UNIVERSITÀ
DEGLI STUDI
DI PALERMO

The
University
Of
Sheffield.

Università degli studi di Palermo

Facoltà di Scienze Matematiche Fisiche e Naturali

Dipartimento di Scienze della Terra e del Mare (DiSTeM)

Rapid sensing of volcanic SO_2 fluxes using a dual ultraviolet camera system: new techniques and measurements at Southern Italian volcanoes

Giancarlo Tamburello

Tutor:
Prof. A. Aiuppa:

Coordinator:
Prof. F. Parello

Co-tutors:
Dr. A. McGonigle
Ing. G. Giudice

Reviewers:
Patrick Allard, Institut de Physique du Globe de Paris
Clive Oppenheimer, Department of Geography, University of Cambridge
Matthew Watson, Department of Earth Science, University of Bristol

Dottorato di ricerca in Geochimica XXIII ciclo (cod. 007)

January 2009 – December 2011

Table of Contents

Abstract

Volatiles carry crucial information on pre- to sin-eruptive processes at active volcanoes. Measurements of gas emission rates (crater plumes, fumaroles, diffuse soil degassing) therefore improve our understanding of degassing processes and subsurface magmatic and hydrothermal conditions, and contribute to eruption forecasting. Recent technological developments in spectroscopy have allowed, over the last 30 years, the remote sensing of magmatic volatile emissions from quiescent and erupting degassing volcanoes. These data-sets have contributed to discovering cyclic gas flux components due to periodic magma supply and replenishment in magma storage zones, and/or timescales of magma migration (and degassing) within the feeding conduit systems of volcanoes (*chapter 2*). In spite of these relevant achievements, a number of magmatic degassing processes have remained elusive to measure, as they occur at a faster rate than the time resolution of most available spectroscopic techniques.

In this study, I take advantage of a novel technique - the UV camera (*chapter 3*) - to image SO_2 emissions from the Italian volcanoes with improved high temporal resolution. The UV camera heralds the much awaited prospect of capturing transient ($\leq$ tens of seconds) volcanic gas-driven phenomena, such as Strombolian explosions and puffing. Here, this technique has been updated to a new configuration (dual-camera system), which combines higher temporal resolution (0.5-1.2 Hz) and improved accuracy relative to the single-camera setup. During the first year of this PhD, the methodology has been extensively tested and improved, whilst developing a user-friendly control software (*Vulcamera*) and a calibration technique (in tandem DOAS-SO_2 quartz cells calibration), which simplify instrument deployment, acquisition and data analysis (*chapter 4*).

The results of the volcano applications of the UV camera are described in *chapter 5*. A first application (*chapter 5.2*) was focused on SO_2 gas flux measurements at individual fumaroles from the La Fossa crater (Vulcano island, Italy) fumarolic field. There, the dual-

UV camera technique allowed the simultaneous imaging of multiple-source emissions, discriminating between SO_2 contributions from the four main fumarolic areas. The UV camera-derived individual fumarole SO_2 fluxes have been used in tandem with MultiGAS-derived gas/SO_2 molar ratios to accurately assess CO_2, H_2O, and H_2S fluxes. Results highlight a factor ~2 increase in CO_2 and H_2O degassing during the La Fossa crater degassing/heating unrest event of November-December 2009.

Bubbles nucleation (birth), coalescence (growth), outgassing and fragmentation (death), are stages of volatile's life within the magma. Our understanding of these processes mainly comes from modelling and textural studies. In this work, I have attempted to retrace part of the gas bubbles' life by measuring - at high rate - SO_2 outgassing rates from two open-vent volcanoes: Stromboli and Etna. On Stromboli (*Chapter 5.3*), the UV camera-derived data allowed the first simultaneous estimate of the SO_2 flux contribution from the three main forms of degassing at Stromboli (passive degassing, 84-92 %; explosive degassing, 5-8 %; puffing, 3-8 %). The obtained high frequency SO_2 flux time-series also revealed the existence of a periodic SO_2 degassing pattern over timescales of minutes, modulated by rhythmic strombolian explosions. Also I report on systematic in tandem UV camera-geophysical observations. Among the key results, I provide experimental evidence for a positive correlation between seismic (very-long period; VLP) thermal, and gas (eruptive SO_2 mass) signals irradiated by individual Strombolian explosions. During each strombolian event, onset of the SO_2 flux emission systematically coincides with deflation of the conduit upon gas slug bursting during the explosion.

At Mount Etna (*Chapter 5.4*), degassing mechanisms and rates have been studied during two field campaigns on Pizzi Dineri (northern rim of Valle del Bove), from which a clear view of the pulsate gas emissions (*gas puffing*) from the North-east crater was available. The >10 hour acquired SO_2 flux time series highlighted a periodic degassing behaviour for this vent, with characteristic periods in the 60-250 s range. This allows deriving new constraints on model gas bubble distribution in a magmatic conduit. The data obtained here support a process of gas packaging into trains of discrete bubble-rich layers. This, coupled with time variations in ascent rate of individual gas bubble layers, may well account for the time-dependent periodicity of observed volcanic SO_2 flux emissions.

Chapter 1
Introduction

A number of volatiles are dissolved in silicate magmatic melts, the most abundant of which are - in decreasing order of abundance - water, carbon, sulphur, chlorine, fluorine and noble gases. These volatile species are in large part mantle-derived; the Earth's mantle is a significant volatile reservoir, where these species exist in the form of thin inter-granular films. Volatiles, and sulphur among them, are magma-transported from the lithosphere to the atmosphere or hydrosphere, to be eventually recycled back into mantle at subduction zones (Wallace, 2005; Oppenheimer et al., 2011). Global climate and life evolution have been deeply affected by such volcano-mediated volatile cycling through the Earth's geochemical spheres (Oppenheimer, 2003).

The amount of sulfur dissolved in magma depends - among other factors (Métrich and Mandeville, 2010; Oppenheimer et al., 2011) - upon confining pressure,

and hence on depth of magma storage. During magma ascent and decompression, volatile solubility decreases leading to gas exsolution, and bubble nucleation and growth (Gonnermann and Manga, 2003). Solubility varies considerably among the different volcanic gas species, resulting in early degassing of the less soluble volatiles (fractional degassing) (Carroll and Webster, 1994; Oppenheimer, 2003).

The most evident expression of magmatic degassing is the atmospheric dispersion of gases and particles emitted from a volcano summit. A plume is a heterogeneous system, including an air-dominated gas phase and aerosols (Oppenheimer, 2003), and it accounts for the majority of the energy and mass daily output of a quiescent volcano (Allard, 1997; Shinohara, 2008).

Sulphur speciates in volcanic gases mainly as SO_2 and H_2S (Oppenheimer et al., 2011), the abundances of the two species being linked via the reaction (Giggenbach, 1987):

$$SO_2 + 3H_2 = H_2S + 2H_2O$$

which, in terms of the equilibrium constant K_T, equates to:

$$\log\left(\frac{SO_2}{H_2S}\right) = \log K_t - 3\log\left(\frac{H_2}{H_2O}\right) - \log(PX_{H_2O})$$

where the ratio H_2/H_2O is a proxy for magmatic redox conditions, and X_{H2O} is the water molar fraction in the gaseous phase. This equilibrium determines sulphur dioxide to be the most abundant S species in high temperature and oxidising magmatic gases (e.g., Aiuppa et al., 2005), and therefore a key target of gas monitoring activities at active volcanoes.

In addition to its relevance in volcano monitoring, studying volcanic SO_2 also has important implications for atmospheric chemistry and climate change (Berresheim et al., 1983). In tropospheric volcanic gas plumes, SO_2 can be relatively fast deposited

(via wet and dry deposition), to give rise to volcanic air pollution, acidification of soils, rainwaters and freshwaters, and eventually anomalously high S contents in vegetation (see Delmelle, 2003 for a recent review). During large-scale eruptions, SO_2 is converted in the stratosphere into radiatively active sulphate aerosols, which may reflect sunlight back to space (Graf et al. 1997). Sulphate aerosols from the Mt Pinatubo plinian eruption, for instance, cooled the troposphere, offsetting the anthropogenic greenhouse effect for a limited duration (Robock, 2002). TOMS (Total ozone mapping spectrometer), along with the infrared TOVS (TIROS Optical Vertical Sounder), provided early estimates of the stratospheric sulphur yield of this eruption (~10 Tg of S; see Oppenheimer, 2003 for a review). The Pinatubo eruption also caused stratospheric heating, an alteration in global stratospheric circulation pattern, and an approximately 20% reduction in Antarctic ozone levels (McCormick et al. 1995). The Mt. Pinatubo eruption has been the most striking recently observed demonstration of the dramatic increase in S atmospheric burden during a volcanic eruption (see Robock and Oppenheimer, 2003).

In light of the above, remote sensing techniques have increasingly been used over the last decades in volcanic SO_2 plume measurement, significantly broadening the ability of volcanic gas geochemistry to contribute to volcanic hazard assessment (Oppenheimer, 2010). For instance, spectroscopic-sensing of volcanic SO_2 effectively contributed to identifying Pinatubo's re-awakening in 1991 (Daag et al. 1996; Hoff 1992), therefore mitigating against the effects of the eruption. The growing need to improve accuracy and time resolution of SO_2 observations at active volcanoes has encouraged the scientific community to refine traditional observation techniques (e.g., COSPEC; Moffat and Millán 1971), and to explore new horizons (a brief review is given in *chapter 2* of this report). Technological progress has boosted this process, and, for instance, the previously used correlation spectrometers (Moffat and Millán 1971, Stoiber et al. 1983) were upgraded (and actually replaced) some 10 years ago by miniatured UV USB-powered grating spectrometers, and in particular the Ocean Optics Inc. USB2000 (e.g., McGonigle et al. 2002, Galle et al. 2003, Horton et al. 2006, McGonigle 2007, Kantzas et al. 2009).

This PhD report aims to contribute to proving further the potential - in a volcanological context - of a novel technique, recently developed for imaging SO_2 emissions: the UV camera. Over the last 5 years, the UV camera has emerged as a key tool to study transient gas-driven volcanic phenomena, such as Strombolian (Mori and Burton, 2009) and Vulcanian (Yamamoto et al., 2008; Nadeau et al., 2011) explosions, which are far too rapid (timescales ≤ tens of seconds) to be resolved using conventional scanning spectroscopic instruments (e.g., Edmonds et al., 2003; McGonigle et al., 2003; Oppenheimer, 2010). In this study, we make use of (and provide a detailed report on) a recently introduced (Kantzas et al., 2010; Tamburello et al., 2010) variant of this technique, which requires operation of two simultaneously acquiring cameras. This dual-UV camera setup combines high temporal resolution (up to ~ 1 Hz) with improved measurement accuracy. This technique are discussed in *chapter 4* of this dissertation.

We have taken advantage of the improved capability of this dual-UV camera configuration to obtain novel (high spatial and temporal resolution) time series of volcanic SO_2 emissions from three active Italian volcanoes: Vulcano Island, Stromboli and Etna. These volcanoes cover a wide spectrum of degassing styles and mechanisms. Our observations, the main results of which are detailed in *chapter 5*, allow a number of new constraints to be derived on the modes and rates of SO_2 release from both a dormant volcano in a fumarolic stage of activity (Vulcano Island) and a quiescent (Etna) and an erupting (Stromboli) open-vent basaltic volcanoes. More specifically, at Vulcano Island (*section 5.2*), I focus on examination of the structure of the fumarolic system (analysis of individual fumaroles' contribution to the total SO_2 budget), while at Stromboli (*section 5.3*) and Etna (*section 5.4*) I explore short term (timescales of seconds to minutes) patterns and trends in SO_2 flux sourced by both active (puffing, Strombolian explosions) and passive (quiescent) degassing modes. I conclude that, at such open-vent volcanoes, gas bubble coalescence, and or structuring into waves of bubble-rich layers, may originate a non-stationary (periodic) SO_2 flux degassing regime.

Chapter 2

SO_2 flux measurements: four-decade story

2.1 Introduction

Volcanic degassing occurs in range of ways: during volcanic dormancy, and in periods of either low intensity effusive eruptions or highly energetic (Hawaiian to Plinian) explosive activity. Volcanic gas measurements provide important information on underground magma conditions, enabling the definition of, for instance, the masses of magmatic bodies in the subsurface, whether magma flow rate to the surface is escalating or decreasing, whether a volcanic system is open or sealed to gas flow, and whether hydrothermal interactions are involved. Such data are vital for volcano

monitoring, and have significantly contributed to volcanic hazard assessment at a number of targets worldwide (Oppenheimer, 2003)

Volcanic gas geochemistry has been limited for over a century to in-situ sampling of fumaroles and plumes. Traditional collection methodologies included flasks filled with alkaline solutions (Giggenbach, 1975), and/or bubbling of vent gases through alkaline solutions or base-treated filters, which act as acid traps (Symonds et al. 1994). Despite the numerous gas species detected, sampling, and transport to the laboratory for subsequent analysis require days to be accomplished, resulting in a number of limitations: poor temporal resolution (with gas data traditionally taken at 10^{-5} Hz rate) relative to geophysical techniques (seismology primarily), which can acquire data continuously and with an high temporal resolution (~ 1 Hz); the inherent risks for researchers who approach the vents; and the fact that volcanic summits are often not physically accessible, restricting sampling to low temperature fumaroles, which may be unrepresentative of the volcano as a whole.

Over the last 30 years, ground-based remote measurement of SO_2 flux has been playing an increasingly important role in volcano monitoring. The clear advantage is its capability to acquire data far from the craters and areas at risk, with a time resolution of minutes to hours (far higher than in-situ sampling methodologies). In this chapter, I review briefly the state-of-the-art of SO_2 flux methodologies, and the progresses made over the last ten years (Fig. 2).

2.2 Basic theory

Broadly speaking, remote gas sensing techniques are based on the measurements of the attenuation of light (natural or artificial) by a volcanic gas plume (Fig. 1). Absorption involves only particular spectral windows, depending on the target gas species, and is concentration-dependent as described by the Lambert-Beer Law:

$$(1) \quad I(\lambda) = I_0(\lambda) \cdot e^{-\sigma(\lambda) \cdot N \cdot L}$$

where $I(\lambda)$ are $I_0(\lambda)$ the intensities of the radiation after and before attenuation due to target gas, $\sigma(\lambda)$ is the absorption cross-section of the absorbing gas species; and the product of the number of molecules in the optical path (N) and its length (L) represents the column amount, usually expressed in *ppm·m*. An a-priori assumption is made that the optical path is straight through the volcanic plume, and that multi-scattering effects are negligible (see *section* 2.4).

The most ubiquitously used spectral window for such measurements has been the ultraviolet (Galle et al., 2003), and particularly down-scattered solar radiation sampled from the ground to assess volcanic SO_2 emission rates. Research has focused on SO_2 because of its strong UV absorption features, low background atmospheric concentrations (< 1 ppb) and relatively high abundance in volcanic plumes (>1 ppm). In contrast, volcanic H_2O and CO_2 are extremely difficult to measure remotely, because of their high concentrations in background (ambient) air.

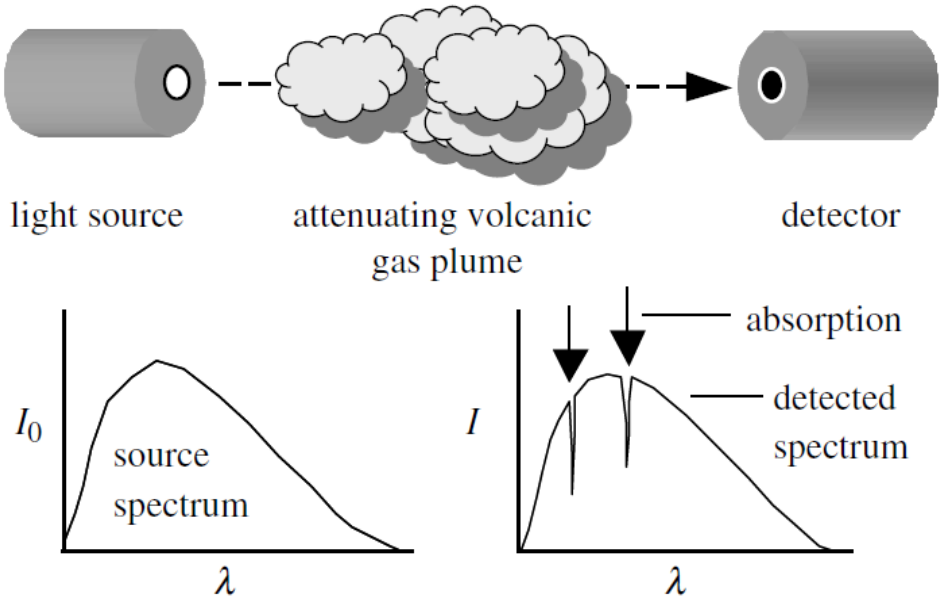

Figure 1: Transmission of radiation (in this case from an artificial lamp) through a volcanic plume, before detection by a spectrometer. The emitted source spectrum $I_0(\lambda)$ and the measured spectrum $I(\lambda)$ differ depending upon the composition of absorbing species in the plume (McGonigle et al., 2005a).

After more than 30 years of valued service in Volcanology, the correlation spectrometer (COSPEC; Moffat and Millán 1971, Stoiber et al. 1983) has largely been

replaced – ~10 years ago - by miniature UV USB-powered grating spectrometers, with spectral analysis via differential optical absorption spectroscopy (DOAS) (McGonigle et al. 2002, Galle et al. 2003, Horton et al. 2006, McGonigle 2007, Kantzas et al. 2009).

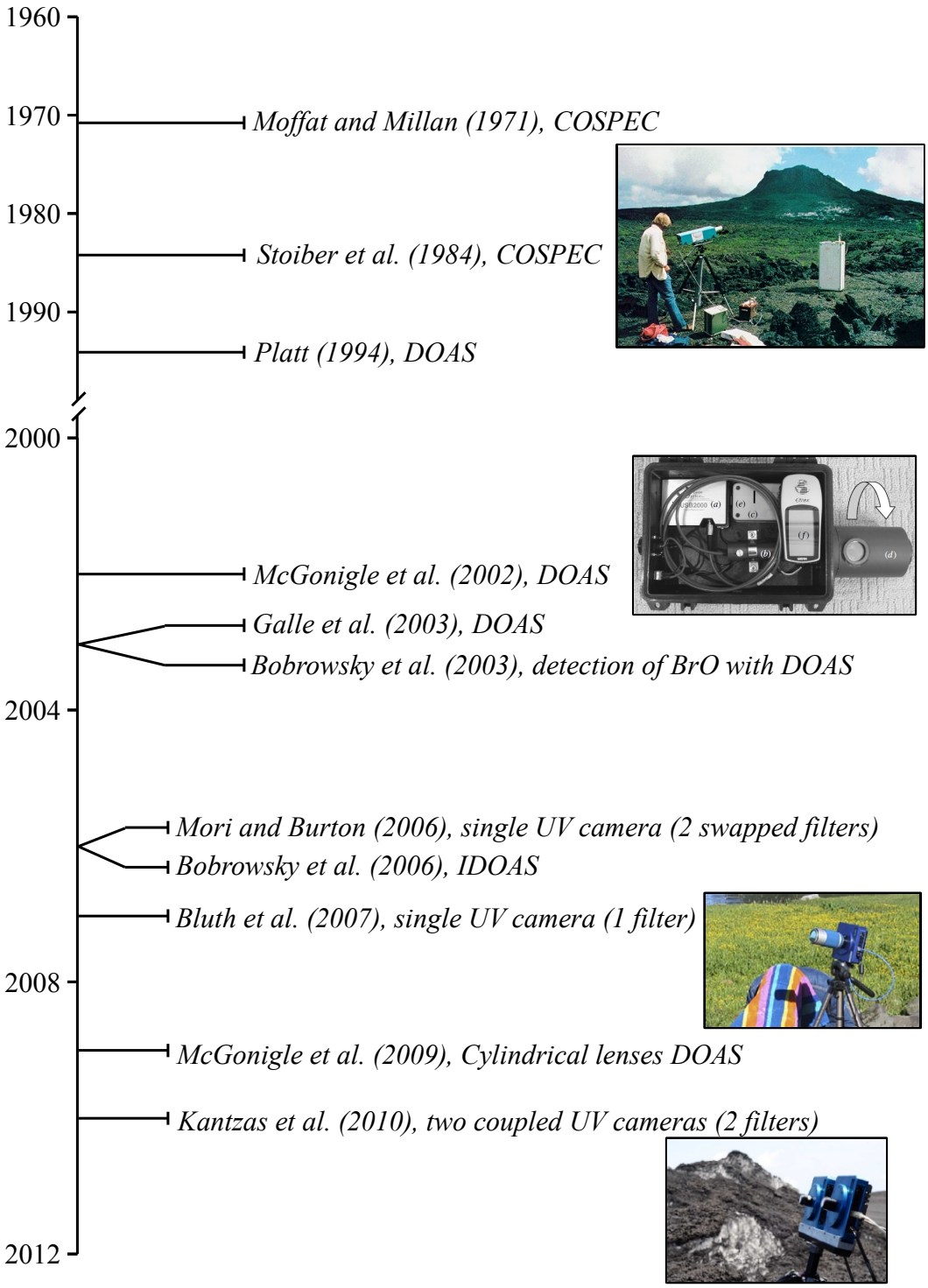

Figure 2: This timeline chart illustrates the advances in UV remote sensing of volcanic gas.

2.3 DOAS

In contrast to the COSPEC, which works on a small range of the UV spectrum via an internal mechanical correlation procedure (Millán, 1980), the less expensive USB spectrometers (e.g. USB2000, USB4000, Avaspec) acquire an entire UV spectrum, which can be subsequently processed using a differential optical absorption retrieval technique to derive SO_2 column amounts. Miniature UV spectrometers have been widely deployed on volcanoes and for routine operations by volcano observatories. SO_2 flux measurements have been mainly carried out in two modes: by scanning from a fixed position downwind of the volcano, or traversing underneath the plume by foot, boat, aircraft or road vehicle (Fig. 3a,b), using a spectrometer coupled via an optical fiber to a narrow field of view (FOV) telescope (few mrad).

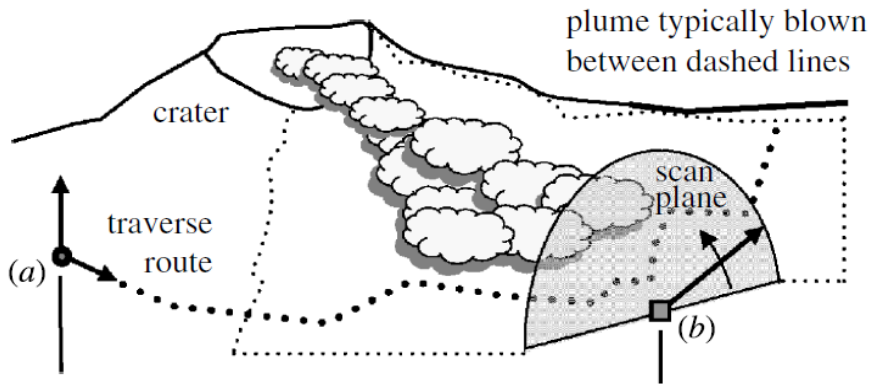

Figure 3: (a) Diagram of a traverse route underneath a volcanic plume with a vertically pointing spectrometer, showing the vector of motion (dotted line) and (b) scanning from a fixed position below the plume (McGonigle et al., 2005a).

2.3.1 Traversing DOAS

During traverses, the telescope is zenith oriented and a GPS receiver measures the distance $d_{i,(i+1)}$ between the i-th spectrum and i-th + 1 spectrum(spectra are acquired every 1-4 s depending on the skylight intensity). A SO_2 plume column amount c_i is calculated by dividing every i-th spectrum by a reference spectrum

acquired outside the plume (white spectrum) according to the Lambert-Beer law (Eq. 2). This operation removes the possible interference due to plume aerosols' absorption. By multiplying the retrieved concentration for each spectrum (converted from ppm·m to kg·m^{-2}) by *d*, and then summing these products for all spectra acquired under the plume, the integrated column amount (ICA) is obtained:

$$(2) \quad ICA = \sum d_{i,(i+1)} \cdot c_i$$

The *ICA* is then multiplied by the plume transport speed (m·s^{-1}) to derive flux (kg·s^{-1}).

A traverse must be performed by an operator, and generally takes minutes to tens of minutes, depending on the plume width, ground path length, and the transportation medium

2.3.2 Scanning DOAS

SO_2 flux measurements can also be taken from a fixed position (scanning DOAS, Fig. 3b), a technique which is rapidly propagating across the scientific community, especially for continuous monitoring from automatic stations (Salerno et al., 2006; Burton et al., 2009; Galle et al., 2010). In this case, a telescope scans the sky over 180° along a vertical plane (Edmonds et al., 2003) or a conical surface (Galle, 2007) intersecting the gas plume as perpendicularly as possible; an integrated column amount of a cross section of the plume can then be determined and, if plume velocity is known, the flux through the cross section can be calculated. The advantage of a conical scanning surface is managing much larger variations in plume direction than with simple flat scanning geometries (Galle, 2007; Johansson, 2008). A complete plume scan takes a few minutes, depending on the distance from plume and on plume width. Such time resolution represents a discrete achievement for DOAS measurements. Figure 4 shows an example of SO_2 gas flux time-series (sampling period < 5s) from San Cristóbal volcano in Nicaragua, obtained using a scanning

miniaturized differential optical absorption spectroscopy (Mini-DOAS) instrument (Galle et al., 2010).

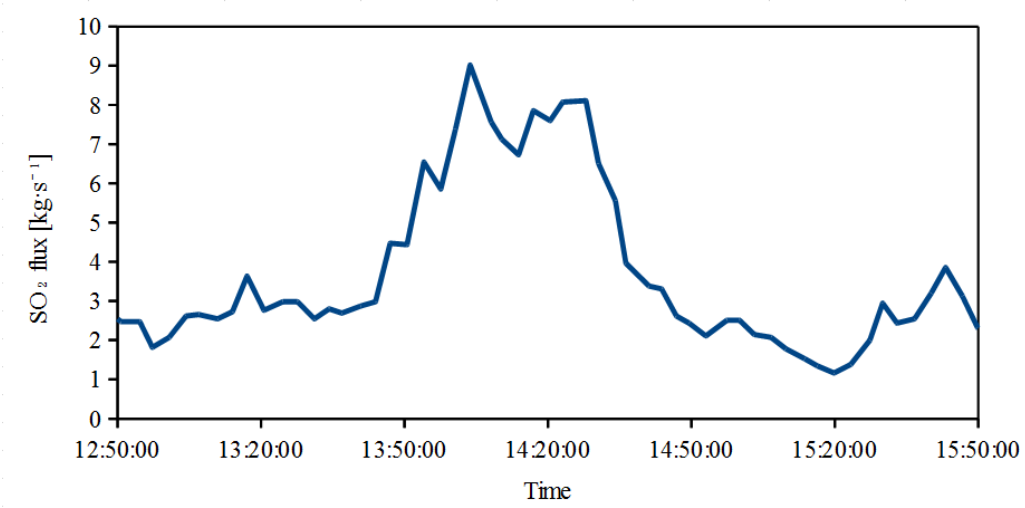

Figure 4: SO_2 flux time series from San Cristòbal volcano on 23 November 2002 (Galle et al., 2010).

Continuous scanning DOAS stations have provided interesting results for the monitoring of active volcanoes. For instance, the FLux Automatic MEasurement (FLAME) network (Burton et al., 2009) is a set of 4 scanners around Stromboli volcano (Italy), connected via WiFi network to the main observatory in San Vincenzo. The FLAME network has been conceived after the 2002/03 eruption of Stromboli, and it began operations on 2004 with the objective of automatically measuring SO_2 fluxes from the summit craters. FLAME detected elevated SO_2 fluxes during the 2007 eruption of Stromboli (Burton et al. 2009, Fig. 5), which were proposed to reflect a change in magmatic convective circulation in the volcano's upper conduit.

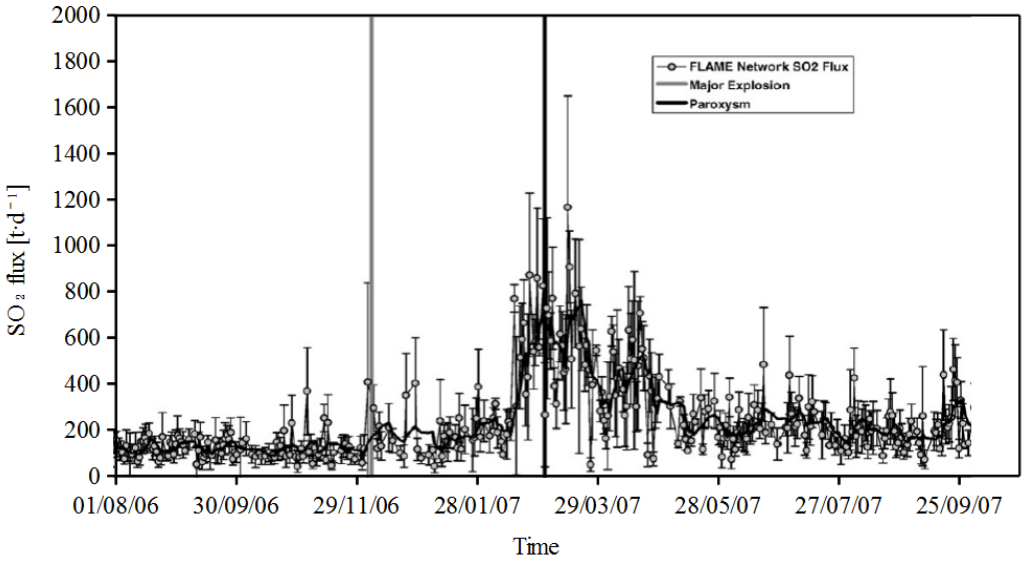

***Figure 5:** Average daily SO_2 flux from Stromboli, measured with the FLAME network. Grey bars indicates the 2007 eruption (Burton et al., 2009).*

In view of these recent results, researchers have focused their attention towards the automation of SO_2 gas flux measurement systems. The NOVAC project (Network for Observation of Volcanic and Atmospheric Change) started on October 2005 with the objective of establishing a global network of stations for SO_2 flux measurements at active volcanoes. At present, NOVAC encompasses observations at 20 volcanoes including Mt. Etna, one of the most active and strongest volcanic gas emitter in the world. The network makes use of a scanning dual-beam Mini-DOAS (Galle et al., 2006), which represents another step forward in volcanic gas spectroscopy given its capability of measuring SO_2 and BrO emissions from a volcano with less than 5 minutes time resolution during daylight.

Figure 6 shows one year of SO_2 flux measurements of the NOVAC station at Tungurahua, an andesitic-dacitic volcano in Ecuador. The dataset has been coupled with the seismic signals monitored by the IGEPN network. The comparison shows a fair correlation only within a time-scale of months.

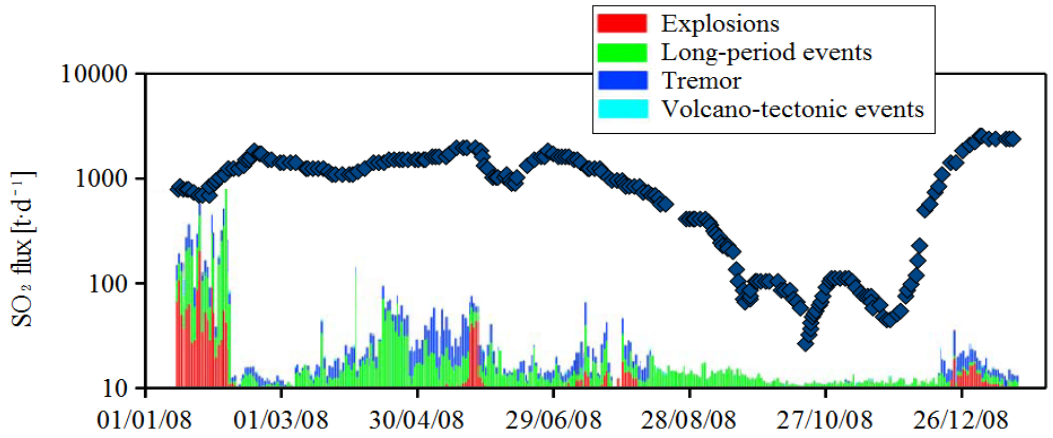

Figure 6: Results of measurements of the NOVAC stations at Tungurahua. SO_2 gas emission rate is measured in tons per day by the NOVAC instruments. All the geophysical signals are quantified as the number of seismic events per day by a dense network of seismometers around the volcano (Galle et al., 2010).

2.3.3 Cylindrical lens DOAS

Scanning and traversing DOAS modes derive the SO_2 molecules distribution along a plane of the gas plume resolved via point-to-point measurements. The accuracy and duration of this assessments depend on the number of spectra collected. Despite significant progresses in improving the sampling frequency of DOAS, from half an hour to only a few minutes, the temporal resolution still remains well below that achieved by geophysical observations, preventing us from a full data comparison.

A first attempt of spectroscopically capturing SO_2 fluxes at high-frequency has been made by McGonigle et al. (2009) on Stromboli. This work is based on the use of two USB2000 spectrometers, each coupled to telescopes with cylindrical lenses: these have quasi-rectangular fields of view, and allow capture of an integrated column amount directly from a single collected spectrum every 1-1.4 s (Fig. 7) (a far more rapid alternative to traversing or scanning). The two fields of view were separated by a small angle, which permitted tracking of plume heterogeneities in the time-stamped datasets obtained from each spectrometer. Emission rates were thereby integrated with geophysical data, providing one of the first examples of this nature, and demonstrating correlation between the magnitudes of seismic and thermal signals and the SO_2 mass

of Strombolian explosions. This technique presented some disadvantages, however, such as the permanent and invariable field of view of the lenses, and the difficulties in keeping a good alignment between the measured sections and plume location.

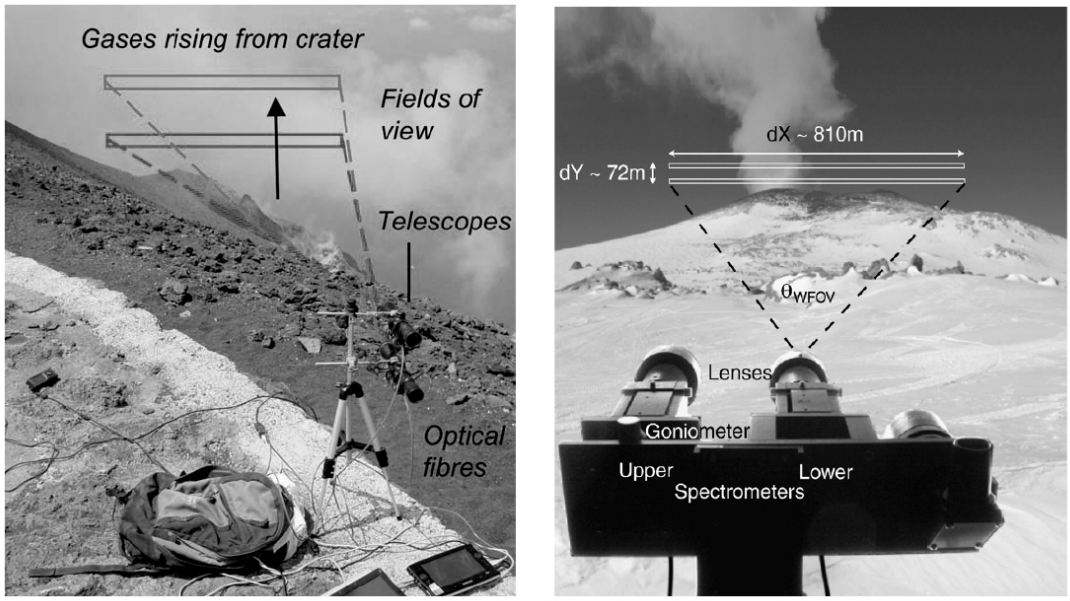

Figure 7: Two telescopes with cylindrical lenses scanning horizontal stripes of a vertically rising plume on Stromboli (left photo) and Erebus (right photo).

The same approach has also been deployed on Mt. Erebus in Antarctica (Boichu et al. 2010), which led to discrimination of SO_2 fluctuations linked to atmospheric processes, from those resulting from magmatic activity. A gas flux periodicity of 11–24 minutes was observed, leading to important findings regarding transport dynamics of volcanic gas in the conduit (see c*hapter* 3).

2.4 Sources of error

In recent years, a number of studies have detailed the sources of error associated with SO_2 flux measurements, which have led to attempts to improve measurement accuracy. Following Galle et al. (2010), we recognize three important sources of error: radiative transfer, plume-instrument geometry, and plume speed.

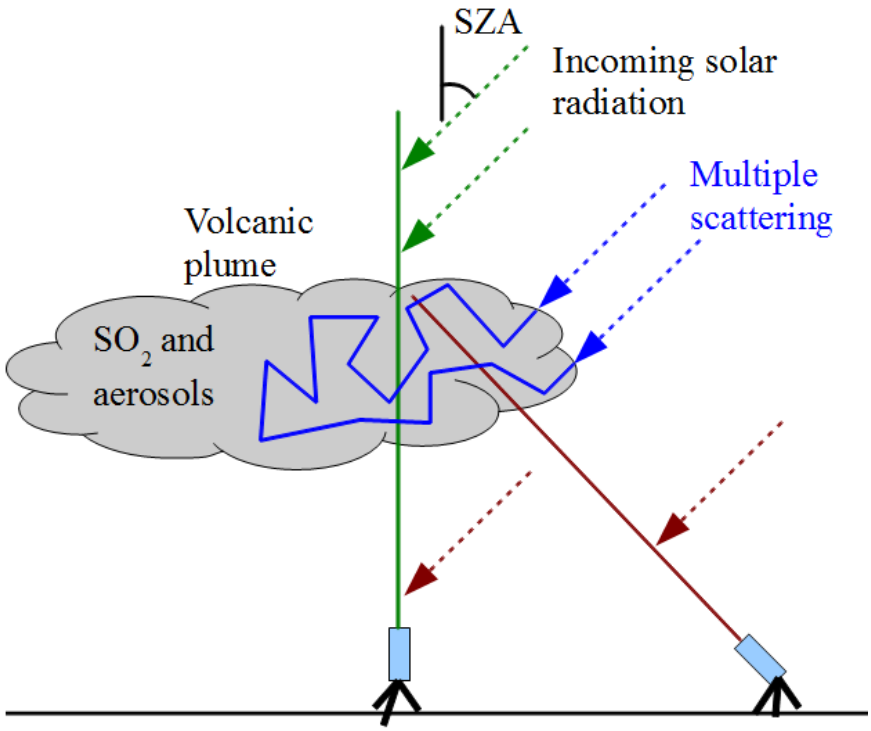

Figure 8: Schematic of the radiative transfer effect and of the different possible photon paths from the sun to a remote sensing instrument. The green path shows the idealized photon path: light is scattered above the volcanic plume and passes through the plume in a straight line. The red path represents the dilution effect. Light is scattered between the plume and the instrument and effectively dilutes the measured column density. The blue path depicts the case of multiple scattering occurring inside the plume causing an extension of the light path and therefore an enhancement of the measured column density (Kern et al., 2009).

Ground based remote sensing theory is based on the assumption that radiation, scattered by molecules and particles in air behind the plume, passes through the plume with straight paths, before being detected by the instrument. Instead, depending on the opacity of the plume (which contains ash, condensed water and aerosols), multiple scattering can occur (Fig. 8), resulting in extended in-plume light paths, and leading to an overestimation in the derived SO_2 flux. Conversely, scattering effects can also bring light that has not been absorbed by the gas into the field of view of the instrument, leading to an underestimation of the detected SO_2 column amount (dilution effect). This source of error has been recently quantitatively measured by Mori et al. (2006) using DOAS instruments.

These effects and their dependencies were well described by Kern et al. (2009), who simulated skylight optical paths in different scenarios. The concept of "air mass factor" (AMF) was applied, defined as the ratio between the measured slant column density and the theoretical column density on a straight line through the volcanic plume along the instrument's viewing direction. Therefore, an AMF of 1 means that there is no error in the measurement, and hence that the effective photon path is equal to the length of a straight line through the plume along the instrument's viewing direction. Results show that AMF depends significantly on plume-instrument distance, and on SO_2 and aerosols concentrations in the plume. These dependencies have an affect on all ground-based remote measurements.

Scanning methods require knowledge of plume height and speed for SO_2 flux calculation. The former, in conjunction with plume dispersion and imperfections in orientation and levelling of the instrument, can be a important sources of errors (up to 30 %) (Salerno et al., 2009; Galle et al., 2010). Reliable plume speed derivation is another well-known issue of these remote measurements (Stoiber et al., 1983; Casadevall et al., 1987, Elias et al., 1988; Williams-Jones et al., 2006). A common assumption is that the volcanic gas plume moves at same speed as wind at the same altitude, even though significant differences have been observed (10-320 %). There have been attempts to obtain plume speed in different ways: anemometric measurements of the wind speed at the summit of the actual volcano or on a nearby mountain, use of models of regional winds based on meteorological balloon data, the use of dual-beam DOAS (Galle et al., 2010) or two spectrometer techniques (McGonigle et al., 2005b; Williams-Jones et al., 2006) (see *section* 4.1.5). This latter method is, however, only useful when at least part of the plume is over the instrument.

2.5 Limitations and outlook

The first high-time resolution measurements of the volcanic SO_2 flux have confirmed the non-stationary nature of quiescent volcanic emissions, and have highlighted the importance of studying short-period SO_2 flux fluctuations to improve our understanding of gas transport dynamics in the magma-conduits, and their control on modes and timing of a volcanic eruption.

At active vents, gas ascent is essentially driven by convection, due to a temperature difference between hot volcanic gases and the cold atmosphere. After the gas has cooled down, the plume continues to rise due to buoyancy until, hundreds of meters from the vent, increasing wind speed and collision with denser atmospheric layers turn its vertical rise into an horizontal flow. Aside from the errors that are common to all remote sensing techniques, scanning and traversing methods are performed kilometres far away from the volcano, looking at a homogeneous plume that has lost its original features, in particular those temporal heterogeneities that make up the low-period components of volcanic gas emissions. Moreover, the low temporal resolution (a few minutes at best) of DOAS techniques makes them unsuitable to characterise transient volcanic phenomena (e.g., explosions) , representing the most energetic (and, therefore, potentially dangerous) manifestations of volcanic degassing.

In light of the above, remote sensing measurements from proximal sites (< 1 km) could improve our knowledge of degassing processes, increasing our spatial resolution and preventing changes in the plume's structure from being lost prior to detection. Given its fast sampling rate, cylindrical lens DOAS could represent a good tool for these purposes. This technique is, however, highly dependent on plume width and direction, which are more variable when observed at short distances. In the next *chapter*, I will discuss the advantage of a novel methodology of volcanic SO_2 imaging: the UV camera.

Chapter 3
UV camera and SO_2 imaging

3.1 Introduction

This section briefly reviews the principles of operation, and the most recent applications, of the UV camera technique. The updated UV camera instrumental setup, developed in this work, is detailed on *chapter* 4.

3.2 General instrumentation

The use of an UV camera in Volcanology has been first reported by Mori and Burton, (2006) and Bluth et al., (2007). Broadly speaking, the UV camera consists of a main portable electronic body with a thermo-electrically cooled CCD detector. The CCD has two output amplifiers: one for low noise, and a second for exceptionally

high dynamic range. The exposure time of the camera can range from 10 milliseconds to 183 minutes, with a 2.56 microsecond increment. A fixed focal length quartz lens is screwed in front of the camera, and a pass-band filter is placed in front of this, with a controlled USB wheel allowing the use of more than one filter with a single camera. The UV camera requires 12 VDC and consumes, with the shutter open and maximum cooling, 40 W at most.

Figure 9: The two most used UV camera model in volcanic SO_2 imaging (http://www.ccd.com).

The most commonly used UV cameras (Fig. 9) as cited in the literature are:

1. Apogee Alta U260, fitted with a 16 bit 512×512 pixel Kodak KAF-0261E CCD detector (~7000$);
2. Apogee Alta E6, fitted with a 16 bit 1024×1024 pixel Kodak KAF-1001E-2 CCD detector (~12000$);

The former, which is clearly less expensive, provides more than enough spatial resolution and has considerably reduced readout times, enabling higher acquisition frequencies relative to the 1024×1024 pixel camera.

Quartz lenses do not affect wavelengths in the near UV spectrum, their fixed focal lengths ranging 25-105 mm, and thus providing a field of view of 24-13° respectively. The focus is manual and the iris ranges from F2.8-16. The shape of the iris can be triangular or hexagonal. This feature is important in digital photography, because multiple reflections of light beams inside optical lenses can create multiple projections of the iris shape in the CCD array (Fig. 10). This effect is known as lens flare, and it disappears completely using the max aperture F2.8 of the lens.

Figure 10: Flare effect on a triangular shaped iris lens and a 25 mm and 105 mm focal length lenses.

The camera operates on the principle of contrasting the brightness of the pixels in the presence/absence of SO_2 absorption when measuring scattered sunlight (skylight). This can be done with two pass-band filters placed in front of the lenses of two simultaneously operating cameras, or with a single camera and a filter wheel. The first filter α transmits wavelengths strongly affected by the presence of SO_2, the second one β transmits wavelengths that are not absorbed. A qualitative measure of absorbance A can therefore be obtained per camera pixel:

$$A = -\log_{10}\left[\frac{\left(\frac{IP_{\alpha}}{IB_{\alpha}}\right)}{\left(\frac{IP_{\beta}}{IB_{\beta}}\right)}\right] \quad (3)$$

where IP and IB are plume and background images respectively, after being dark-image subtracted. Dark image collection, obtained covering the camera lens, is necessary to accommodate for dark current and electronic offset. As these phenomena are quasi-constant, over timescales of 1 hour, following the ten minute switch on thermal stabilisation, a single dark image, per camera, will be enough for such an acquisition duration. Conversion from A to ppm·m is achieved through a calibration procedure involving cells of known SO_2 concentration (see *section* 4.1.3).

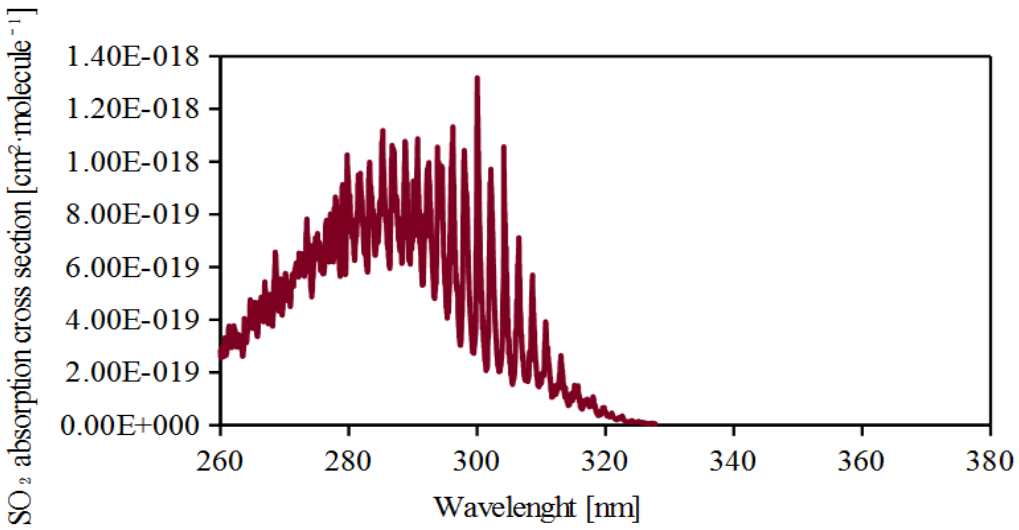

Figure 11: Sulphur dioxide absorption cross section (Vandaele et al., 1994).

Sulphur dioxide absorption ends at ~320 nm (Vandaele et al., 1994), and filters α and β operate in the range 300-320 nm and 320-340 nm respectively (Fig. 11). All interferences are supposed to be spectrally flat over this 300–340nm range, and therefore to have no effect on measured absorbance. Filters can be manually switched if the sampling period is >3 s (Mori and Burton, 2006), or automatically using a USB controlled filter wheel (e.g. the Apogee AFW50-7S Filter Wheel, Fig. 12). The latter allows one to take two consecutive images in ~4 s.

Figure 12: Apogee AFW50-7S filter Wheel mounted on a Apogee UV camera.

Alternately, a higher sampling frequency can be achieved using a single filter in a spectral region where SO_2 is absorbed (Mori and Burton, 2009; Bluth et al., 2007; Dalton et al., 2009), in which case A is measured as:

$$(3) \quad A = -\log_{10}\left(\frac{IP_\alpha}{IB_\alpha}\right)$$

The difficulty with a single filter, however, is that one is measuring the plume attenuation caused by both gas and aerosols, with no means of discriminating between the two (see *section* 4.1.1).

3.3 Recent applications

Remote sensing techniques have been used in the last decades to measure the SO_2 flux from volcanoes and therefore monitor their activity status. This has made it possible to link SO_2 emission rates with magmatic budgets at several volcanoes (Allard et al., 1994; Caltabiano et al., 1994; Hirabayashi et al., 1995; Allard, 1997; Watson et al., 2000; Edmonds et al., 2003, Aiuppa et al., 2010), but over time scales of weeks to years. High-rate SO_2 observations have long been challenging, preventing

investigation of fast-occurring volcanic processes (e.g., explosions), and their underlying degassing mechanisms. Several efforts have been made in calculating SO_2 flux from infrasonic data, but without any tangible result (Vidal et al., 2006).

Over the last few years, the UV camera technology has represented an important step forward in volcanic gas flux measurement, enabling the capture of consecutive images of a volcanic plume at steps of ~1s. This highly improved temporal resolution has ultimately opened the way to comparison of SO_2 flux time series with seismic and infrasonic datasets, thus contributing to reduce the existing gap between volcano-geochemistry and geophysics, and our better understanding of degassing process.

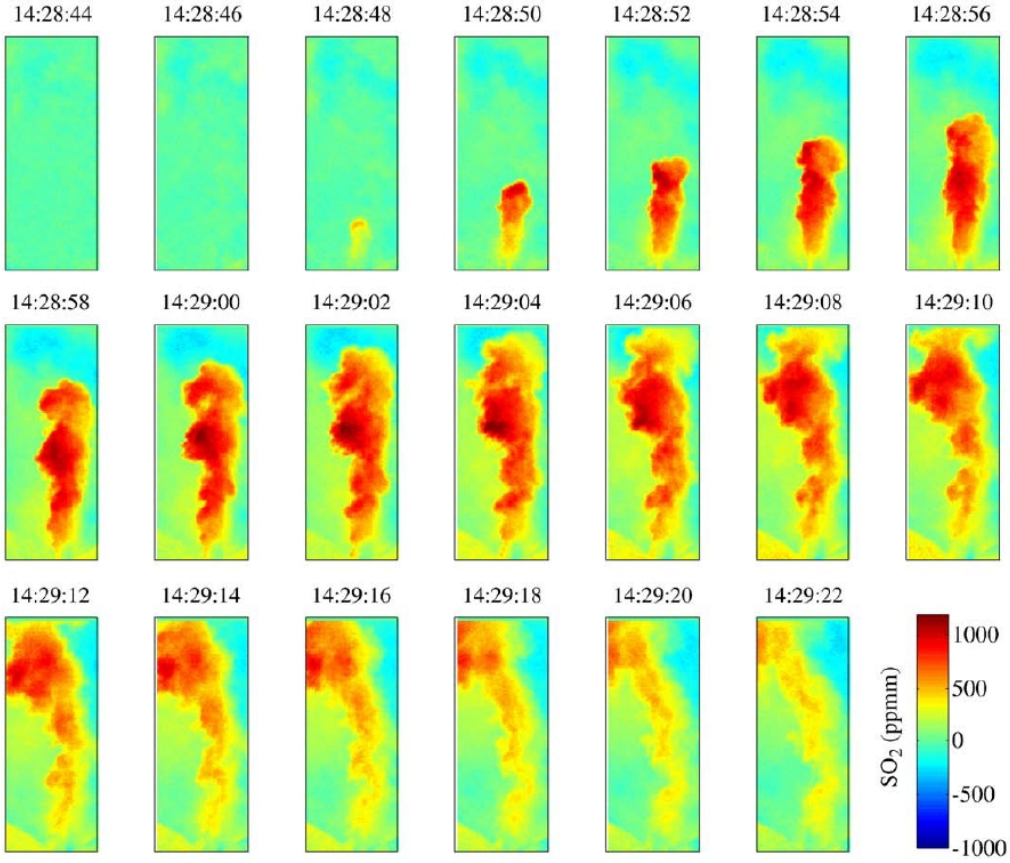

Figure 13: Time sequence of SO_2 column amount images of a single hornito eruption (Mori and Burton, 2009).

The advantage of the high temporal and spatial resolution of the UV camera has been demonstrated by Mori and Burton (2009), who first quantified the gas mass

emitted during a single (Strombolian) explosion on Stromboli (cfr. *section* 5.3). However, the ascent speed of the eruption plume was fast relative to the field of view of the camera (Fig. 13), making switching between two filters (manually, or with a filter wheel) between two consecutive images impractical. To overcome this problem, the authors used, for most of the study, a single 310 nm bandpass filter; they additionally observed two further hornito eruptions - using both filters - to estimate the aerosol effect on SO_2 eruptive mass.

The observed SO_2 mass amounts ranged from 15-40 kg in five discrete explosions, which led the authors to conclude that explosive gas output contributes to 3–8% of the total SO_2 flux from the volcano. Based on the well-known (Burton et al., 2007) chemical composition of the gas driving the explosions, they calculated that the total emitted gas amount may range between 360 and 960 kg per eruption.

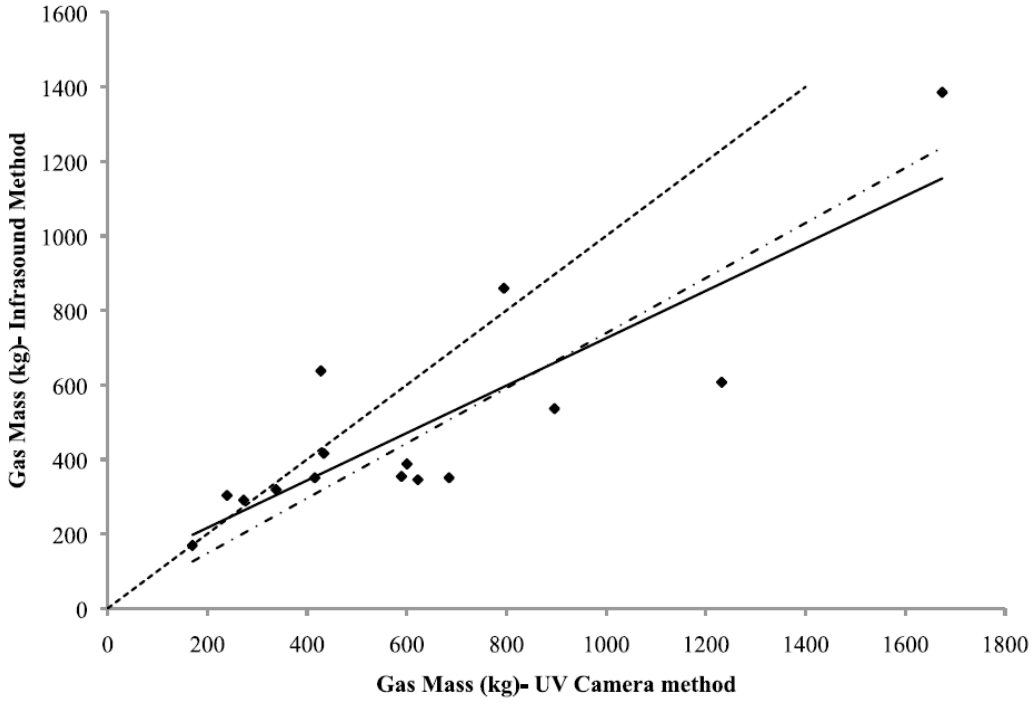

Figure 14: Correlation of gas mass estimates from the UV camera and infrasound methods on Pacaya volcano (Dalton et al., 2010).

Strombolian activity on Pacaya volcano (Guatemala) was investigated, by use of a single UV camera, by Dalton et al. (2010). The target of this work was to compare independent gas mass estimates made with UV camera and infrasound records during

discrete events. The observed explosions were small, and overall responsible for variations in the total SO_2 flux in the order of 10-20 $kg \cdot s^{-1}$. The results have corroborated the use of both acoustic (excess pressure integration) and UV camera as independent techniques to retrieve gas masses associated with discrete degassing events (Fig. 14). In addition, the authors provided support for earlier theory that the dominant acoustic signals recorded at Pacaya are created by Strombolian bubble-burst events.

High temporal resolution SO_2 emission rate data have been collected with a single UV camera at Santiaguito volcano (Guatemala) in 2008 and 2009 by Holland et al. (2011). Santiaguito is an ideal case study to investigate processes of degassing during dome-forming extrusion of an intermediate magma (compositionally very similar to products of the 1902 Plinian eruption of the parental Santa María volcano). The dome has been characterised by continued extrusion of dacite block lava flows accompanied by frequent (0.5–2 per hour) low-intensity explosions, producing ash and gas plumes to heights of 0.5–2 km above the volcano (Sahetapy-Engel et al., 2008). The dome's cap rock is fractured and is permeable to gas flow, and shear fracturing at the conduit margins has been proposed as the most likely explosion mechanism. Measured quiescent degassing ranged from 0.4-1 kg s^{-1}, punctuated by small increases in emission rates (up to 2–3 $kg \cdot s^{-1}$) during explosions, as shown in Fig. 15

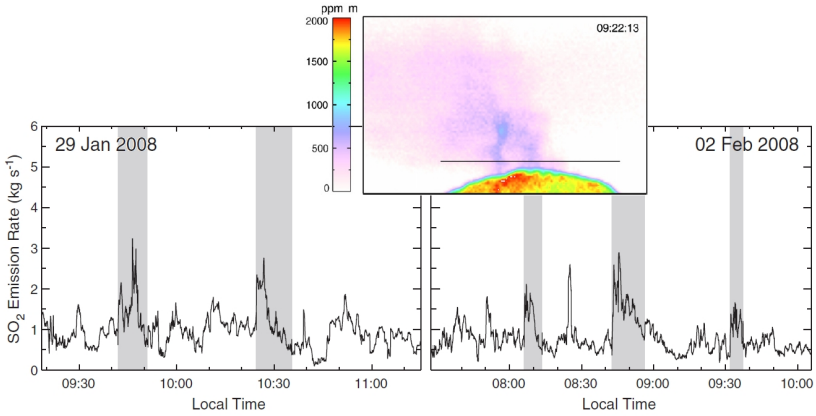

Figure 15: Time series of SO_2 emission rates and eruption periods (gray bars). The pseudo colour graph shows the plume of Santiaguito and the section (black line) used for flux calculations (Holland et al., 2011).

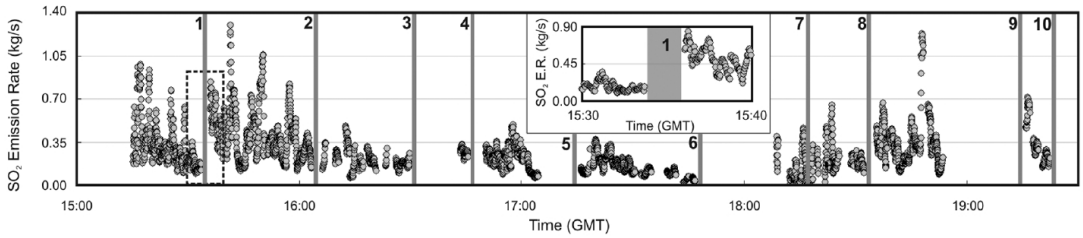

Figure 16: SO_2 emission rates from Fuego volcano on 21 January 2009. Portions of plots with no SO_2 data reflect periods of meteorological cloud or ash in the field of view or pauses in data acquisition for calibration. The gray bars represent explosion occurrences (Nadeau et al., 2011).

A first integration of UV camera and seismic measurements has been performed by Nadeau et al. (2011) in January 2009 at Fuego, a basaltic-andesite stratovolcano (~3800 m a.s.l.) in central Guatemala, characterized since 1999 by periodic lava flows, passive degassing, and explosions (Lyons et al., 2010). The SO_2 emission rate data (Fig. 16) have been obtained from a site ~1 km far from two closely-spaced vents, using a single UV camera (1024 × 1024 pixels). On the basis ofin tandem seismic and visual observations and high-resolution SO_2 emission rates, Nadeau et al. (2011) linked source processes of tremor and degassing, and highlighted a decrease in gas emission prior to explosions interpreted to arise from rheological stiffening within the upper conduit.

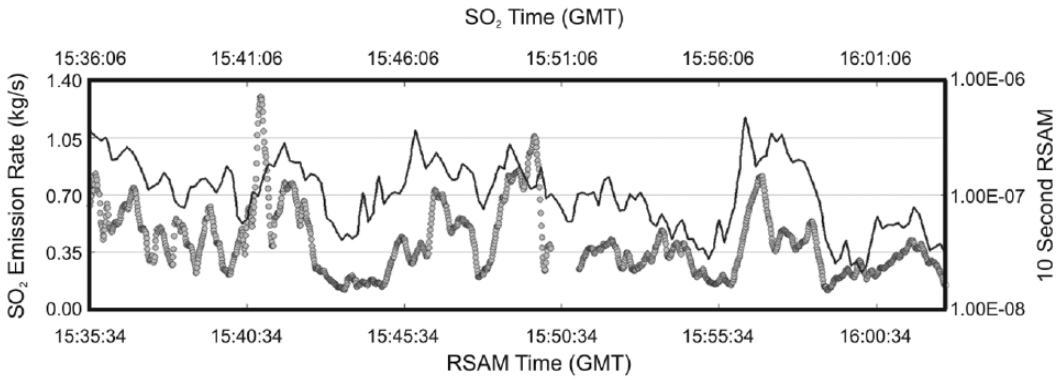

Figure 17: Example of ~30 minute period of similarity between SO_2 emission rate (circles) and low‐frequency 10 second average seismic amplitude (RSAM; black line) (Nadeau et al., 2011)

Moreover, the high correlation between tremor and SO_2 flux (Fig. 17) was used to support the commonly held view that rapid flow of bubbles and bubble-rich magmatic fluids are the main source of seismic tremor (Chouet, 1992; Chouet, 1996).

Kazahaya et al. (2011) examined the relationship between VLP pulses and volcanic gas emissions at Mt. Asama (Japan), an andesitic-dacitic volcano characterised by the presence of a small open vent on the crater bottom (~ 300m a.s.l.). After a recent eruption on February 2009, ash-free degassing bursts from this vent have frequently been observed, occurring just after a VLP pulse. The authors have obtained high temporal resolution SO_2 flux data using two UV cameras, following the methodologies conceived by Mori and Burton (2006), Bluth et al. (2007), and Kantzas et al. (2010).

Kazahaya et al. (2011) revealed that the eruptive gas emissions at Mt. Asama are larger than those at of Stromboli by one to three orders of magnitude, contributing to about 16 % of the bulk SO_2 emission. The strong correlation between SO_2 mass and the VLP displacement produced during gas bursting (Fig. 18) provides a linkage between the two parameters.

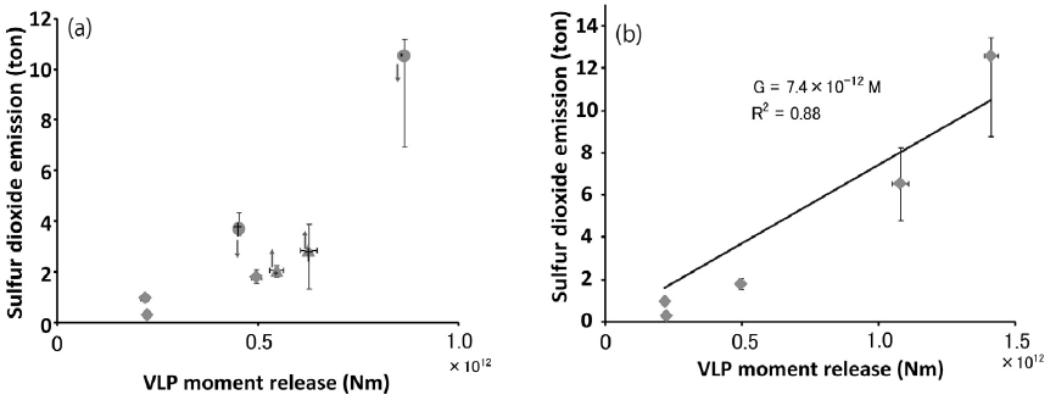

Figure 18: Plot of SO_2 emission and VLP pulse moment. (a) For seven eruptions: the triangles and circles with arrows correspond to the events that systematically under - or overestimated SO_2 emissions, respectively. (b) The relationship between volcanic gas emission and moment of VLP pulse where values of consecutive events, which include systematical errors, are summed (Kazahaya et al., 2011).

As this rapid review shows, applications of the UV camera system have been increasing in number and quality over the last 5 years, and demonstrate the enormous potential of this methodology.

Figure 19: Two worst case scenarios for remote SO_2 measurements: explosions with ash and clouds or fog.

3.4 Errors and limitations

Remote sensing techniques which use scattered sunlight as a light source are all affected by errors due to the radiative transfer (see *section* 2.4). Single or two coupled UV cameras, in contrast to the DOAS technique, work using a small wavelength range, possibly preventing the assessment of the radiative transfer problem. Here below we will attempt at quantifying UV cameras errors on the base of the results reported by Kern et al. (2009) for wavelengths of 300 nm and 325 nm (close to those of the filters), being that radiative transfer is wavelength dependent. We'll employ the concept of "air mass factor" (see *section 2.4*) to describe the error magnitude.

UV cameras require to be placed at a lateral distance from the plume. Such distance depends on plume dimension and lens focal length. In the last three years, I used a two coupled UV camera system (see *section 4.1.1*) in different conditions (from small gas sources such as a fumarolic field, to large gas plumes issuing from open vents), and operating at distances of 0.3 – 4 km away from the gas. Figure 20

shows the dependence of AMF on distance at 300 nm and 325 nm and fora SO_2 concentration of $1.66 \cdot 10^{-3}$ ppm (corresponding to 20 ppm·m along a straight path) and no aerosols present. As distance to the plume increases, dilution (see *section 2.4*) progressively grows and the AMFs drop to values considerably below 1. This suggests that, beyond 3 km and under the plume conditions listed above, we measured less than 80 % of the real SO_2 slant column density.

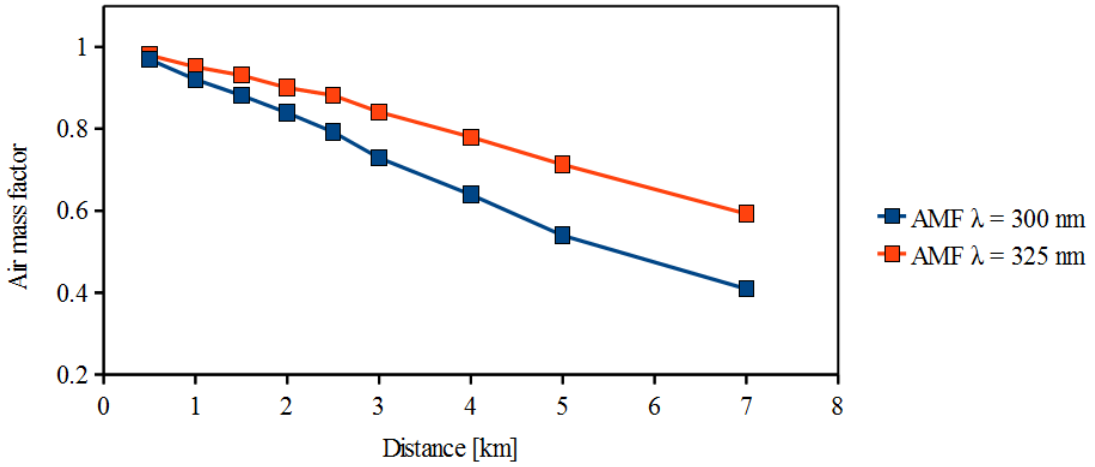

Figure 20: Air mass factor at different lateral distances and wavelenghts.

Volcanic plumes are obviously not aerosol free, and they are quite often surrounded by aerosol entrained from ambient air. Volcanic plumes transport two types of aerosol: volcanic ash and condensing water and/or sulfates-chlorides. The former produces a typically dark plume (see *section* 5.3) as a result of high absorption and low single scattering albedo (SSA). The latter give rise to a white plume since water droplets have a high albedo (SSA~1); in this case, the light entering the plume is usually scattered back with almost no-absorption. For remote sensing measurements, not only the aerosol load at the location of the plume is relevant, but also the conditions along the entire light path from the sun to the instrument. A scenario has been conceived by Kern et al. (2009) in order to model the aerosol effect on the air mass factor; an aerosol-rich and water condensed volcanic plume (SSA = 1, aerosol extinction coefficient AEC = 8 km^{-1}, SO_2 straight column density of 1000 ppm·m) was located at ~1.3 km above and at a lateral distance of 3 km from a instrument. Figure 21 shows the results for different AEC in the planet boundary level (assuming an ambient aerosol SSA = 0.8) at 300 nm and 325 nm. The importance of

the plume AEC (here supposed to be the worst case, much higher than the maximum ambient AEC considered) clearly stands out: this may lead to measure ~40% of the real SO_2 slant column density at 300 nm in a surrounding ambient aerosol-free (AEC = 0). The higher the ambient AEC, the more radiation is scattered by aerosols into the instrument's field of view between the plume and the instrument, thus diluting the absorption signal (up to ~20% of the real SO_2 slant column density at 300 nm).

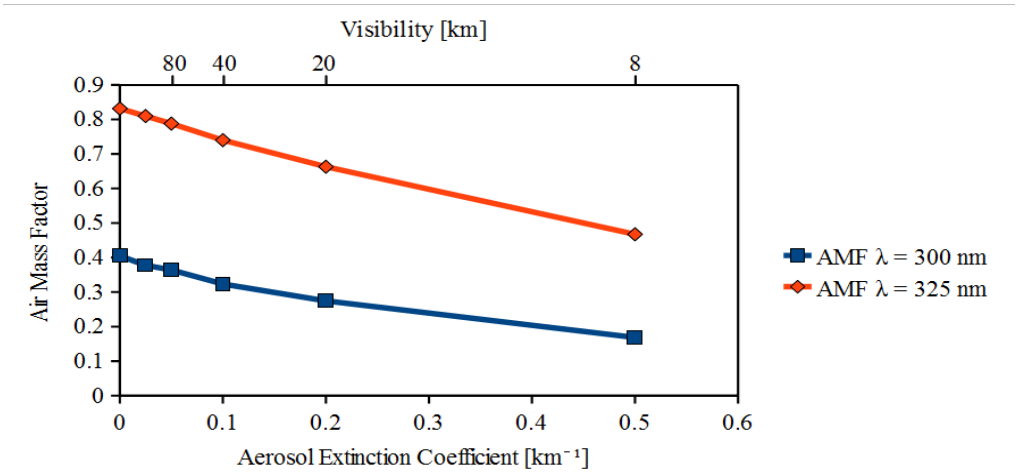

Figure 21: Air Mass Factor at different aerosol extinction coefficients (AEC) in the planet boundary layer (PBL) at 300 nm and 325 nm.

Such results show that UV camera measurements may potentially undergo considerable underestimation of the SO2 slant column density (up to 20 %) due to the cumulative effect of lateral distance and aerosol (light dilution). Accordingly, near-vent gas measurements (< 2 km) of an aerosol-free plume (no water condensation must occur) may reduce the error to < 30 % . Unfortunately, volcano summits often undergo condensation of water-rich air masses, and may easily be covered by clouds, which prevent measurements. In addition, a near-vent plume is quite often too condensed and gas-aerosol concentrated to be measured.

Chapter 4
The UV camera:
A new hardware set-up and software

4.1 UV CAMERA

4.1.1 Set-up and retrieval

Recent UV camera applications (Mori and Burton, 2006; Dalton et al., 2009; Holland et al., 2011; Nadeau et al., 2011) have used a single pass-band filtered device in order to overcome the delays due to filter switching, thus achieving a higher sampling frequency (~1 Hz). This technique is, however, potentially subject to an overestimation of the SO_2 column amount, due to combined light absorption by both gas and aerosols.

Here, I propose an alternative to previous UV camera settings, consisting of two UV cameras operating simultaneously from the same position. Two Apogee Instruments Alta U260 cameras were mounted on a steel rail atop a tripod, each coupled to a Pentax B2528-UV lens of f=25 mm focal length (FOV ~ 24°). Immediately in front of each lens, a 10 nm full width at half maximum (FWHM) bandpass filter was placed in an in house built mount, which also accommodated the quartz SO_2 cells used in the calibration (see section 4.1.3). These filters were centred on 310 nm (Asahi Spectra XBPA310; strongly affected by plume SO_2 absorption) and 330 nm (XBPA330; where SO_2 absorbs two orders of magnitude less than at 310 nm), respectively (Fig. 22).

Measurement involves capturing plume and background sky images, so to determine the qualitative measure of plume absorbance, *A*, per pixel, as described above (Eq. 3). Ideally, the sun should be behind the camera in order to create conditions of homogeneous illumination of the sky in the field of view. Meteorological clouds behind the camera field of view do not appear to be overly problematic; however clear/uniformly cloudy sky backgrounds are optimal. Clouds between the observer and plume, however, will likely render measurement impossible.

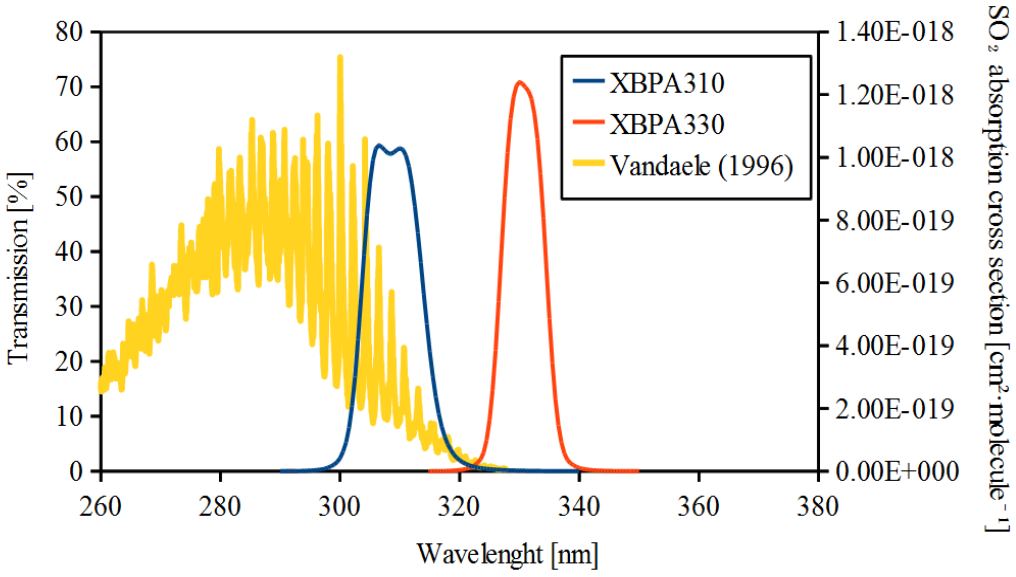

Figure 22: Sulphur dioxide absorption cross section (Vandaele et al., 1994) and trasmittance of the two filters XBPA310 and XBPA330.

The retrieval Equation 3 allows the calculation of absorbance A per pixel taking an image of SO_2-free sky as the reference. The UV camera should be oriented to at least 90° to avoid issues associated with strongly inhomogeneous illumination across the field of view; for flux computation, clear sky should be contained in the image either side of the plume. To overcome the inherent delay of taking a reference image, Equation 3 has been rearranged and simplified into the components:

$$(4) \quad A = -\log_{10}\left(\frac{IP_{\alpha}}{IP_{\beta}}\right) - \log_{10}\left(\frac{IB_{\beta}}{IB_{\alpha}}\right)$$

simply taking the logarithm of the ratio of the two vignette-corrected (see *section* 4.1.2), dark-subtracted filter images of the plume. Assuming that the second term is constant across the image, we can recast it as:

$$(5) \quad A = -\log_{10}\left(\frac{IP_{\alpha}}{IP_{\beta}}\right) + K$$

where the value K is a scalar subtracted to the resulting image to set SO_2 concentrations equal to zero in the absence of volcanic gas (clear sky). At least 75 pixels of clear sky should ideally be present in both sides of any row/column of interest for accurate computation of concentrations therein, and vignette correction is required.

Figure 23: The complete UV camera system adopted in this work.

The use of two distinct UV cameras raises the question of whether to adopting different integration times for each filter, given that the background skylight illumination is far more intense at 330 nm than at 310 nm. Here, we used the same integration time for both cameras. This was chosen to almost saturate the 330 nm filtered camera (~60000 over a maximum of 65536) to maximise the signal-to-noise ratio; thus the measured light intensity in the 310 nm was generally 85 % less (on average ~ 60000 and 9000 counts respectively). We have tested the "equal-integration" method by calibrating the UV camera with 5 quartz SO_2 cells of known concentration (see *section* 4.1.3) and the fit line R^2 was ≥ 0.99. Hence, so long as calibration is made under the same conditions as the measurements themselves, so that the appropriate ratio is used, there is no advantage here to near saturation of the 310 nm filter acquisitions. Our results are in disagreement with the lower R^2 values reported by Dalton et al. (2009) obtained from the equal-integration method. A possible exclusion to our conclusion could be for conditions of poor illumination, such that the 310nm/330nm intensity ratio is considerably lower than encountered in our measurements. Under such circumstances, it may be necessary to increase the 310 nm exposure to obtain good calibration line R^2 fitting.

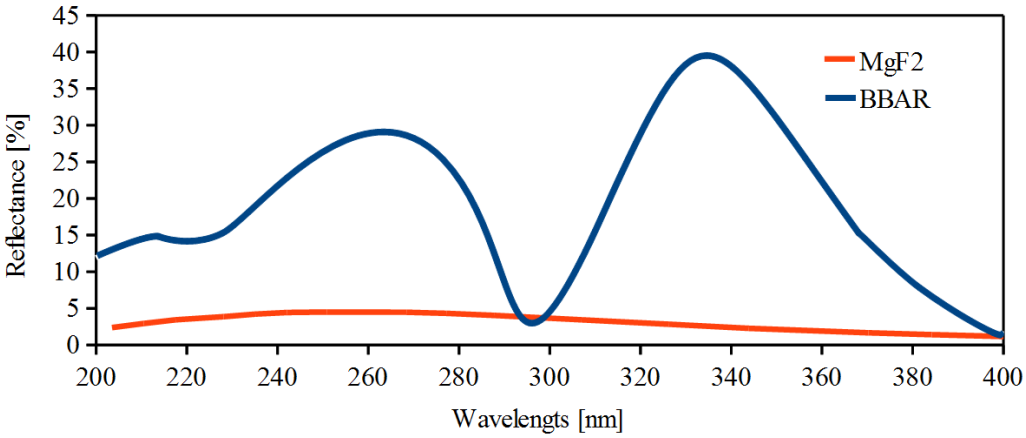

Figure 24: Reflectance of two tested CCD covering windows.

In this regard, the type of covering window that seals the CCD sensor is very important. We have tested two types of windows: the standard Broad Band Anti-Reflection (BBAR), and the MgF_2 window. The former has strong reflection (up to 40 %, Fig. 24) in the 300-340 nm wavelength range, forcing the use of higher exposure

time (> 1 s), and resulting in increased noise. We therefore recommend the use of MgF_2 windows, which have < 5 % reflectance

As mentioned above, many recent works report SO_2 flux data collected with a single UV camera, driven by the need to achieve high temporal resolution with a single device. This makes it difficult to discriminate between aerosol and gas absorbances. The two filtered UV camera technique, instead, assumes that the aerosol contribution to the attenuation of light at 310 nm and 330 nm is the same, and its effects is therefore removed by calculating the ratio, as above.

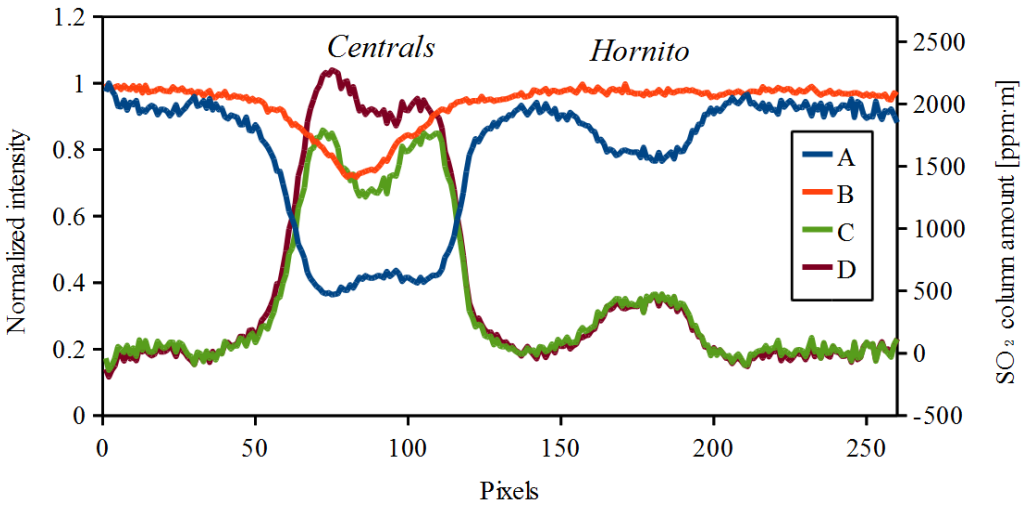

Figure 25: Plume cross-section of two central craters and an hornito close to each other taken on Stromboli on 20 May 2011.The lines A and B represent the light intensity profiles reported on the 310 nm and the 330 nm filtered cameras respectively. It is clear an attenuation of light intensity in A due to SO_2 and aerosol; the B profile highlights that the aerosol effect is strongly present in the Central plume (~50 % of the total absorption) and is absent in the hornito plume (probably resulting from low concentrations in general). The lines C and D represent instead the calculated column amount profile with the two filters and one filter methods respectively. It is evident an overestimation of the detected SO_2 in the Central plume (relative to the Hornito one) in which the aerosol effect has been quantified with the 330 nm filtered camera.

The effect of the use of either one or two filters is discussed in Figure 25. The figure reports results of a plume cross section drawn from an SO_2 image collected on Stromboli on 20 May 2011. We have calculated a concentration profile using the retrieval equation for one (D purple line in Fig. 25) and two (C green line in Fig. 25) filtered cameras from Eq. 3 and 5. The gas emitted from the central craters was aerosol-rich relative to the gas emitted from the nearby hornito, possibly resulting in a SO_2 flux overestimation of the former using a single filtered camera (D purple line in

Fig. 25). The aerosol contribution to the total absorbance is sometimes negligible , as in the case for gas emitted from the hornito, in which the one and two filtered camera methods give the same result.

4.1.2 Vignetting correction

In this study, efforts have been made to correct for the effect of vignetting on the UV camera images. In photography, vignetting is an optical effect causing the corners of an image to be darker than its centre. There are several causes for vignetting:

1. Mechanical vignetting results from the outer rim of the filter placed in front of the lenses, which partially block the light beams, and usually produce a very steep brightness attenuation;
2. Optical vignetting is an intrinsic feature of multiple element lenses and it can be completely removed by setting a small iris aperture. This is because, by using a smaller aperture, the different paths light passing through the diaphragm and reaching each pixel on the CCD are getting narrower –and equally distributed in the whole CCD area; while using a big aperture the incident light on the central regions of the CCD is larger than on the periphery (proportional to the different paths).
3. Natural vignetting (Aggarwal et al., 2001) is a problem of energy loss of the light beam passing through the lens with a non-perpendicular trajectory. The falloff f_v caused by the natural vignetting can be modelled as:

$$f_v = \cos^4(\beta) \quad (6)$$

where β is the angle between the normal to the lens axis and the direction of the light beam.

4. Pixel vignetting is caused by the angular-dependence of the CCD sensors, which produces a stronger signal from incident photons with a perpendicular trajectory.

An example of vignetting is shown in Fig. 26, corresponding to imaging of a portion of clear sky with a 310 and 330 nm pass-band filtered UV camera. It should be noted that neither is the vignetting function symmetrical across the image (Fig. 26c) - as one might expect - nor do the two lenses have the same vignetting function.

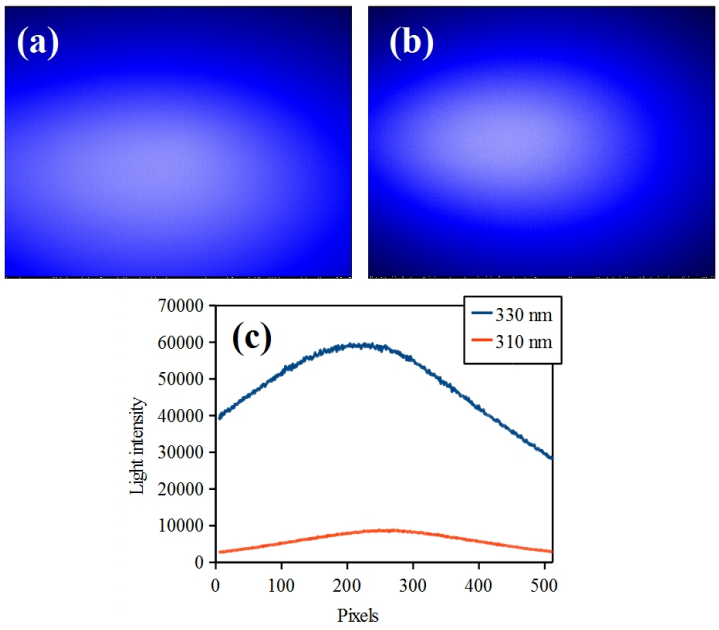

Figure 26: Vignetting effect in 310 nm (a) and 330 nm (b) filtered UV cameras and the relative intensity profiles at horizontal half-height.

Whilst vignetting can be ascertained from images containing the volcanic plume, it is better to avoid this perturbing influence upon some of the pixels, in order to have the largest possible number of data points for the analysis. The simplest way to do this is to point the camera away from the sun at a cloudless sky, at 45° zenith angle at around 10:00 or 16:00 when the sun is neither at zenith nor the horizon, so the imaged sky is uniformly illuminated (Fig. 27).

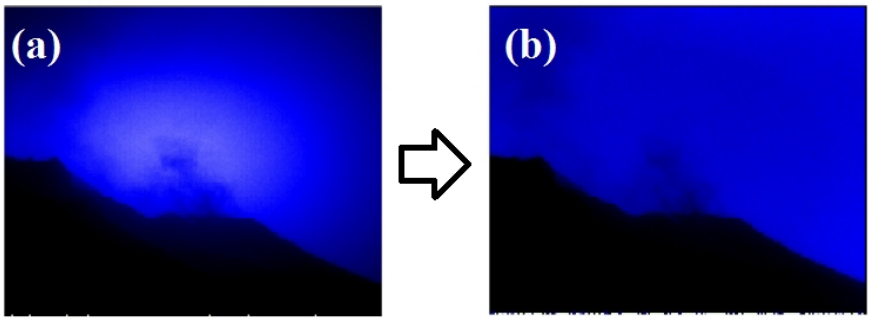

Figure 27: A vignetting correction mask has been derived from a clear-sky image and applied to (a) to get (b).

Images should be collected according to the approximate light intensity values of the plume acquisitions themselves, given the slight non-linearity in the camera response e.g., this would normally correspond to near saturating the 330 nm filter, and around 10% of the maximum counts for the 310 nm case (using the same exposure time). Once one image is collected per filter, this is normalised with respect to the maximum pixel intensity to create a mask, which all subsequently acquired images are divided by, to correct for vignetting. Here we suggest to collect as many vignetting masks as possible with different integration times during the first acquisitions, especially if light conditions vary, in order to derive a sort of library to be used to correct for vignetting in successive acquisitions.

4.1.3 Calibration

UV cameras measure the absorbance A in the presence of SO_2 molecules in the optical path of each pixel. Conversion from A (dimensionless) to SO_2 column density (ppm·m) is generally achieved using quartz SO_2 cells of known concentration. A possible calibration strategy is illustrated in Fig. 28, in which five cells have been placed together on a support, a few meters in front the camera, with clear sky as the background. The absorbance values are calculated taking an average in the centre of each cell to avoid light scattered by the edge of the cells. This calibration method allows one to check continuously the calibration coefficients, provided that there is

enough clear sky as background to image the cells and the volcanic plume simultaneously.

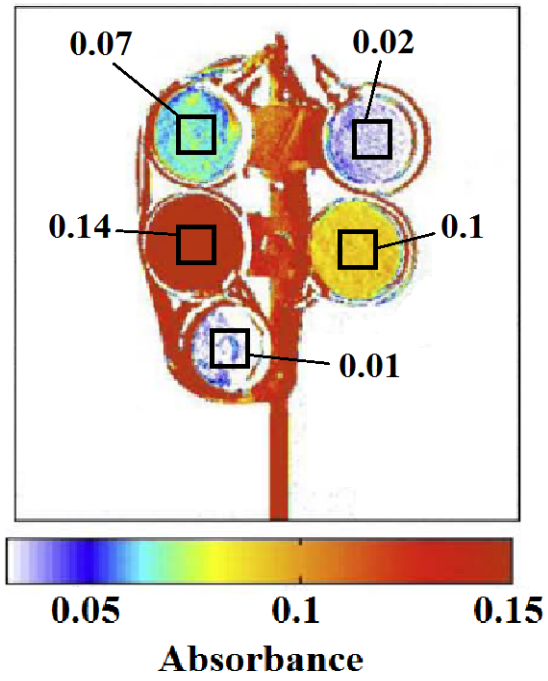

Figure 28: Calibration of a UV camera system with a single image of a whole quartz SO_2 cells set (Dalton et al., 2009).

In this study, we propose an alternative method for UV camera calibration, which requires placing the cells one by one immediately in front the lenses in order to calculate the absorbance as:

$$(7) \quad A = -\log_{10}\left[\frac{\left(\frac{IC_{\alpha}}{IB_{\alpha}}\right)}{\left(\frac{IC_{\beta}}{IB_{\beta}}\right)}\right]$$

where IC is the light intensity due to SO_2 cell absorption, and IB is light intensity of the clear sky (background). This method allows the calculation of the absorbance in a larger number of pixels (in our case, an average taken over the central 200x200 pixel section), and vignetting does not need to be corrected because the ratio minimizes the darkening of the edges. For consistency, we used cells of equal diameter (25 mm; Resonance Ltd.) of the filters, placed immediately in front of the filters in the in-

house-built mounts. The SO_2 concentration for each cell is then plotted against A, measured as above, and the gradient of the best-fit regression line is taken as the calibration ratio (Fig. 29). The latter is then multiplied by subsequently acquired plume image pixel A values to convert to ppm·m.

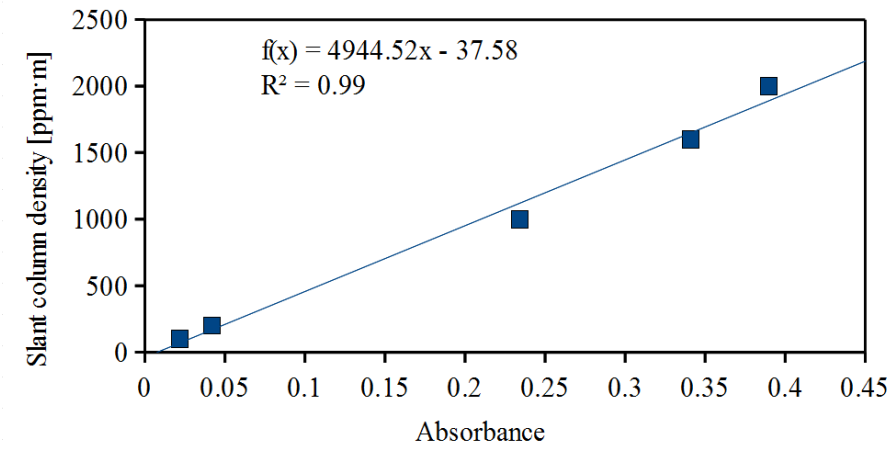

Figure 29: UV camera calibration best-fit regression line. Cells concentration are 98, 197, 1030, 1600, 2040 ppm·m respectively.

4.1.4 Pixel dimension

SO_2 flux measurements performed by traversing underneath the plume take advantage of a GPS unit for geo-referencing, which allows one to calculate the travelled distance for each spectral acquisition and processing, and finally integrated column amounts along the route. The UV camera works instead from a fixed position, and ICA is derived by integrating SO_2 column density along a line of pixels (a section through an SO_2 concentration image). The dimension p, in meters, of a pixel that is looking an object (the plume) placed at distance d from the camera can be calculated trigonometrically as follows:

$$p = \frac{2 \cdot d \cdot \tan\left(\frac{\gamma_{FOV}}{2}\right)}{512} \quad (8)$$

where γ_{FOV} is the field of view of the lens in degrees. However, p also depends on the slope of the section in the image as illustrated in Fig. 30, where the number of pixels that connects points AB and CD (gray pixels in Fig. 30), multiplied by the dimension p does not correspond to the real length of the two lines. A correction factor f can be calculated as:

$$f = \frac{\sqrt{n_v^2 + n_h^2}}{n_{MAX}} \tag{9}$$

$$p_r = p \cdot f$$

where p_r is the real pixel dimension, n_v and n_h are the number of pixels of the vertical and horizontal component of the section, respectively; and n_{max} is the number of pixel of the biggest component. The correction factor ranges from 1 to 1.415.

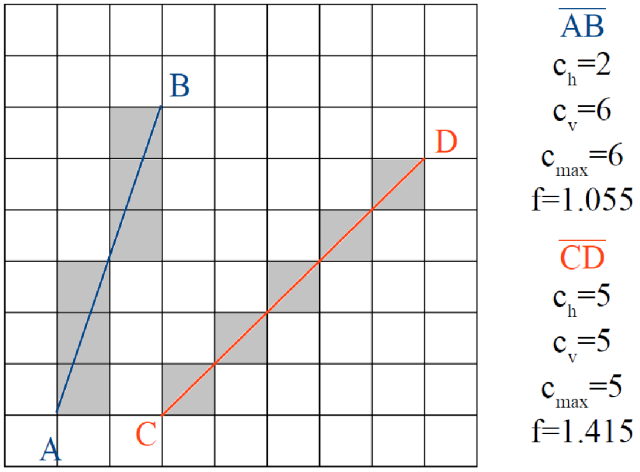

Figure 30: Difference between the number of pixels connecting two points and the real distance between them. On the right, two cases, AB and CD, and their respective correction factors.

4.1.5 Plume speed calculation

UV spectroscopic scanning systems typically calculate gas flux by multiplying the integrated amount of SO_2 distributed along a section, the so-called integrated

column amount (ICA), by an average plume speed. The calculation must thus rely upon accurate knowledge of plume velocity. As a matter of fact, a common assumption made is that the volcanic plume moves at the same speed as the wind. The latter is often measured with anemometers on the crater rim or directly on the measurement site. Recently, wind speed has also been calculated by means of mathematical and meteorological models (Burton et al., 2009). Even so, anemometer-derived plume speed data can be affected by uncertainties of 10-40 % (Stoiber et al., 1983; Williams-Jones et al., 2006) and may involve significant underestimates (Doukas, 2002).

In the last twenty years, numerous efforts have been made to directly measure plume speed using video measurement (Kyle et al., 1994), or multiple spectrometer methods (Williams et al., 2006; McGonigle et al., 2009; Boichu et al., 2010). Generally, these methods consist in calculating a time lag τ_{lag}, which corresponds to the time for a cloud of volcanic gas to travel from a start to an end point, separated by a distance ΔX. τ_{lag} will be dependent on the distance ΔX, and the velocity of the plume v_p:

$$\tau_{lag} = \frac{\Delta X}{v_p} \quad (10)$$

The UV camera represents an important step forward in the evaluation of the plume speed inasmuch as its spatial resolution, in tandem with its high temporal resolution (up to 1 Hz), make it possible to capture numerous cross-section of the plume at a given time (Fig. 31a), and to calculate the speed of rapid emissions and bursts (e.g. Strombolian explosions, gas puffing). Here, we propose three different methods for calculating the speed of a volcanic gas plume:

1. ICA time-series cross-correlation;
2. In-plume cross-correlation;
3. Evaluation frame by frame;

The ICA time-series cross-correlation (McGonigle et al., 2009; Boichu et al., 2010) consists in calculating the variations over time of integrated column amounts related to two parallel plume cross-sections, separated by a distance ΔX. Thus, the two time-series, which are similar to each other, will exhibit a delay τ_{lag} as mentioned above. In order to calculate the plume speed, the time-lag can be calculated with cross-correlation methods.

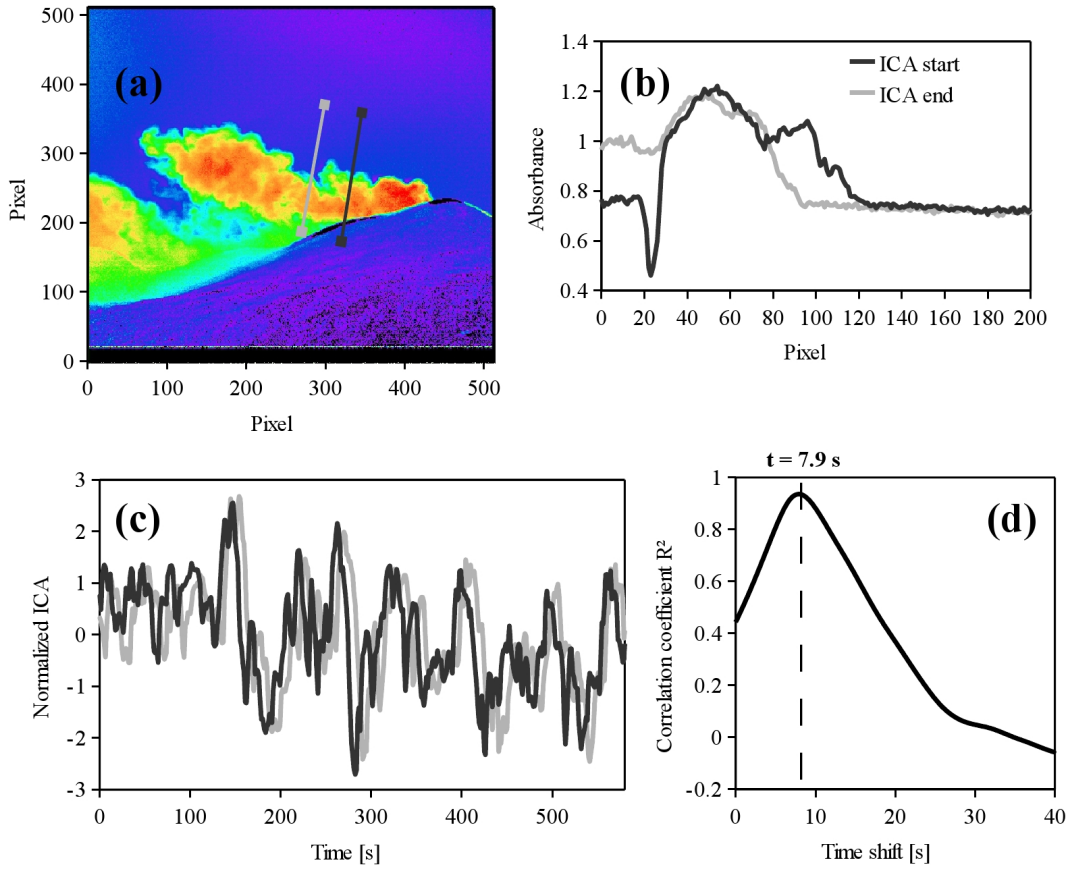

Figure 31: (a) SO_2 column amount image of the NE crater (Etna) and two cross-sections perpendicular to the plume and parallel to each other (light and dark grey lines). (b) The column amount profiles and the calculated ICA time series (c) relative to the two previous cross sections. (d) A cross correlation function resulting from the two ICA time series, the calculated time-lag is 7.9 s.

Cross-correlation is the mathematical method of estimating the similarity of two signals as a function of a time-lag applied to one of them. It is defined by continuous functions having the form:

$$(11) \quad (f \cdot d)(t) = \int_{-\infty}^{+\infty} f*(\tau)\, g(t+\tau)\, d\tau$$

that is simply a moving dot product along time. *(f·g)(t)* global maximum corresponds to the value of τ at which f and g exhibit the best match. The cross-correlation of a signal with it-self is called auto-correlation, and is useful to investigate possible signal periodicity, the maximum value of this function is always at τ=0.

Vulcamera (Section 4.2) includes a tool for calculating the cross-correlation coefficients between two ICA time-series, as shown in Fig. 31. The consecutive steps are (i) to set the "start cross-section", placing it as perpendicular as possible to the plume transport direction (Fig. 31a, dark grey line); (ii) to define the plume transport direction (in zenith degrees) and finally (iii) to set the distance ΔX (in pixels) between the two parallel sections, to locate the "end cross-section" (Fig. 31a, light grey line). *Vulcamera* will automatically calculate two normalized ICA time-series (Fig. 31c), which will then be shifted with a step of 0.1 seconds to estimate the cross-correlation function (Fig. 31d). The example shown in Fig. 31 refers to Etna's North-east crater's plume, for which the cross-correlation function shows that τ_{lag} is 7.9 s: taking into account that ΔX is 88 m, then the mean plume speed in that interval is ~ 11 $m \cdot s^{-1}$. Vulcamera also has zooming tools allowing for the calculation of cross-correlation functions in shorter time intervals, to manually locate plume speed variations with time.

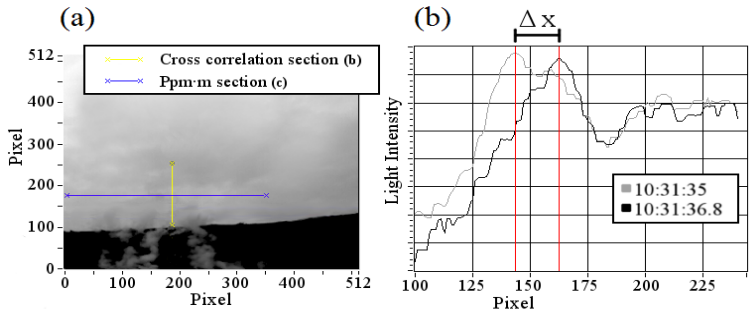

Figure 32: (a) UV image (310 nm filtered) of a fumarole of La Fossa crater (Vulcano island, Italy). The 310 nm filtered image (in which SO_2 absorption occurs) was used for cross-correlation operation (and thus plume speed derivation), because it displays a larger pixel-to-pixel intensity variation than the ratio image. The yellow line shows the section of the image along which the cross-correlation is performed. (b) The plots show pixel-to-pixel intensity variations along the yellow sections taken in two consecutive 310 nm filtered images. From the pixel shift (ΔX) between the gray and black line (this taken along the same yellow section but after an interval ΔT of 1.8s), the mean speed in that interval was calculated.

An alternative method we used consists in the direct estimation of the gas displacement through the analysis of a sequence of absorbance profiles parallel to the plume transport direction, as shown in Fig. 32 (a, b). We have tested this method in the fumarolic system of Vulcano (Aeolian islands, Italy), where the low fluxes of individual fumaroles, and their relatively rapid dispersion, did not allow the calculation of two separated ICA time-series with shared inhomogeneities, as shown in the Etnean example above. In Fig. 32, we show a vertical rising plume case in which we can identify some features in the first absorbance profile (light gray line in Fig. 32b), which is preserved in the consecutive frame (black line in Fig. 32b) taken after 1.8 s. This condition allows the calculation of ΔX by means of cross-correlation.

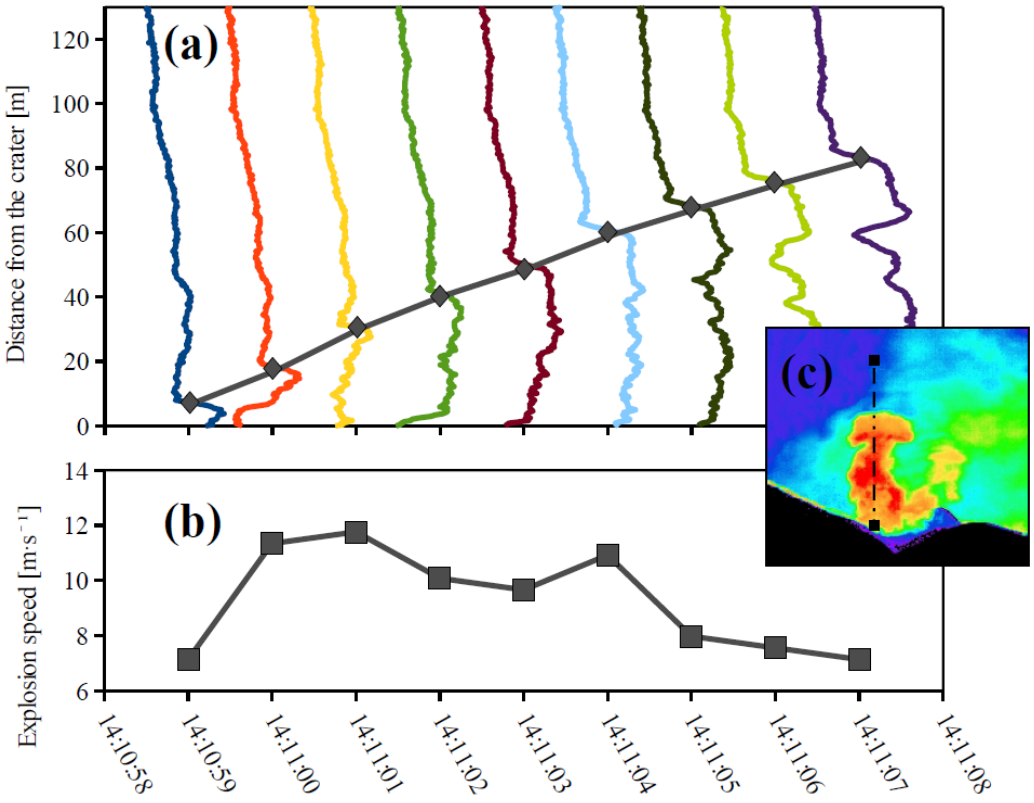

Figure 33: (a) Time variations of a normalized SO_2 column amount profiles (multi-colour lines). The grey line shows the different positions of the explosion front . (b) The frame-to-frame calculated explosion front speed. (c) A SO2 column amount image and the location of the cross-section.

These cross-correlation techniques are no longer effective when plume speed changes rapidly over a wide range (from >20 to <5 $m \cdot s^{-1}$), as in the case of gas bursts

and Strombolian explosions, in which even a sampling frequency of 1.2 Hz is insufficient. Consequently, in such cases, gas speed variations have been calculated manually looking the movements of the explosion front over in-plume sections (Fig. 33)

4.1.6 SO_2 mass measurement

Non-passive degassing is a recurrent mechanism of energy dissipation at open-vent volcanoes. It consists of the emission of over-pressurized gas pockets, in either bursts or puffs (Harris and Ripepe, 2007). This rapid emission creates a cloud of concentrated gas that is clearly detached from the vent (Fig. 34), and rises faster then the surrounding gas. After a few seconds or minutes, depending on the concentration of the gas, this gas pocket mingles with the surrounding plume(s), and disperses in the atmosphere.

Figure 34: Gas puff from the central crater of Stromboli (Italy).

The evaluation of the gas content in explosive bursts or *puffs* is challenging, in view of the short timescale of the process. In fact, the standard scanning spectroscopic methods have time resolution inadequate to resolve these phenomena. Recently, the development of cylindrical lenses DOAS and UV cameras has opened the way to measurement of SO_2 flux at high-frequency (up to 1 Hz). The resulting time-series can

be subsequently integrated (Fig. 35), from the onset of a given gas burst or puff, until the end of that emission (McGonigle et al., 2009, Kazahaya et al., 2011), to calculate the total mass of this individually released gas pocket.

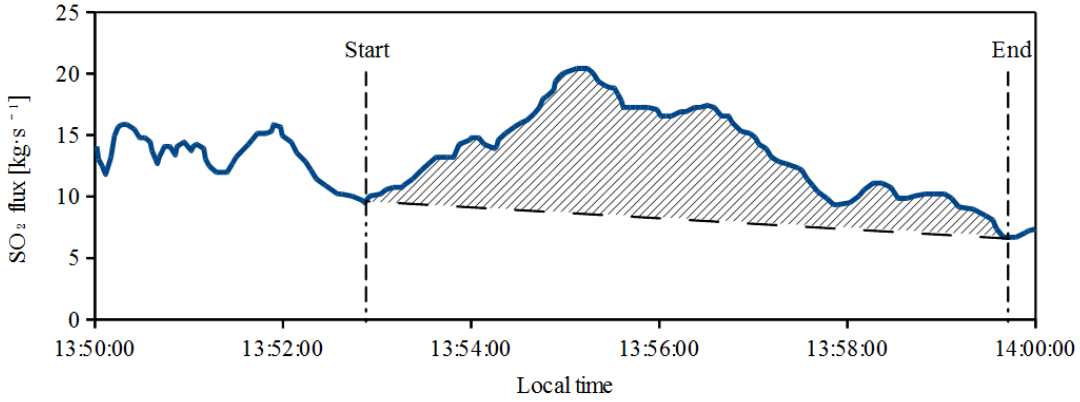

Figure 35: SO_2 flux increased after a Strombolian explosion. The shaded area corresponds to the total SO_2 mass emitted during the event (Kazahaya et al., 2011).

This evaluation may lead to some errors, however, reflecting uncertainties on the precise timing of the event's termination (an explosion or puff can not be completely detached from the in-coming gas at the source vent), and the relatively poor accuracy in determination of the puff/burst ascent rate (especially when this changes over a wide range, and rapidly).

UV cameras provide knowledge of the concentration distribution along two dimensions, yielding simple localization of volcanic gas in the atmosphere. As discussed before, calculation of the integrated column amount results from 1d-integration along a cross-section $C(x)$. By integrating a second time along the dimension y perpendicular to $C(x)$, therefore yielding $C(x,y)$, one can calculate the integrated volume amount (IVA), e.g., the cumulative amount of SO_2 within an imaginary prism of infinite thickness (see gray dotted square in Fig. 36):

$$(12)\ IVA[kg] = \int_{x_i}^{x_f} \int_{y_i}^{y_f} C \cdot dxdy$$

The variations of the gas mass calculated inside a fixed area during passive degassing are negligible if compared to the variations of the gas mass related to an explosion. To calculate the gas mass explosively released during a given burst, the procedure thus requires identification of a background gas mass. This represents a baseline SO_2 mass that has to subtracted from the total measured gas mass (Fig. 36) to obtain the explosive contribution. Notably, this technique does not require knowledge of plume speed, thus overcoming the difficulties encountered in previous studies.

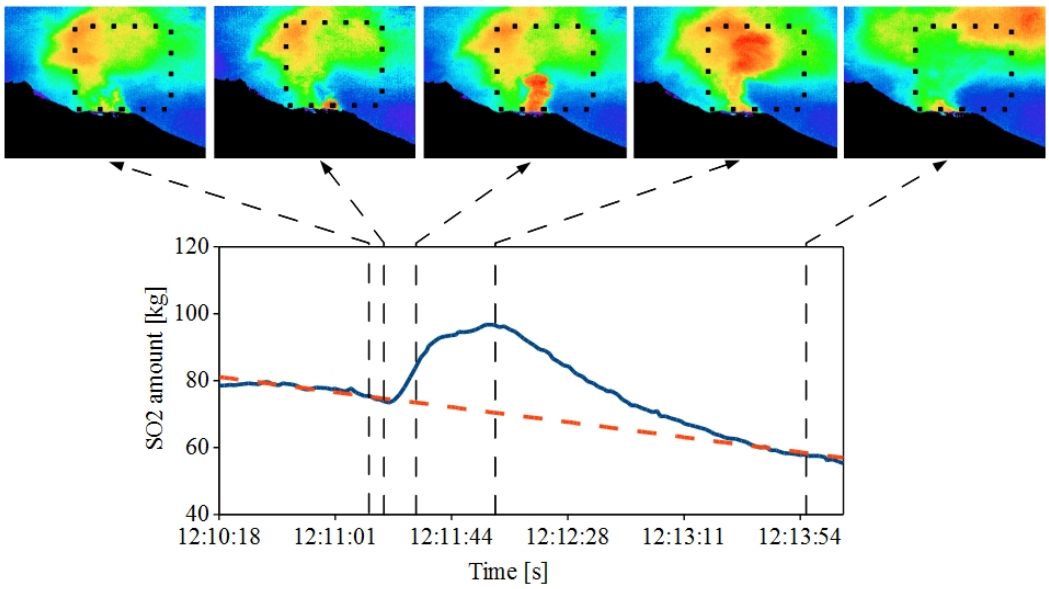

Figure 36: SO_2 column amount image sequence during a Strombolian explosion and the relative variation of the SO_2 mass, obtained from the integration inside the dotted square. The final SO_2 mass value is derived by subtracting from the maximum value of the SO_2 amount profile (4^{th} frame in the sequence) the corresponding interpolated background (orange dashed line).

4.2 VULCAMERA: A USER-FRIENDLY PROGRAM FOR SO_2 IMAGING

The Apogee Alta UV camera is a USB device, generally controlled with a commercial program called MaxIM DL (Diffraction Ltd, http://www.cyanogen.com). This code has been built for laboratory use, and has numerous limitations for field use.

In this study, I have developed *Vulcamera* (Fig. 37), a stand-alone, user-friendly code for measuring volcanic SO_2 fluxes with UV cameras. The code consists of two elements: *Vulcamera_aq* and *Vulcamera_post*, which manage image acquisition and post-processing, respectively. Vulcamera is freely downloadable from https://sites.google.com/site/giancarlotamburello/, where detailed instructions are also given. *Vulcamera* will work with Apogee Instruments U260 and E6 units; however, we recommend use of the U260, given its higher signal-to-noise ratio and faster data transfer. *Vulcamera* is designed to operate with two cameras, simultaneously, with bandpass filters centred on 310 nm and 330 nm. It is imperative to use two filters in these observations, to compensate for aerosol attenuation/backscattering, and to minimize temporal mismatches associated with filter changes on a single camera (Kantzas et al. 2010).

In particular, the functions of the code include: characterization of vignetting via the collection of clear sky images to compensate for angular dependency of pixel illumination; determination of calibration relationships between absorbance and SO_2 cell concentrations, to enable conversion of the measured field images into ppm·m concentration images; use of simultaneously acquired spectroscopic SO_2 flux data to calibrate the images; and, finally, feeding back of all of these operations to the main page of *Vulcamera_post*, which leads to the calculation of SO_2 flux time series and/or gas masses associated with explosions. *Vulcamera* has been extensively field tested at southern Italian volcanoes, and it is hoped that others will find it useful to contribute to realizing the significant volcanological potential of UV camera technology.

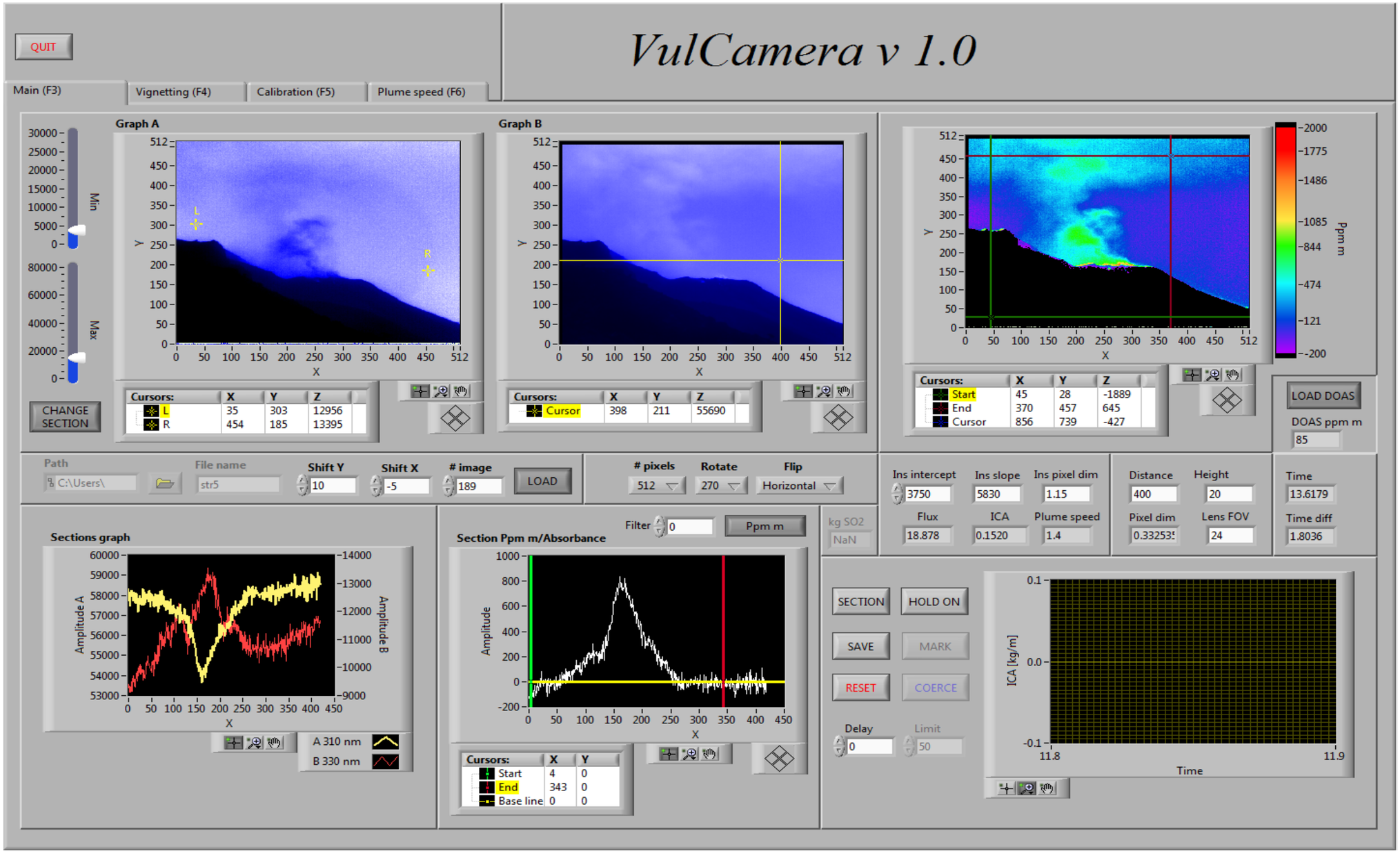

Figure 37: A screenshot of Vulcamera's post processing main menu. "Graph A" and "Graph B" blue-scale images show the 310 nm and 330 nm filtered UV camera images already vignetting corrected.The pseudo-colour graph on the right shows the SO_2 column amount image calculated with the equation 5. The "Sections graph" plot shows the light intensity values of the 310 nm and 330 nm camera of a cross-section connecting the two yellow cursors (L and R) in "Graph A". "Section ppm m/Absorbance" graph shows the calculated SO_2 column amount profile.

4.3 DOAS-UV CAMERA COMPARISON

As a means of further quantitative evaluation of the camera performance, we executed an ad-hoc designed field survey on Etna volcano, where we compared our camera observations with those from a scanning spectrometer system, of 1.8° step, as detailed in McGonigle et al. (2003), and containing an Ocean Optics USB2000+ (Kantzas et al., 2009). The spectral data were processed using the UVolc code (Kantzas et al., 2011), a development of volcanoSO2.exe (McGonigle, 2007) which provides better spectral fitting and wavelength and line width alignment.

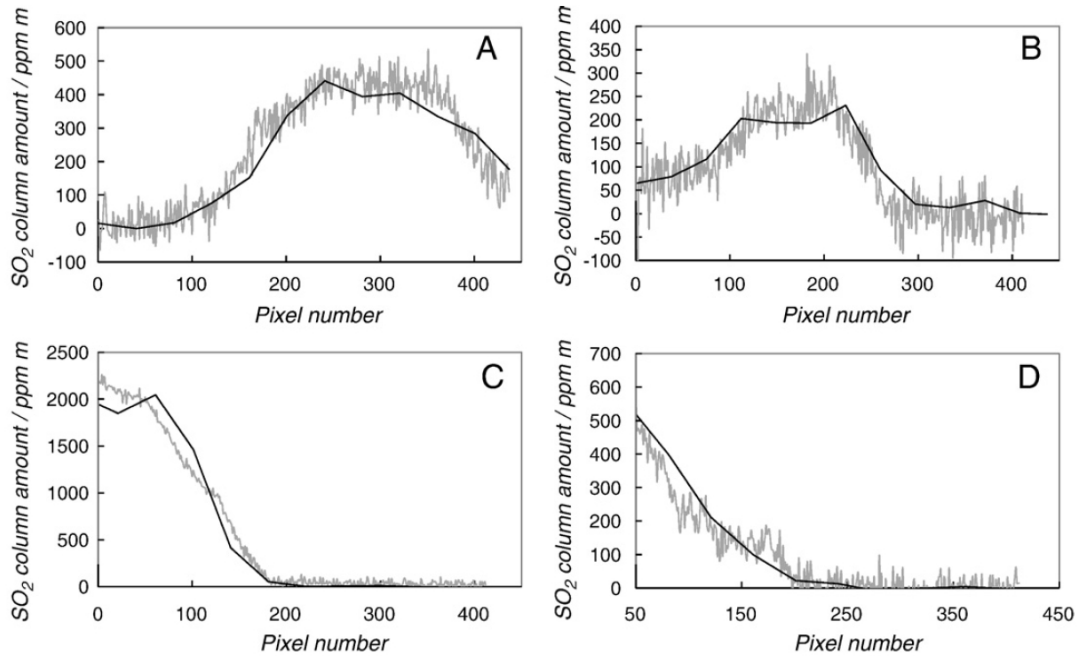

Figure 38: Example of retrieved plume concentration profiles from the UV cameras (in grey) compared against those from a scanning spectrometer (in black). Each angular concentration datum from the latter is projected onto the corresponding camera pixel value, demonstrating broad methodological agreement in all cases. Data were captured at ~12 km from the gas (A and B), and ~1 km away (C and D), respectively. The plume was at low elevation for plots C and D, such that the whole cross section could not be captured. Whilst saturation will affect the highest retrieved concentrations in C, this effect should apply to the spectrometer and camera observations in a broadly similar fashion, therefore perturbing the absolute retrieved concentrations, but not the integrity of the intercomparison (Kantzas et al., 2010).

During the experiment, the optical axes of the scanner and cameras were affixed at right angles to a machined bar, so to scan through profiles of the horizontally advecting plume, corresponding to the central pixel column of the camera FOV at

locations 1 km and 12 km from the gas. In all cases the plume was viewed approximately orthogonally to its propagation vector. Some thirty such profile inter-comparisons were performed, demonstrating broad agreement (typically within ~15%) in all cases, such as in the sample plots shown in Fig. 38. This provides confidence in the inter calibration of both approaches, hence the scope of the UV camera to succeed spectrometer based SO_2 flux observations (e.g., McGonigle et al., 2002; Galle et al., 2003), under appropriate circumstances.

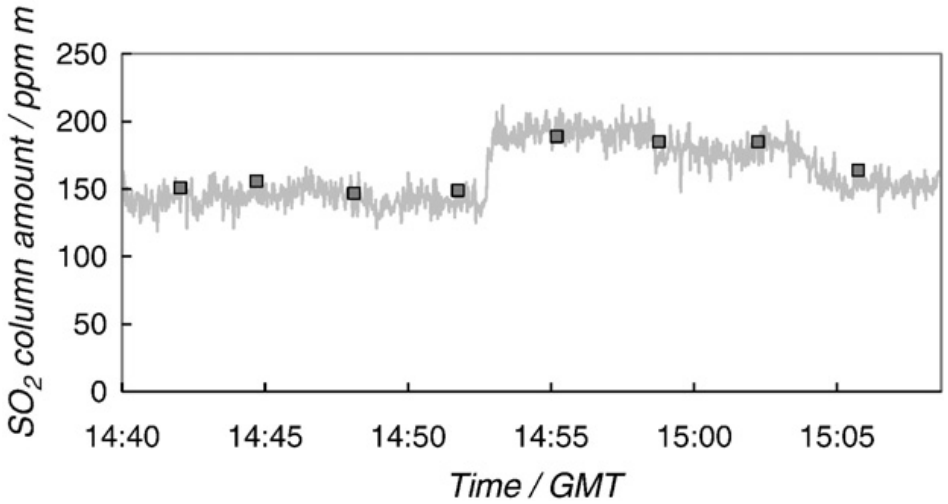

Figure 39: Time series of average concentrations across the plume profile for scanning spectroscopic observations (square points), versus SO_2 columns from a rectangular field of view spectrometer (higher time resolution grey data series) set to match the plume width. The observed agreement provides additional confidence in the latter approach as an alternate to the UV cameras for acquisition of high time resolution SO_2 fluxes, albeit demanding more complex alignment (Kantzas et al., 2010).

Further work now remains in advancing the efforts of Kern et al. (2009) in considering the exact under or overestimations incurred in both the spectroscopic and camera based SO_2 retrievals, caused by in-plume and between plume and observer UV scattering. Future lines of enquiry could involve characterising these errors using spectroscopic data then using this information to correct parallel UV camera concentrations. As part of this exercise we also compared mean scanner concentrations across the plume profile, measured 12 km away, against those from a USB2000+, coupled to a telescope of rectangular, vertically oriented, FOV (~0.3°×14°), spatially filtered to match the ≈12° vertical width plume. Pairs of the

latter have been applied to generate integrated column amounts, with multiplication of the outputted concentrations, taken as proxies for the mean column amount across the field of view, by the field of view length at the plume distance. Such data have been used to generate high time resolution SO_2 fluxes, by analogy to the camera methodology mentioned in *section* 2.3.3 (McGonigle et al., 2009; Boichu et al., 2010). In our experiments, good correspondence was found between the mean scanner concentrations and those from the rectangular field of view instrument, e.g., as shown in Fig. 39.

4.4 UV CAMERA CALIBRATION USING DOAS

In section 4.1.3, we have discussed two methodologies for UV camera calibration using quartz SO_2 cells of known concentration. Unless there is enough clear sky as background to be able to image both the plume and a whole set of calibration cells (Fig. 28), the operator is forced to rotate the field of view of the UV camera to look the SO_2-free sky. This condition is quite often encountered in the field, where the volcanic gas may diffuse over large part of a volcano's summit, therefore decreasing the chance of simultaneous calibration. As the calibration should be performed as frequently as possible, this would imply breaks during acquisition, and therefore a data gap.

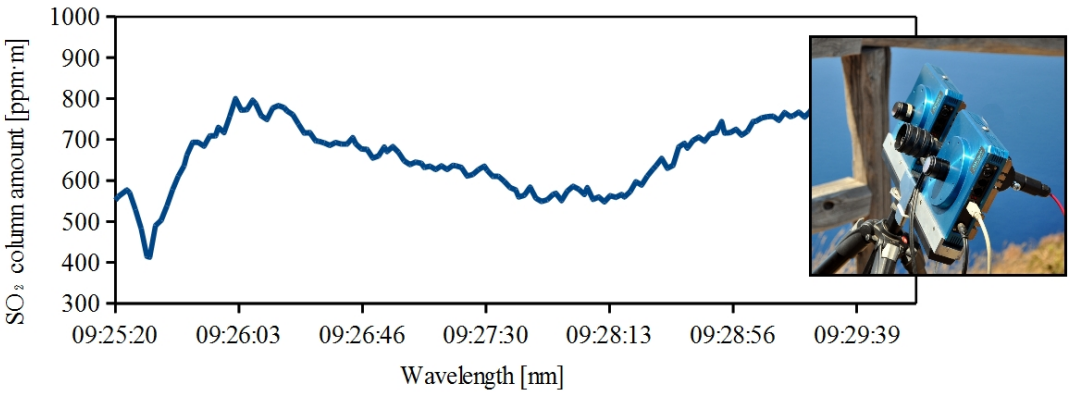

Figure 40: SO_2 column amount time-series resulting from a DOAS system with a telescope (photo on the right) pointing a fixed point in the middle of a rising gas plume.

Here, we illustrate the use of an alternative calibration technique, based on the simultaneous use of UV camera and DOAS (first reported by S. Illing et al., Volcanic plume observations with a SO_2 camera at Popocatepetl and Colima, Mexico; poster presented at IAVCEI 11th gas workshop, Kamchatka, Russia, 2011). The method makes use of a telescope pointing at the gas plume, in order to obtain SO_2 column amount time series (Fig. 40). The telescope should be located between the two UV camera to ensure identical alignment (usually located on the centre of the image). The acquired spectral data from DOAS are later processed using the UVolc code (Kantzas et al., 2011), to obtain a series of spectra $s_i(\lambda)$ each associated with a specific SO_2 column amount c_i (in ppm·m) (calculated as outlined by Kantzas et al., 2011). Then, the procedure involves multiplying the two UV camera's filter functions $f_{310}(\lambda)$ and $f_{330}(\lambda)$ by each spectrum function (Fig. 41a) to get two scaled filter functions $f'_{310,i}(\lambda)$ and $f'_{330,i}(\lambda)$ (Fig. 41b). Finally, one can calculate the absorbance A as:

$$(13)\ A_i = -\log_{10}\left(\frac{\int f'_{310,i}(\lambda)\,d\lambda}{\int f'_{330,i}(\lambda)\,d\lambda}\right)$$

The derivedSO_2 cell column amounts c_i are plotted against absorbance A_i as shown in Figure 41, and the gradient of the best-fit regression line is taken as the calibration ratio. The example shown in Figure 41c, supports fair agreement between DOAS-derived and quartz SO_2 cell-derived calibration coefficients.

This methodology opens the possibilities of continuous UV camera acquisition during daylight . Nonetheless, some linearity problems in DOAS calibration have been reported during our measurements, which will require further attention.

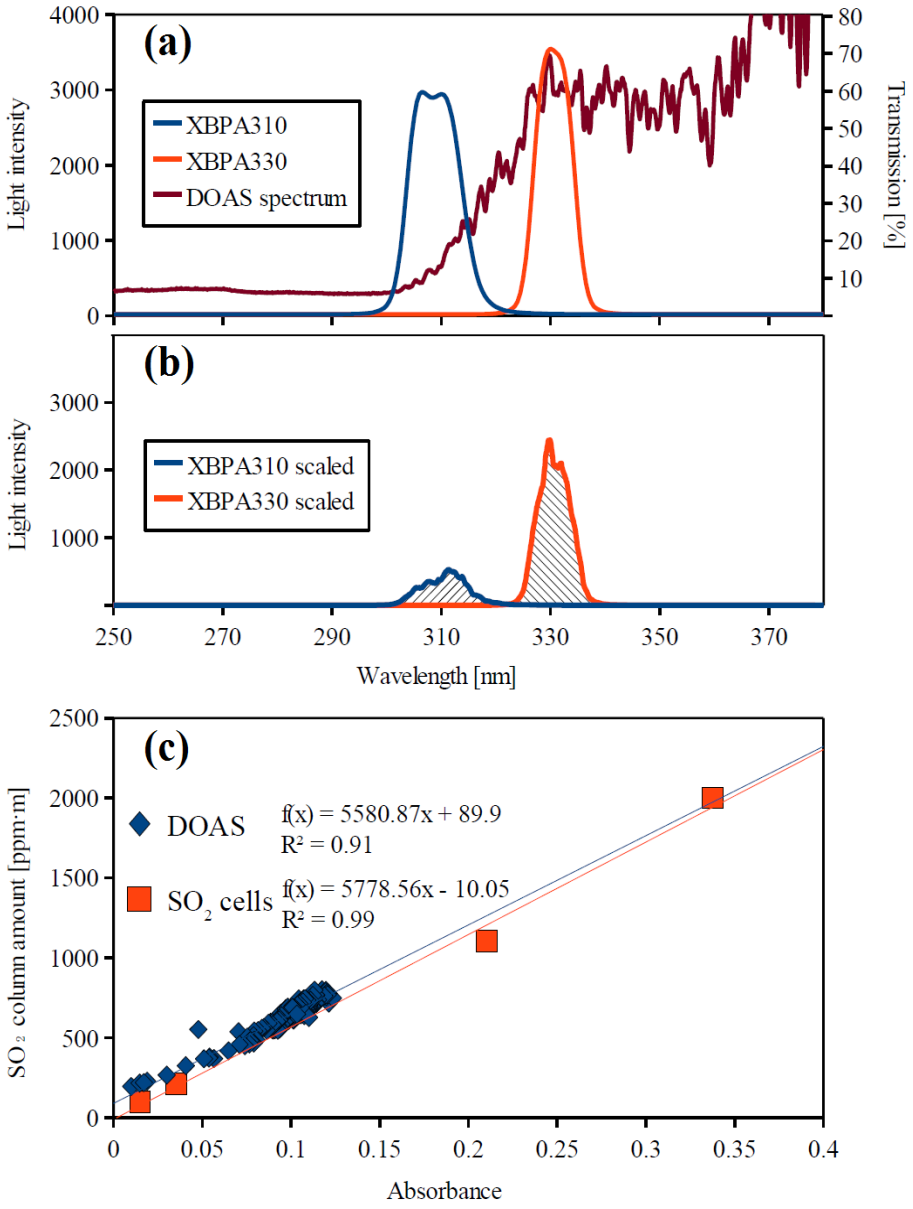

Figure 41: (a) Transmittance of the two filters adopted in our UV camera system and a UV spectrum obtained with a DOAS system in presence of SO_2. (b) The result of the product between the filter functions and the DOAS spectrum, the negative logarithm of the ratio between the integrals of the two functions represents an absorbance. (c) Plot and fit line between the calculated absorbances and the SO_2 column amount with the DOAS system (blue diamonds) compared with to the calculated quartz SO_2 cells, calibration line of the UV camera system.

Chapter 5
Applications to active volcanoes

5.1 Vulcano, Stromboli and Etna

I report below the results of application of the dual UV camera to the southern Italian volcanoes in various volcanological contexts: Vulcano and Stromboli (aeolian islands) and Etna. This allowed us to test the UV cameras potential and to explore in novel ways the degassing mechanisms and dynamics of these volcanoes.

5.2 Measurements of fumarole field degassing (La Fossa crater, Vulcano, Island)[1]

5.2.1 Introduction

The rate of SO_2 release from active volcanoes (SO_2 flux) is an important parameter for volcano monitoring, acting as a proxy for underground magma ascent rate, thus strongly correlating with eruptive activity (Caltabiano et al., 1994). Since the 1970s, COSPEC (Caltabiano et al., 2004) and more recently DOAS (McGonigle, 2007) have been the most widely used techniques for ground-based SO_2 flux monitoring. These are applied by scanning across the plume cross section, (McGonigle et al., 2003), or traversing beneath the plume with a vehicle, boat, aircraft, or an unmanned aerial vehicle (McGonigle et al., 2008). The derived concentrations are integrated over the profile, then multiplied by plume transport speed to output flux.

In spite of their utility, the scanning and traverse techniques are both subject to several significant limitations: the plume speed is typically assumed to be equal to wind speeds, measured with distal anemometers, contributing to high (potentially >100 %) and usually un-quantified errors (McGonigle et al., 2005b). Moreover, the low time resolution of both techniques hampers detection of flux changes related to transient (≤ tens of seconds) degassing-driven volcanic phenomena, such as strombolian and vulcanian explosions (McGonigle et al., 2009). In addition, the low spatial resolution of scanning/traverse methods prevents the observer from discriminating between multiple source SO_2 emissions, in particular when they are weak and closely spaced.

[1] Article published on Journal of Volcanology and Geophysical research, 2010, vol 199, 47-52, doi:10.1016/j.jvolgeores.2010.10.004

Here we augment the increasing usage of the UV camera to derive bulk plume SO_2 flux data, with, to the best of our knowledge, the first application of the camera to investigate the complex structure of fumarolic systems.

In this study, we follow the protocol for UV camera measurement described in *chapter* 4 to image the structure of the fumarolic field of La Fossa crater (Vulcano island, Aeolian islands), a small (386 m high) pyroclastic cone in a state of degassing unrest since the late 1970s (Chiodini et al., 1995). In particular, we show that the UV camera can be used to derive volcanic SO_2 flux data from individual vents within a fumarolic system, and their relative contribution to the bulk emissions. Our measurements were obtained during field surveys performed in November 2009 and February 2010, respectively around the time of an anomalous degassing (heating) event between October and December 2009. In tandem with observations during previous unrests at La Fossa since 1988 (Chiodini et al., 1995), the 2009 degassing event was marked by an increase in fumarole temperature, gas/steam ratio and CO_2 concentrations (Istituto Nazionale di Geofisica e Vulcanologia, Sezione di Palermo, unpublished data, 2009). In order to complement our analysis, and derive insights into the 2009 degassing event, we used a portable gas analyser (MultiGAS) (Aiuppa et al., 2005a; Shinohara et al., 2005) which permitted the real-time in situ measurement of H_2S/SO_2, CO_2/SO_2 and H_2O/SO_2 molar ratios. This, in tandem with the SO_2 fluxes, provided the first assessment of CO_2, H_2S (Aiuppa et al., 2006b; Aiuppa et al., 2005b) and H_2O emission rates from individual vents of the fumarolic field of La Fossa crater, both during and after the unrest.

5.2.2 Hardware and technique: UV camera and Multi-GAS

The UV camera approach, in common with DOAS, is a passive remote sensing methodology that measures sunlight scattered in the atmosphere towards the sensor. As the light path is not absolutely defined this can introduce errors in the estimation of slant column densities, which have been little considered hitherto. In *section* 2.4 We

have focused on two aspects of this: the dilution effect and multiple scattering in the plume. The former is exacerbated at large plume–instrument distances and the latter by elevated plume aerosol concentrations. In our study, UV camera measurements were made only ~300 m from the gas and the thin plume was highly transparent, hence we consider errors here to be minimal. As the plume transport speed is defined accurately, using cross correlation, we estimate each flux to suffer errors of only ±15%, therefore. The calibration was performed immediately prior to each acquisition viewing SO_2-free sky at 45° zenith angle adjacent and away from the fumarolic field, from the measurement location. In both campaigns, the calibration fit line R^2 was ~0.999.

The applied in house built Multi-GAS (Aiuppa et al., 2005) unit combined an infrared spectrometer for CO_2 determination (Gascard II, calibration range 0 - 4000 ppmv; accuracy ±2%; resolution, 0.8 ppmv), electrochemical sensors for SO_2 (City Technology, sensor type 3ST/F, calibration range, 0 - 200 ppmv, accuracy, ±2%, resolution, 0.5 ppmv) and H_2S (SensoriC, sensor type 2E, calibration range, 0 - 50 ppmv, accuracy, ±5%, resolution, 0.7 ppmv), and temperature and relative humidity sensors (Galltec, measuring range, 0 – 100 % Rh, accuracy, ±2%). The readings from the latter two were used to calculate water concentration (in ppmv), assuming a constant standard pressure, with the following equation:

$$H_{2O}[ppmv] = 0.61356 \cdot e^{\left(\frac{17.502 \cdot T}{240.97+T}\right)} \cdot Rh \cdot 100 \quad (14)$$

During the measurements, the fumarolic gas was continuously pumped into the sensors at a flow rate of 1 lpm through a PTFE tube. A data-logger board captured signals from the sensors every two seconds , while a hand-held GPS provided geo-referencing of each datum. The Multi-GAS was powered by a 12 V, 7 Ah lead battery, and housed inside a waterproof box (30 × 20 × 15 cm).

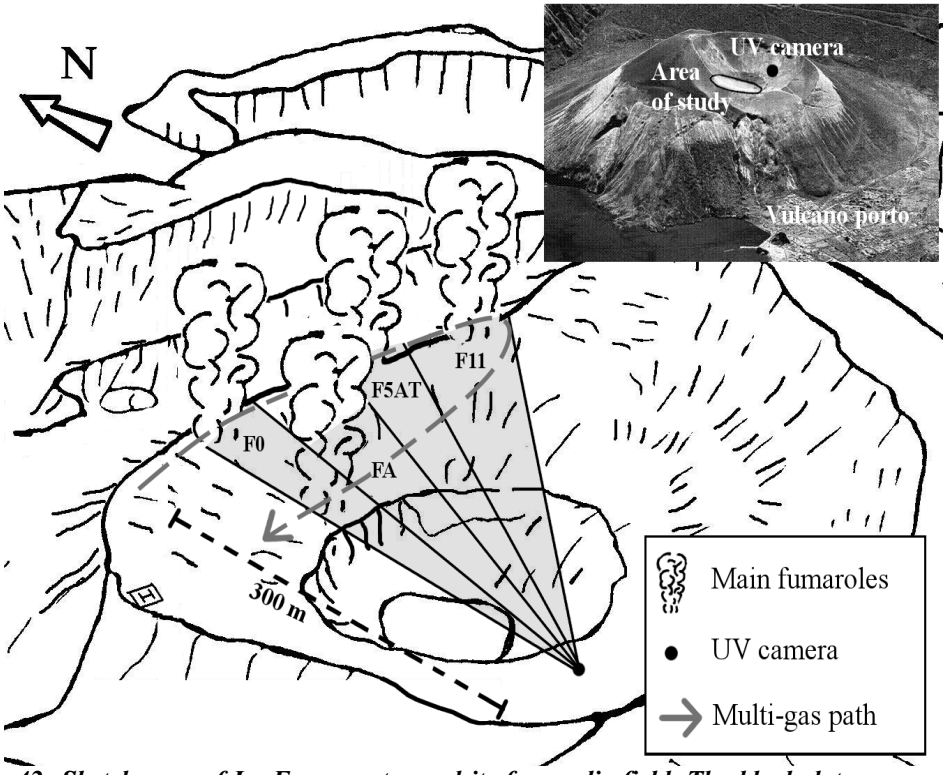

Figure 42: Sketch map of La Fossa crater and its fumarolic field. The black dot represents the site of UV camera observations. The dashed gray line marks the walking path through the fumarolic field taken during the Multi-GAS survey.

Multi-GAS measurements were performed traversing by foot through the fumarolic field (Fig. 42) with the inlet tube 30 - 50 cm from the ground. Using this methodology, we derived the H_2S/SO_2, CO_2/SO_2 and H_2O/SO_2 molar ratios for each fumarole from the gradient of the best-fit regression lines in scatter plots . For more details on this technique see Aiuppa et al. (2005).

5.2.3 Results

5.2.3.1 UV CAMERA MEASUREMENTS

The fumarolic field of La Fossa crater is 0.045 km^2 wide. Therefore, the best way to image it entirely via the UV camera, while distinguishing individual fumaroles

and using sky as background, is by observing from the southern inner crater's ridge, ~ 300 m away from the main exhaling area (Figs. 42 and 43).

During the two field campaigns, we sequentially collected images of the four main fumaroles (FO, FA, F5AT, F11; Figs. 42, 43) from the measurement position by progressively rotating eastward the UV camera. In both days, imaging of the entire fumarolic system (from F0 to F11 in a W to E cross section) was completed in ~20 minutes, and each fumarole was observed for periods of 1 to 6 minutes taking an image every ~2s.

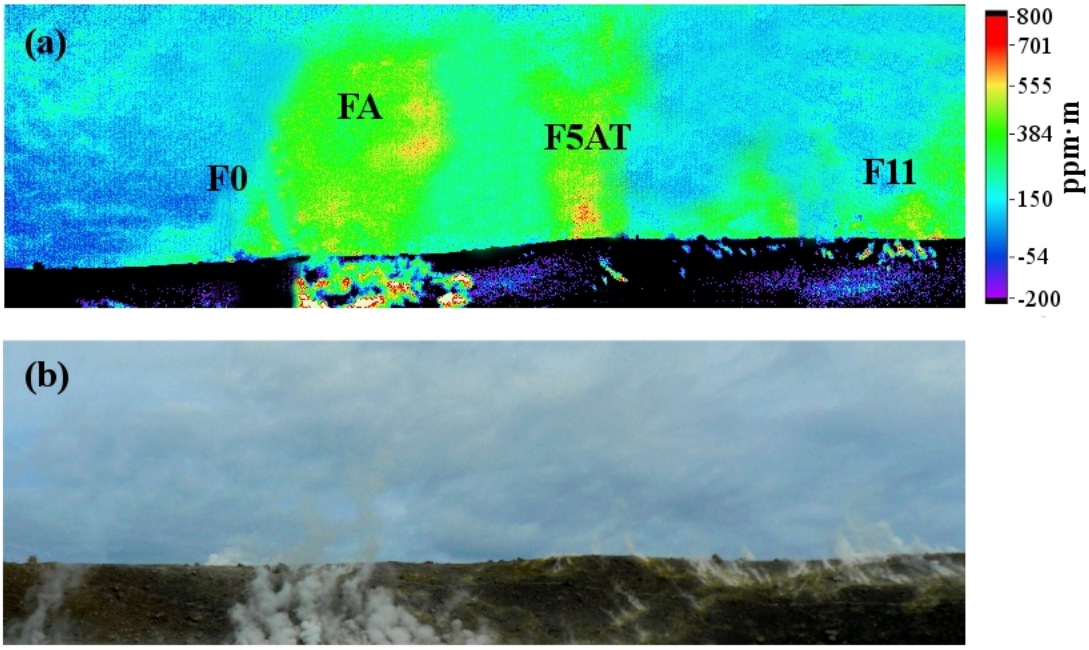

Figure 43: (a) UV SO_2 slant column density (ppm·m) image and (b) visible image of the fumarolic field.

The wind speed (measured with a hand-held anemometer) ranged from ~0 to 0.3 $m \cdot s^{-1}$ on November, and from 3.5 to 6 $m \cdot s^{-1}$ on February. The stronger wind on February partially hampered resolving between the different fumaroles (especially F0 and FA, Fig. 43a), whose atmospheric dispersions were somewhat overlapping. Of the 206 couples of images of the F0 + FA area taken on February, only 10 were affected by degassing of the F0 fumarole, while a mixed F0 + FA plume was captured in the remaining cases. In November, when the wind was instead blowing more gently, the

gas was rising vertically (Fig. 43, 44a), making the fumaroles more easily distinguishable.

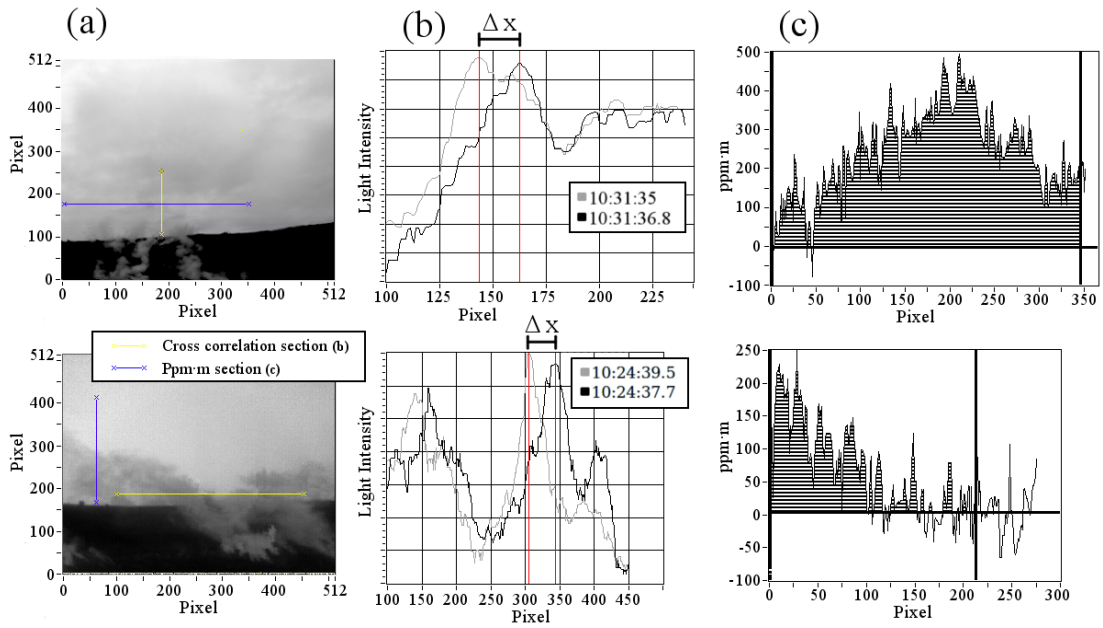

Figure 44: (a) UV image (310 nm filtered) of the F0+FA area in November (upper image) and February (bottom image). The 310 nm filtered image (in which SO_2 absorption occurs) was used for cross-correlation operation (and thus plume speed derivation), because it displays a larger pixel-to-pixel intensity variation than the ratio image. The yellow line shows the section of the image along which the cross-correlation is performed. (b) The plots show (for November and February survey from top to bottom) pixel-to-pixel intensity variations along the yellow sections taken in two consecutive 310 nm filtered images. From the pixel shift (ΔX) between the gray and black line (this taken along the same yellow section but after an interval ΔT of 1.8s), the mean speed in that interval was calculated. This ΔX was larger on February than in November (when the plume was more gently dispersed). (c) SO_2 slant column densities (in ppm·m) calculated along cross sections perpendicular to plume transport direction (blue lines in the 310 nm filtered image). The areas (shaded) below the SO_2 slant column density curves were integrated, with respect to distance across the plume, to derive integrated columns amounts (ICA). The thick black lines mark the integration boundaries.

During both surveys, we calculated SO_2 ICAs by integrating pixel concentrations along representative lines within the UV image perpendicularly oriented to the plume transport direction, and a few meters from the fumarole in question in order to minimize interference from adjacent sources (Fig. 44). The summation was performed horizontally for the November data, when wind speeds were low (0 to 0.3 $m \cdot s^{-1}$) so the plumes rose vertically; and vertically for the February data, when the wind blew from the south-east and rather more strongly (3.5 to 6 $m \cdot s^{-1}$) so that the gases propagated quasi-horizontally.

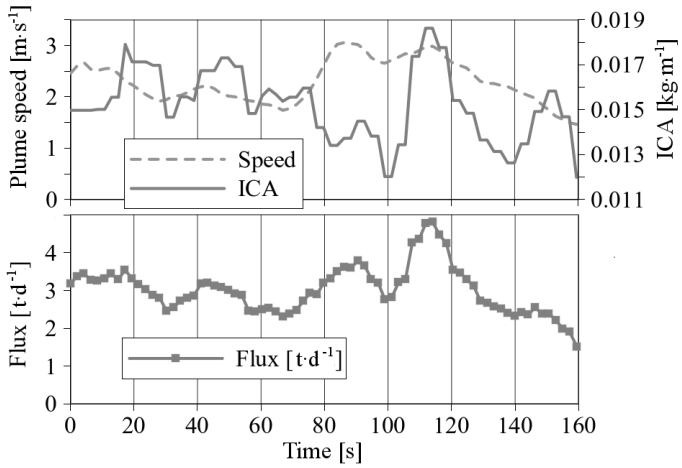

Figure 45: An example ICA record for the November survey (F0 fumarole). The SO_2 flux (in $t \cdot d^{-1}$) was obtained by multiplying the plume speed ($m \cdot s^{-1}$) by the Integrated Column Amount ($kg \cdot m^{-1}$).

An example ICA record for the November survey is given in Fig. 45, showing typical smooth fluctuations in gas emission over timescales of 10-20s. During the February survey, more irregular temporal ICA trends were observed: as the wind speed increased, the gas plume eventually grounded or went out of the field of view, precluding any retrieval (no ICA data were calculated in such high wind conditions). Plume transport speed was calculated by the in-plume cross-correlation method (Fig. 44b, 44c); this minimizes the error due to the plume speed uncertainty, especially if we derive the shift using multiple sections (the yellow line in Fig. 44a) in an image. The so-calculated plume speed ranged from ~2 $m \cdot s^{-1}$ (November) to ~6 $m \cdot s^{-1}$ (February). Finally, the SO_2 flux was calculated combining ICA and plume speed, as shown in Figure 45: this allows derivation, for each main vent of the fumarolic system and with high time-resolution, a record of subtle SO_2 flux variations.

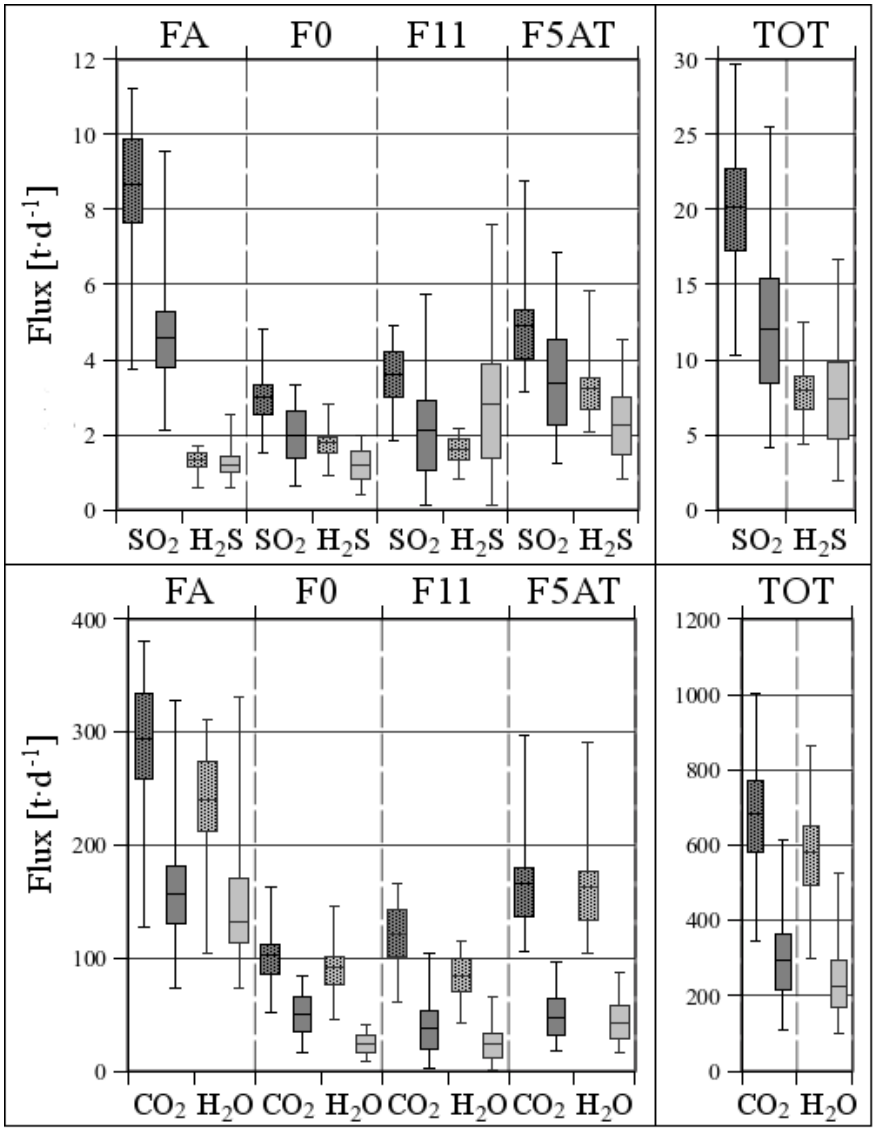

Figure 46: Box-plot showing SO_2, H_2S, CO_2 and H_2O fluxes from individual fumaroles and for the entire field in November 2009 (dotted box) and February 2010 (solid box). An overall decrease in gas fluxes between the two survey is evident.

SO_2 flux results are summarized in the box plot of Figure 46. This clearly highlights that, in both surveys, the FA fumarole was the main degassing area, accounting for ~50% of the bulk SO_2 degassing. The total SO_2 flux from the volcano, calculated by summing contributions from the 4 exhaling areas varied from ~ 21 $t \cdot d^{-1}$ in November (dotted box) to ~ 12 $t \cdot d^{-1}$ in February (filled box), a factor ~2 larger in the former case, during the degassing/heating event, than in the latter, when the fumaroles were cooling down (Istituto Nazionale di Geofisica e Vulcanologia, Sezione di Palermo, unpublished data, 2009). These results are qualitatively similar to those presented by Aiuppa et al. (2006a), who, whilst using a very different SO_2 flux

retrieval technique (walking traverses with a zenith-pointed UV spectrometer), derived SO_2 fluxes of 33 $t \cdot d^{-1}$ and 35 $t \cdot d^{-1}$ during the two unrests in the 2004 –2006 period, and factors of 2-3 lower fluxes (from 2 to 18 $t \cdot d^{-1}$) for the periods in between.

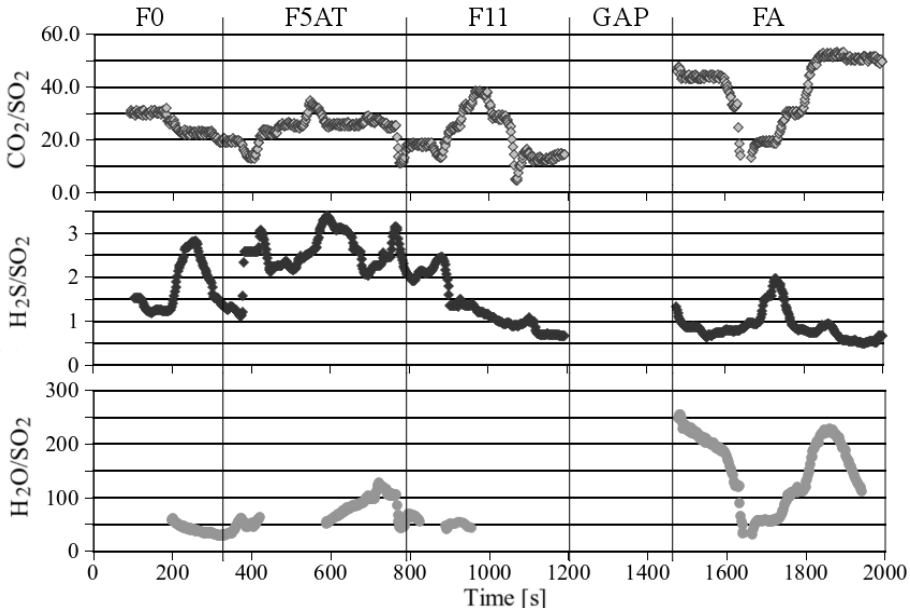

Figure 47: Variation of H_2S/SO_2, CO_2/SO_2 and H_2O/SO_2 molar ratios along the Multi-gas acquisition path (data for the February survey are shown in this example). X/SO_2 molar ratios were derived from best fit regression lines in X vs. SO_2 scatter plots (R^2 values were > 0.6). The central data gap is due to the absence of fumaroles between the F11 and the FA.

5.2.3.2 MULTI-GAS MEASUREMENTS

During each campaign, we also made MultiGAS traverses to derive the spatial distribution of plume H_2S/SO_2, CO_2/SO_2 and H_2O/SO_2 molar ratios over the fumarolic field (Fig. 47). In agreement with Aiuppa et al. (2005), we observed contrasting compositions for the four representative fumarolic areas (F0, F5AT, F11, FA). Figure 47 shows such results, illustrating that the H_2O/SO_2 and H_2S/SO_2 molar ratios varied mostly widely, ranging from ~ 30 to ~ 220, and from 0.6 to 3.4, respectively across the field. The FA fumarole, which is the hottest vent and typically displays the most magmatic chemical signature (Nuccio and Paonita, 2001), was characterized by lower H_2S/SO_2, and higher CO_2/SO_2 and H_2O/SO_2 molar ratios, than the rim fumaroles (e.g., F0), where hydrothermal gas contribution becomes more important, so H_2S prevails over SO_2 (as is typical of hydrothermally-buffered gases). As previously noted

(Aiuppa et al., 2005a), the F11 fumarole has H_2S/SO_2 and CO_2/SO_2 ratios intermediate between F0 and FA.

5.2.4 Discussion and conclusions

Since 1988, SO_2 flux measurements have been performed on La Fossa crater by traversing beneath the plume by boat, car, or by foot (Aiuppa et al., 2006a); or scanning the gas plume from a fixed position (Mcgonigle et al., 2005b). This has led to bulk SO_2 fluxes, with time resolutions, at best, of minutes to hours. Neither the traverse nor the scanning techniques were able, however, to resolve short-term fluctuations in SO_2 degassing rate (over time-scales less than minutes), or, more importantly in this case, to derive the relative contribution of the different fumaroles to the overall SO_2 flux. The latter limitation is particularly significant for the derivation of volcanic fluxes for other gas species, e.g., CO_2, or H_2O: the traditional approach of scaling the bulk volcano's SO_2 flux by the composition of a single emission vent, assumed to be representative of the whole field, is clearly inaccurate for relatively large and chemically heterogeneous fumarolic fields like La Fossa. In such circumstances, composition and flux data for each of the main degassing areas is necessary.

In this work we took advantage of the high spatial (0.3 meters per pixel) and time resolution (~ 0.5 Hz) of the UV camera (Kantzas et al., 2010) to propose a new approach for exploring multiple-source SO_2 gas emissions from fumarolic fields. The camera-derived individual fumarole SO_2 fluxes (Figs. 45, 46), when coupled with MultiGAS (Aiuppa et al., 2005) derived gas/SO_2 molar ratios for a number of fumaroles (Fig. 47), allowed us to accurately assess CO_2, H_2O, and H_2S fluxes (Fig. 46), and thus to refine previous gas inventories from the volcano (Aiuppa et al., 2005a; McGonigle et al., 2008).

Figure 46 shows that the major components H_2O and CO_2 are mainly contributed by the FA fumarole, and by the F5AT fumarole to a lesser extent. In contrast, the FA area only marginally contributes to the volcano's H_2S budget, which is instead dominated by the rim fumaroles (F11 and F5AT in particular).

Our results also clearly show that there was a factor ~2 increase in CO_2 degassing during la Fossa crater degassing/heating unrest (the derived CO_2 fluxes were 680 $t \cdot d^{-1}$ in November 2009, and 290 $t \cdot d^{-1}$ in February 2010; Fig. 46). Our mean CO_2 flux of ~ 490 $t \cdot d^{-1}$ (average of the two surveys) is between 2 and 6 times larger that the CO_2 flux diffusely degassed from soils in the Vulcano Porto area (Chiodini et al., 1996), highlighting that the central conduit system feeding the fumaroles is the main gas transfer path. We also evaluate a mean H_2O flux of ~ 400 $t \cdot d^{-1}$, close to earlier estimates by Italiano et al. (1998) and Chiodini et al. (2005). We additionally confirm that the H_2O flux is also larger during La Fossa heating events than in "cold" periods (580 $t \cdot d^{-1}$ in November 2009 and 225 $t \cdot d^{-1}$ in February 2010); supporting the idea that recurrent heating unrests on La Fossa fumarolic field reflect an enhanced rate of hot (deep rising) gas transport to the surface. In contrast, the total H_2S flux was apparently not affected by the heating event (8 $t \cdot d^{-1}$ in November 2009 and 7.5 $t \cdot d^{-1}$ in February 2010). Our mean H_2S flux of ~ 7.7 $t \cdot d^{-1}$ is consistent, or slightly higher, than previous estimates; from ~ 6 $t \cdot d^{-1}$ in 2003, Aiuppa et al., (2005b); to ~4 $t \cdot d^{-1}$ in 2004 (Aiuppa et al., 2005a). Since H_2S is a hydrothermally derived gas component, our observations suggest that a deep magmatic (CO_2-rich and H_2S-poor) reservoir was likely sourcing the anomalously high gas emissions in November 2009, and indeed during other degassing/heating events.

We conclude that systematic UV camera/MultiGAS monitoring of gas fluxes could improve our understanding of degassing processes, and contribute to volcanic hazard assessment. Indeed, our measuring technique was sensitive enough to detect the increase in gas fluxes during the La Fossa crater heating events.

5.3 Stromboli: insights on passive SO_2 gas emission, Strombolian eruptions, and puffing[2]

5.3.1 Introduction

Active volcanoes dissipate their magma-transported energy in a variety of ways, among which volcanic degassing is often dominant (Oppenheimer, 2003). *Passive* degassing is frequently the only visible surface expression of the activity of quiescent volcanoes, and also makes up a large fraction of the daily mass/energy release from persistent basaltic volcanoes (Shinohara, 2008). At such open-vent systems, this *passive* degassing frequently coexists with *non-passive* degassing forms, resulting from emission of over-pressurization gas jets/pockets in either bursts or puffs (Harris and Ripepe, 2007). Near-surface gas bursting is the fuel for mildly explosive activity at basaltic volcanoes (Parfitt, 2004), and whilst this is thought to represent only a small part of the total degassing budget of a volcano (Allard et al., 1994), it carries important information on explosion triggering mechanisms, and as such on the volcanic behaviour in general (e.g., Allard et al., 2004; Burton et al., 2007a).

Over the last few decades, remote sensing techniques working in the UV region of the electromagnetic spectrum have increasingly been applied to explore the long-term (years) to medium-term (days) trends in the rate of SO_2 release from active subaerial volcanoes (McGonigle and Oppenheimer, 2003; Oppenheimer et al., 2011; Tamburello et al., 2011a). From these observations, the *time-averaged* budgets of SO_2 release for a number of individual volcanoes have been obtained, and the global volcanic SO_2 flux has been evaluated with reasonable accuracy (Andres and Kasgnoc, 1998). In spite of this progress, however, the relative roles played by passive and non-passive degassing in determining the total volcano's gas budget remain largely unknown. This comes from the fact that non-passive degassing processes, such as gas release during Strombolian explosions or gas puffing, typically correspond to timescales of seconds, therefore cannot be resolved with traditional (scanning or traverse) techniques, which generally have temporal resolution of minutes to hours.

[2] Article under submission to Earth and Planetary Science Letters

The recent advent of the UV camera represents a step forward in volcanic gas remote sensing (Mori and Burton, 2006; Bluth et al., 2007), allowing SO_2 measurement to be carried out with unprecedented spatial and temporal resolution. This technique has rapidly found widespread usage in targeting previously unresolvable aspects of volcanic degassing, such as the SO_2 budgets of individual Strombolian (Mori et al., 2009; Dalton et al., 2009) and Vulcanian (Holland et al., 2011; Nadeau et al., 2011) explosions, and spatial analysis of heterogeneous gas sources such as fumarolic systems (Tamburello et al., 2011b).

Here, we use the dual-UV camera technique detailed in Kantzas et al., (2009) and Tamburello et al., (2011) to provide a comprehensive and simultaneous characterisation of the three main forms of SO_2 gas release from Stromboli volcano: passive degassing, explosive degassing, and puffing. Stromboli, in the Aeolian islands (Fig. 48), is the archetype for "strombolian" activity, an eruptive behaviour found on many other volcanoes (e.g. Shishaldin, Fuego, Villarica, Etna, Karymsky). At Stromboli, explosions are regularly super-imposed on the persistent quiescent degassing activity, with each event lasting a few seconds at most (mean duration, 15s; Patrick et al., 2007), with ~300 explosions/day (Ripepe et al., 2008). Syn-explosive gas emissions therefore have a cumulative daily duration of only ~ 80 min, which led Allard et al. (1994) to suggest their contribution to the total daily SO_2 budget (250±50 $t \cdot d^{-1}$; Allard et al., 2008) is relatively low. The few previous measurements (a total of only ~ 30 explosions have been characterised to date, using air-borne COSPEC observations - Allard et al., 1994 - single UV camera acquisitions - Mori et al., 2009 - and the two spectrometer technique - McGonigle et al., 2009), also tentatively indicate that explosions may correspond to only 3-8 % of the total SO_2 flux (Allard et al., 1994; Mori et al., 2009). In addition to explosions, Stromboli is also the site of persistent and repetitive (every 1-2 s) release of small overpressurised gas pockets during *puffing* (Harris and Ripepe, 2007). While no direct measurements of the gas flux contributed by puffing has been reported to date, there are thermal and infrasonic data, which have been used to argue that puffing may be responsible for up to ~100 t/d

SO_2 (or 50% of the total degassing budget) (Harris and Ripepe, 2007; Ripepe et al., 2008).

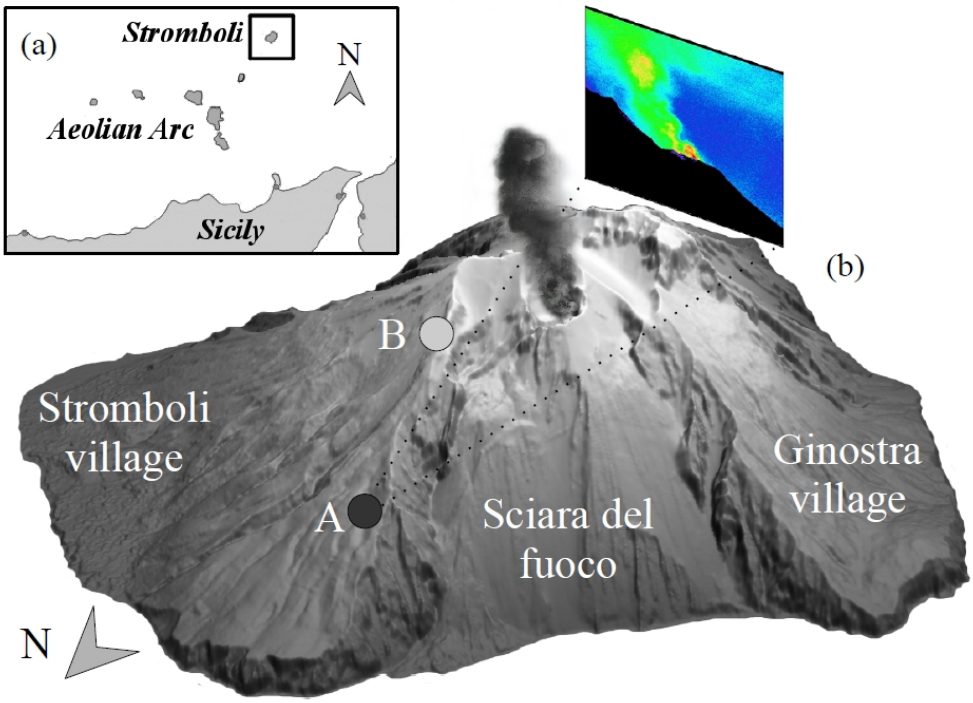

Figure 48: (a) Location of Stromboli with respect to mainland (b) Digital elevation model of Stromboli (courtesy M. Marsella), showing location of measurement sites: A, SAR observation site (dark grey circle); B, Roccette site (light gray circle). An exemplificative graphical representation of the UV camera field of view from site A is given by the pseudo-colour image (in yellow, the SO_2-rich gas plume).

The aim of this work is to contribute to a better understanding of the mechanisms and timing of SO_2 release from Stromboli, with special emphasis on strombolian explosions and puffing. These results provide wider implications for degassing activity at other open-vent basaltic volcanoes.

5.3.2 Hardware and technique

We report here on results of an UV camera survey carried out on Stromboli from the 10th to the 16th of July 2010. Additional data collected on the 20th May 2011 are also included. Overall, we recorded ~16h of image sequences, and observed ~130 explosions throughout. Most measurements were carried out from the SAR site, on the northern rim of the Sciara del Fuoco (Fig. 48), ~ 1 km from the volcano's summit. Considering the close proximity of this site, any error or artefact related to distance from the target (Bluth et al., 2007; Kern et al., 2009) had likely only a very minimal impact on our measurements.

In order to derive accurate and high-frequency (~1Hz) SO_2 flux time series with the UV cameras, we first considered a cross section (first cross section in Fig. 49a) a few meters above the vents, for which we obtained SO_2 concentration profiles, over the pixels, similar to that shown in Figure 49b, and, by integration, the ICA. Then, in order to calculate the plume transport speed, we calculated ICA time series for two parallel cross sections of the plume in the SO_2 column amount image (Fig. 49a) as discussed in the *section* 4.1.5. A mean plume speed has been calculated using cross correlation of these two ICA time series, for every episode of passing degassing, occurring between explosions. The explosions themselves are too fast however, to allow a measurable delay ΔT, therefore a velocity profile has been calculated manually by visually observing the progression of the eruption cloud across the field of view, in an image sequence. This process is expedited by the marked contrast between the high SO_2 concentration in the explosive gas plume against the far weaker quiescent plume.

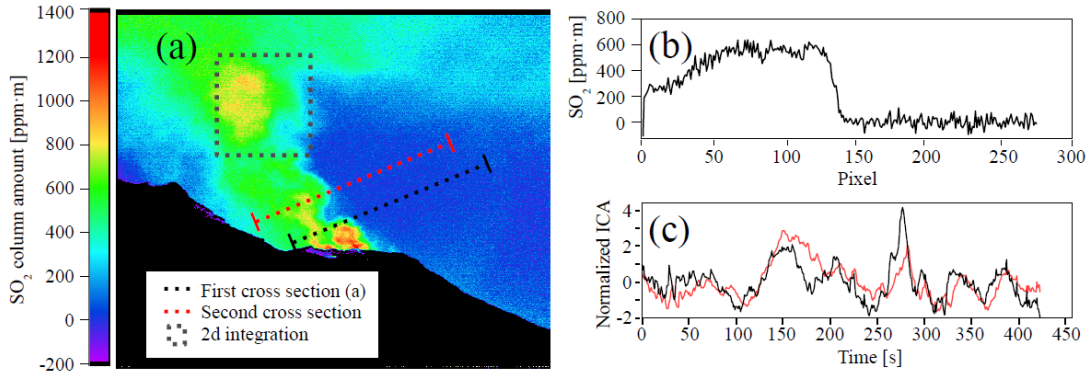

Figure 49: (a) SO_2 column amount image obtained from SAR observation site. The black and red dotted lines represent the two sections taken for SO_2 flux and plume speed calculation (see text), the gray dotted square shows an example of an integration area over which the total (cumulative) SO_2 amount (in kilograms) is calculated (cfr. 4.1.6); (b) Pixel-to-pixel variation of SO_2 column amounts along a cross section of the plume (black dotted line in (a)). SO_2 is integrated along the profile top obtain the integrated column amount (ICA), then multiplied by the plume speed to derive SO_2 flux (c) Normalized ICA time series from the two cross sections of the pseudo-colour graph (black and red dotted line), showing a typical time delay ΔT between the two series: the plume speed is calculated from ΔT the by knowing the distance ΔX between the two sections.

UV cameras also provide knowledge of the concentration distribution along two dimensions $C(x,y)$; by integrating a second time along the dimension perpendicular that that of the integrated column amount, one can calculate the integrated volume amount (IVA), e.g., the cumulative amount of SO_2 within a imaginary prism of infinite thickness (see gray dotted square in Fig. 49a):

$$(14)\ IVA[kg] = \int_{x_i}^{x_f} \int_{y_i}^{y_f} C \cdot dxdy$$

This calculation does not require knowledge of the plume speed, thus overcomes the inherent difficulties in measuring the ascent rate of the explosion gas thrust (see above). This technique has been used here to calculate the SO_2 mass contributed by individual explosive bursts (results in section 5.3.3.2), and by individual puffs (section 5.3.3.3). The integration window ranged between 160×220 pixels for the explosions to 30×30 pixels for puffs. The former was more or less constant for most events, although slightly bigger windows were required for the largest explosions; in the latter case this pixel range was always used as puff volumes are rather constant.

Some strombolian explosions erupt finer particles which are coupled with the gas phase, creating an ash-rich plume. Ash represents an obstacle to accurate measurement of the erupted SO_2 mass, because it prevents sun light from passing through the plume causing absorption and back reflection at the surface of the cloud (Kern et al., 2009). Ash settles down rapidly from the eruptive plume, however, making it more and more transparent during ascent and dispersion in the atmosphere. A good proxy for the transparency of the explosive plume is the ratio between the mean light intensity recorded by the 330 nm filtered camera inside the cloud ($I_{e,330}$), and the light intensity of the background ($I_{b,330}$ clear sky), the so called ash index (AI), assuming that ash is the main absorbing species:

$$AI = \frac{I_{e,330}}{I_{b,330}} \quad (15)$$

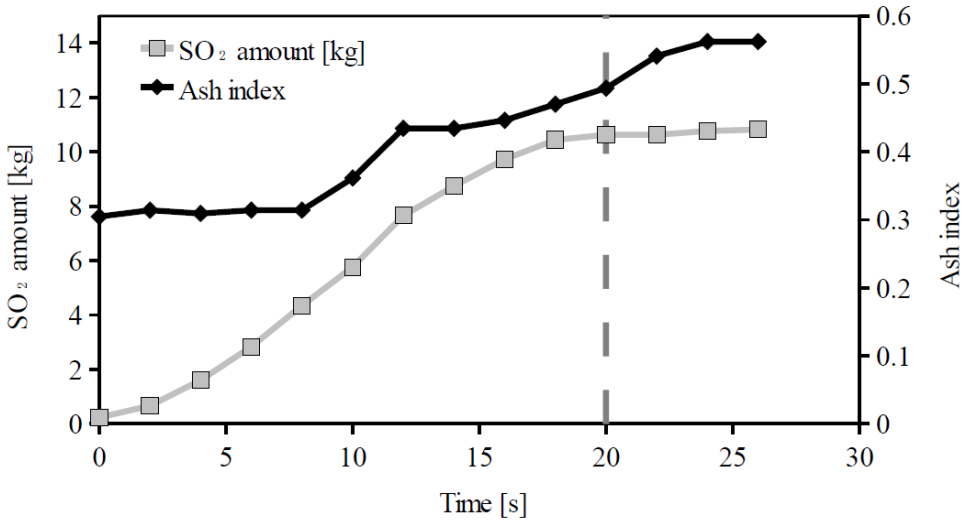

Figure 50: Time variation of SO_2 amount (in kg) and ash index during an ash-rich explosion (time 0 - the explosion onset - is fixed from the first appearance of a thermal signal in the radiometer). The figure shows that a steady SO_2 value is achieved for AI ≥ 0.5 (after ~20 seconds from the explosion onset).

Theoretically, in the absence of ash, the index should result ~1; in the real world, however, the plume contains water vapour and aerosols that absorb a priori in the range of wavelengths, so that the AI ranges between 0.5 and 0.8, even for ash-free explosions. Figure 50 shows the typical time-evolution of AI and SO_2 amount, during an ash-rich explosion (these occurred mostly at the NE crater): as the AI increases due

to ash deposition and settling from the plume, the erupted SO_2 mass also increases to achieve a steady value for $AI \geq 0.5$. We therefore assume our SO_2 measurements to be only marginally affected by ash above this threshold. We stress this procedure would not be possible using a single 310 nm filter, where the absorption of ash and SO_2 would be indistinguishable, entirely precluding the possibility of accurate retrieval (e.g., Kern et al., 2009).

5.3.3 Results

From 10th to 15th of July, we deployed the UV cameras on the lower north rim of the Sciara del Fuoco on Stromboli at the SAR location, about 350 m asl (Fig. 48). The site is ~ 1 km from the crater terrace (~ 750 m asl), and ensured a clear view of the explosions as shown in Figures 48 and 49. Additional measurements were taken (on July 16th 2010 and May 20th 2011) at the more proximal site ROC (Fig. 48), from which a clear view of puffing degassing from the central crater was occasionally possible. During the whole campaign, the plume remained transparent (with very little condensation), and rose quasi-vertically under relatively windless conditions; convection was the main motion mechanism of the rising gas (plume loft speed ~ 3 $m \cdot s^{-1}$).

5.3.3.1 Total SO_2 flux

The two PC-synchronised cameras captured (at ~0.8 Hz rate) sequential images of the bulk (total) craters' plume (Fig. 49a), from which we derived high time-resolution time series of the SO_2 flux, an example of which is given in Figure 51. For each acquisition day, we averaged the large number of SO_2 flux measurements taken to obtain robust evaluations of total SO_2 flux emissions, as summarised in Table 1. According to our data, Stromboli's time average SO_2 passive release ranged from 0.4 to 1.9 $kg \cdot s^{-1}$ during the observation period, thus being somewhat lower than the volcano's longer term time-averaged SO_2 flux emissions of 3 $kg \cdot s^{-1}$ (Allard et al., 2008). This reduced SO_2 degassing in mid-July 2010 is in accord with the low to

moderate level of volcanic activity and seismicity after the 25-30 June 2010 major explosions (Aiuppa et al., 2011). In addition, our camera-derived time-averaged SO_2 fluxes (Table 1) are consistent with results simultaneously obtained by the permanent network of UV scanning spectrometers operated by INGV-Catania (for the 3h measurement shown in Figure 51, we obtained a mean SO_2 flux of 0.78 $kg \cdot s^{-1}$, which corresponds well with the 0.8 $kg \cdot s^{-1}$ daily average obtained on the same day by the scanning network).

Date	UV camera	Note
10 July 2010	0.6 ± 0.15 $kg \cdot s^{-1}$	From SAR
11 July 2010	0.81 ± 0.17 $kg \cdot s^{-1}$	From SAR
12 July 2010	max 0.6 $kg \cdot s^{-1}$	From SAR, hidden gas behind craters
13 July 2010	max 0.7 $kg \cdot s^{-1}$	From SAR, hidden gas behind craters
16 July 2010	1.9 ± 0.3 $kg \cdot s^{-1}$	From Roccette

Table 1: Daily average of the total SO_2 flux of Stromboli during our observation period.

The results shown in Figure 51 also demonstrate that, when observed at a ~1 Hz sampling rate, SO_2 flux time series have a dynamic and complex structure which is unresolvable by conventional UV scanning techniques. We identify two novel features in our dataset: (i) impulsive and large (up to ~1.6 $kg \cdot s^{-1}$) SO_2 flux variations (Fig. 51a), and (ii) longer and milder (duration of hundreds of seconds; amplitude, 0.1-0.3 $kg \cdot s^{-1}$) cyclic fluctuations in emission (Fig. 51b). We therefore conclude that the SO_2 output from Stromboli systematically varies over timescales of seconds/minutes, with both impulsive and semi-cyclic behaviour.

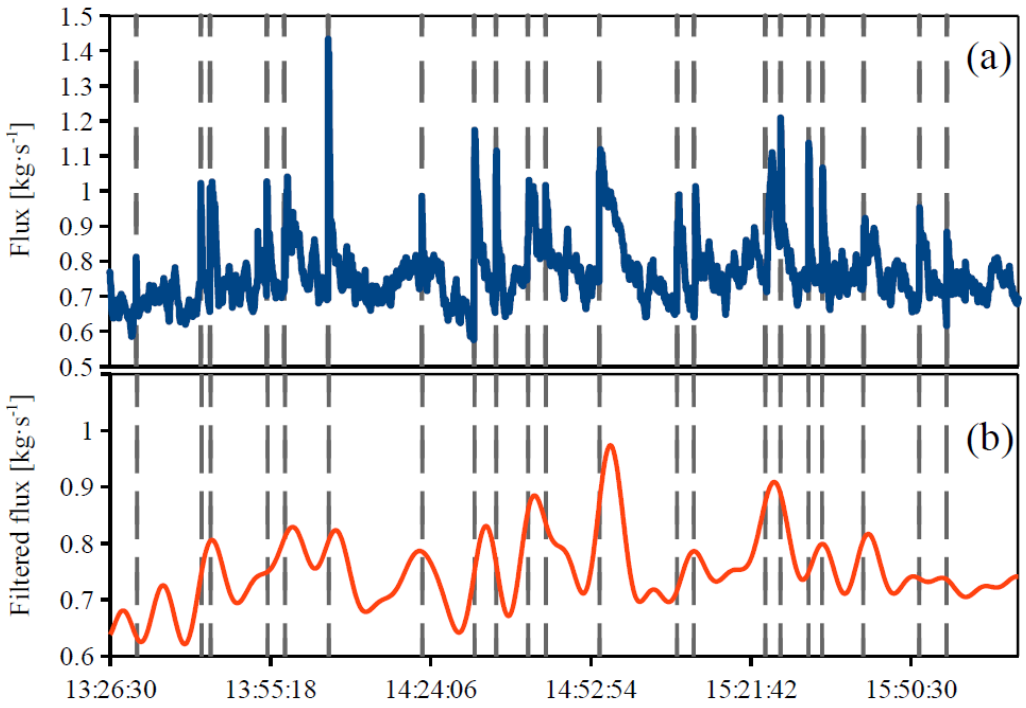

Figure 51: (a) Two-hours high frequency (0.8 Hz) record of the total SO_2 flux from Stromboli from site A, taken on July 13th, 2010. Each explosion (vertical dotted line) is associated with a large SO_2 flux increase, followed by a few-minute long coda. This, combined with the rhythmicity of Strombolian explosions, originates a "periodic" SO_2 degassing behaviour (period, ~ 300-700s), clearly visible in the 0.004 Hz low-pass filtered SO_2 time series of (b).

The impulsive SO_2 flux signals (duration, 15-30s) are clearly sourced by explosive gas release during individual Strombolian events (Figs. 51 and 52). Each explosion is captured by our UV images (see sequence of frames (a) to (e) in Fig. 52, and video V1 in the auxiliary materials) as a fast-rising SO_2 cloud, whose initial release time is nearly simultaneous with onset of the thermal signal (as captured by radiometers) radiated by hot pyroclastic materials upon their ejection from the eruptive vent(s) (Fig. 52f). This gas signal onset also falls in the centre of the very-long-period seismic displacement (Chouet et al., 2003) typically associated at Stromboli with explosions (Fig. 52f).

Our results also show that each explosion is systematically followed by a few minute-long coda (Fig. 52f), during which the SO_2 flux exponentially decreases to the pre-explosion value. This, combined with the intrinsically rhythmic nature of Strombolian explosions, gives rise to a manifestly periodic SO_2 outgassing behaviour (Fig. 51b), with cycles of SO_2 flux increasing and decreasing lasting hundreds

(typically, 300-700s) of seconds. We therefore conclude that strombolian explosions modulate the volcano's degassing behaviour over timescales (minutes) much longer that the explosion' duration itself.

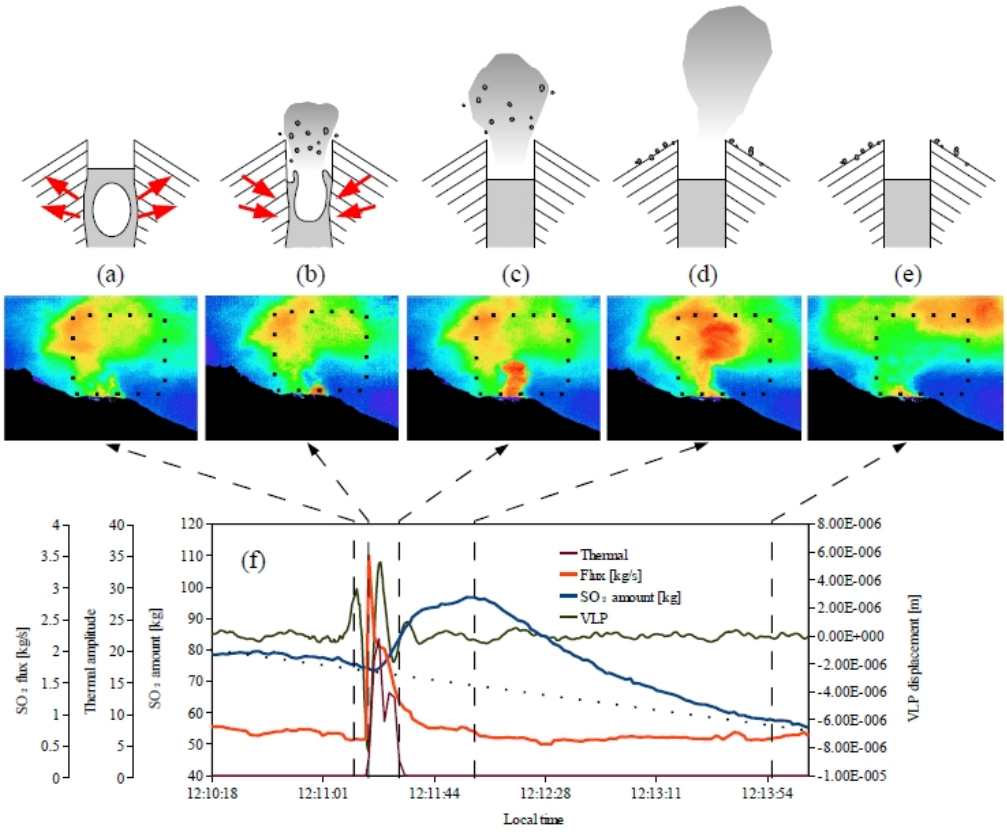

Figure 52: (a-e) SO_2 column amount image sequence (pseudo-colour graphs) taken prior to (a), during (b-d), and after (e) a Strombolian explosion, and schematic illustration of the related conduit processes involved (sketches on the top). In the sketches, the conduit inflates prior to the explosion as the slug is generated and ascends, and then deflates as the gas is suddenly erupted during the explosion; (f) Inter-comparison between SO_2 flux, SO_2 amount, VLP displacements and thermal amplitude, all simultaneously recorded before, during and after the explosion (which onset time is taken as frame (b)). Thermal and SO_2 flux signals are nearly synchronous, while the SO_2 flux trend is centred on the negative gradient middle portion of the VLP signal. The SO_2 amount curve (blue line in (f)) is obtained by applying the two dimension integration technique (section 2.3) to the area delimited by the dotted box of frames (a) to (e). The SO_2 mass (in kg) released by the explosion is calculated by subtracting the background (black dotted line in (f)) from the maximum (frame d) of the SO_2 amount curve (blue line).

5.3.3.2 SO_2 release during Strombolian explosions

The SO_2 signal related to Strombolian explosions is clearly visible in our SO_2 flux record (Fig. 51). At least in principle therefore, integration of the area below the "explosive" SO_2 flux curve (in red in Fig. 52f) might straightforwardly be used to calculate the SO_2 mass released during individual explosions. This operation is however complicated by two classes of problems: (a) our SO_2 flux measurements are taken, looking only a few meters above the vent, where the effect of ash on the measured signal (see Fig. 50) is likely significant (at least for the ash-rich explosions); (b) the gas thrust at the base of the eruptive column is of high and rapidly-changing ascent speed (see below), implicitly reducing the accuracy in SO_2 flux measurements.

We therefore used the two dimension integration technique (section 4.1.6) to obtain more reliable estimates. Figure 52 shows an example of the technique used: for sets of consecutive images, we performed pixel-to-pixel two-dimensional integration of SO_2 concentrations within the dotted area above the vents (Fig. 52a), and obtained the variation of total SO_2 mass (in kg) in that area (given by the blue curve in Fig. 52b). This showed a smooth but systematic increasing/decreasing cycle after each explosion, the peak in SO_2 mass being typically reached 70±30 seconds after the blast. By subtracting the SO_2 contribution observed prior to and following the explosion (see dotted line below blue curve in Fig. 52f) to the corresponding observed maximum value (Fig. 52d), we obtained the total SO_2 mass released during each strombolian explosion. This background subtraction procedure wasn't required on days with stronger wind, where the passive and explosive plumes were clearly spatially segregated, the former being grounded in the direction of the Sciara del Fuoco. Most of the explosions we measured were ash-free, leading to low overall error (± 15 %) in the mass measurements; only the NE crater produced explosions with ash, requiring use of the procedure detailed earlier (section 5.3.2).

Looking at the camera image sequences, the explosions were evident in clouds of highly concentrated SO_2 rising rapidly upwards (Figure 52). The initial velocity of

the gas explosion peaked at ~ 23 $m \cdot s^{-1}$, in agreement with Harris and Ripepe (2007); the gas jet initially rose very rapidly for the first 10-20 seconds, reaching heights of 40-140 m, then decelerated to a constant velocity as the motion became convective. The lowest rise speeds resulted from slow gas emissions (low energy explosion) dominated by convection.

During our campaign, we observed 147 discrete explosions overall, 29 from the NE crater and 118 from the SW crater (the latter were all ash-free). Explosions varied widely in style and appearance, but can be broadly categorized based on their rising gas speed, the geometry and evolution of the plume front. Following Patrick et al. (2007), we recognize two main groups: Type 1 (ballistic-dominated) and Type 2 (ash-dominated). Type 2 can be subdivided into two subgroups (Patrick et al., 2007): Type 2a explosions, which exhibit a visible gas thrust phase, and Type 2b, which only show convective velocities. As for the Type 1 explosions of Patrick et al. (2007), the UV cameras only allowed identification of their gas phase fraction, because bombs and lapilli are far too small to be resolved (at least from SAR) in our camera pixels. Observing only the gas phase, we found that Type 1 explosions can also be subdivided into two subgroups (1a and 1b), with the same velocity profiles of Type 2a (gas thrust) and 2b (convection), but without ash. Most of the observed explosions belonged to 1a and 1b Types, respectively 43 % and 41 %, whilst Type 2a and 2b subgroups accounted for 19 % and 5 %, respectively.

We found that the erupted SO_2 mass per explosion ranged 2-55 kg, with an average of ~20 kg for the 10^{th} to 15^{th} July period. The mean explosive frequency was 9.4±1.8 events per hour during our observations. From this, we estimate that the daily explosive SO_2 mass output rate was 0.05 ± 0.01 $kg \cdot s^{-1}$. We conclude that, at Stromboli, the explosive SO_2 gas output accounts for 7±1.5 % of the total SO_2 flux of ~ 0.7 $kg \cdot s^{-1}$ (average of 10^{th}-15^{th} July total SO_2 flux observations; see Table 1) .

5.3.3.3 SO_2 RELEASE FROM PUFFING

Gas puffs are rapid and repeated emissions of discrete packets of high-temperature gas from the vents (Harris and Ripepe, 2007). At Stromboli, puffing activity is systematically centred at only one vent per time (most often in the central craters' terrace area), thought switching from one vent to another is often observed by the infrasonic network (Ripepe et al., 2002). A single puff usually forms a convecting cloud of gas that ascends from the vent. After a few 10 s of meters, the puff cools, decelerates, expands and begins to mingle within the surrounding plume, issuing from the adjacent (quiescent or erupting) vents; therefore its individual character is lost rapidly (Harris and Ripepe, 2007).

In order to measure the SO_2 content of puffs produced by the central crater, we performed two campaigns: on 16 July 2010 and 21 May 2011 and placed the dual-camera UV imaging system on the Roccette (ROC; Fig. 48) site, about ~750 m asl and at a horizontal distance from the crater terrace of ~450 m.

During the first campaign, the infrasonic network run by Università di Firenze recorded very small pressure (< 2 Pa) transients, indicating that puffing activity was rather weak. Detection of gas puffs by UV imaging was challenging, therefore, and only 11 puffs were identified and measured within an hour. Figure 53a-d are sequence of UV images, showing a typical gas puff entering the integration box (red dashed area) in (b), covering the largest part of the box in (c), and then disappearing to become diluted in the main plume (d). The resulting time variation of the cumulative SO_2 mass in the box is given in (e), the maximum value in (c) [after subtraction of the baseline; red line in (e)] yield SO_2 mass for an individual puff. The derived SO_2 masses for single puffs ranged 0.14-0.45 kg, averaging at 0.28 kg. On the basis that puffing occurs at an average frequency of 1.7 s (Harris and Ripepe, 2007), its contribution to the daily SO_2 flux would thus be evaluated at ~ 0.16 $kg \cdot s^{-1}$. This would correspond to ~8 % of the total SO_2 flux produced by Stromboli on the same July 19th (1.9 $kg \cdot s^{-1}$; Table 1).

Because a relatively limited number of puffs were measured in 2010, therefore limiting the statistical significance of the acquired data, an additional campaign was carried out on 20th May 2011. During this second campaign, more sustained puffing activity was observed on the volcano by infrasound (> 3 Pa), and ~50 SO_2 puffs was measured in a single hour of observations. Figure 53e shows a sequence of two gas puffs (dotted boxes) issuing from the central crater, and clearly distinguishable from the main plume from from the SW crater (on the left in the image). With a sampling frequency of 1.2 Hz, it was possible to follow each puff, from emission at the vent up to heights of 10-30 m above the craters, but only when turbulent effects were at a minimum and the plume rose vertically with a buoyant ascent. Using thermal imagery, puffs are not longer distinguishable after ~ 15 m from source, when they have cooled to background plume temperature.

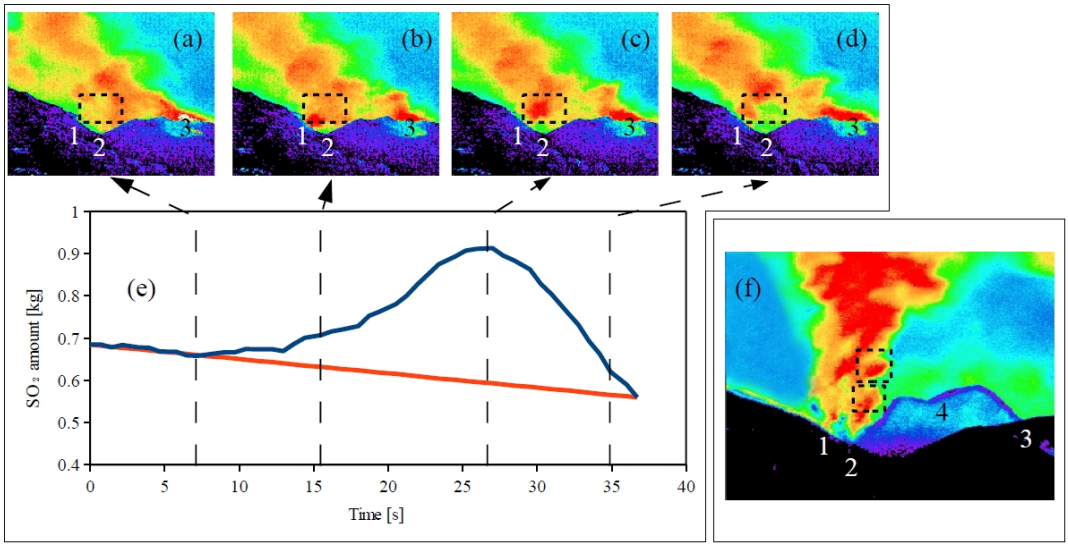

Figure 53: (a-d) SO_2 column amount image sequence of puffing from central crater, observed on July 16th 2010. The corresponding time variation of the integrated SO_2 amount, calculated applying the two dimension integration technique (section 4.1.6) to the area delimited by the dashed black box, is given in (e). The total SO_2 mass released by the puff is calculated by subtracting the background (orange line) to the maximum value of the SO_2 amount curve (blue line). (f) A sequence of two puffs observed on May 20th 2011, easily distinguishable from the adjacent plumes. Craters and respective plumes are clearly visible: south-west (1), central (2), north-east (3) and an hornito (4, growing from November 2010).

The so-measured single-puff SO_2 mass (20th May 2011 campaign) ranged 0.03-0.22 kg averaging 0.09 kg (Fig. 54). This, for a mean puffing rate of 1.7 s, would correspond to a daily SO_2 flux sourced by puffing of ~ 0.05 $kg \cdot s^{-1}$, or a factor ~3 less

than in July 2010 (this would be consistent with the fact that only the most-sizeable puffs were visible - and therefore measurable - by our UV observations in 2010). Considering a total SO_2 flux on 20th May 2011 of 1.7 $kg \cdot s^{-1}$, this intimates a relatively marginal (~3%) contribution from puffing to the total degassing activity.

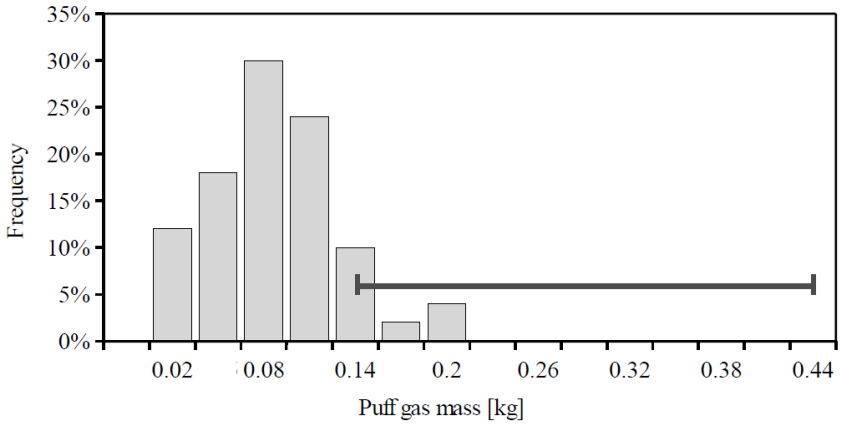

Figure 54: Histogram showing the frequency distribution of SO_2 mass released by individual gas puffs on May 20th 2011. The mode is centred at ~0.08 kg. The dark gray line shows the range of SO_2 puff masses measured on July 16th 2010.

In spite of the limitations of our measurements, and while more data are required to corroborate our conclusions, our results are strongly suggestive that the puffing contribution to the volcano's degassing budget is far lower than previously thought (Harris and Ripepe, 2007; Ripepe et al., 2008), and most likely <10 % of the total SO_2 flux.

5.3.4 Discussion

The results presented here clearly demonstrate the potential of the UV camera in characterizing –in nearly real-time – the different forms of gas release from an active volcano. Our observations, summarized in the cartoon of Figure 55, clearly corroborate the earlier hypothesis (Allard et al., 1994, 2008) of a dominant role played by quiescent degassing at Stromboli (and, likely, at other open-vent volcanoes), with non-passive degassing contributing to <15-20% to the total SO_2 degassing budget.

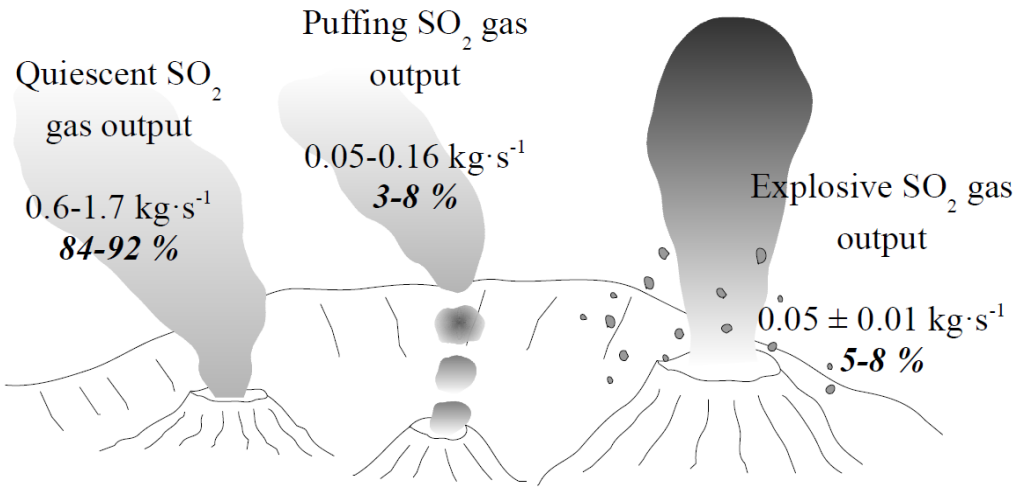

Figure 55: Sketch diagram summarising the relative contribution of passive and non-passive degassing (puffing and Strombolian explosions) forms to the total SO_2 budget (see text).

Our measurements also open the way to in-depth exploration of significant aspects of magmatic degassing at Stromboli, as discussed below.

5.3.4.1 Insights into explosive degassing

Our observations contribute to extend the currently limited data-set for explosive SO_2 emissions at Stromboli. Overall, our SO_2 mass estimates (2-55 kg, mean ~20 kg) for 147 individual strombolian events are in fair agreement with previous UV-based evaluations, yet based on observation of 5 (Mori and Burton, 2009) to 16 (McGonigle et al., 2009) explosions only. Accepting the assertion of Burton et al. (2007a) that SO_2 represents ~4.2 wt% of the syn-explosive strombolian gas phase, we therefore calculate the total gas mass released during explosions to range 50-1310 kg. In Figure 56, we compare this new estimate with previous evaluations based on a variety of techniques, including photoballistic (Chouet et al., 1974), infrasonic (Vergniolle and Brandeis, 1996; Ripepe and Marchetti, 2002) and seismic (Chouet et al., 2003). Hence, the gas-based direct observations (including this study) indicate that indirect (geophysical) techniques may potentially under-estimate (photoballistic, infrasonic) or over-estimate the real explosive gas emissions.

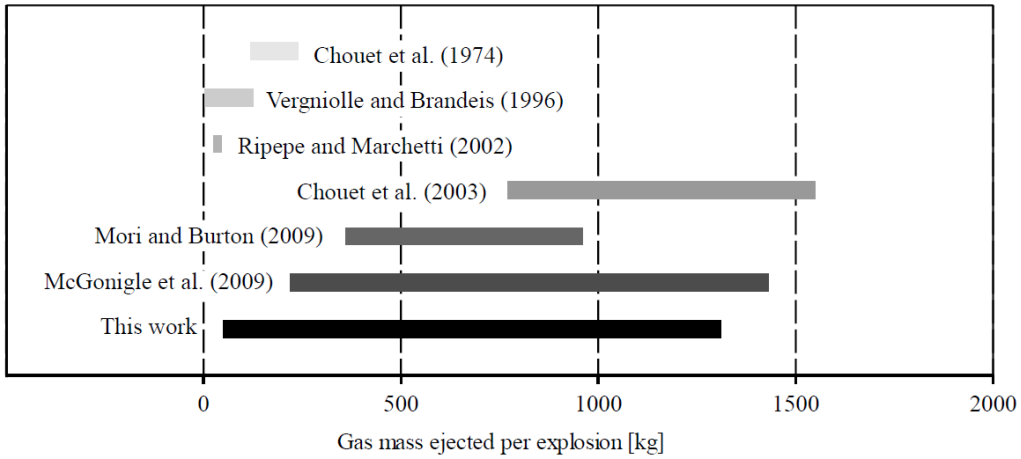

Figure 56: Total gas mass released by individual Strombolian explosions, from this work, compared with previous evaluations (see text for discussion).

Our UV camera observations also offer more in-depth exploration of the dynamics of gas release during Strombolian explosions. This is achieved here by integrating our UV camera-based SO_2 gas signals with simultaneous seismic and thermal observations taken by the multi-parametric geophysical network operated by the Università di Firenze (Ripepe et al., 2009) (Figs. 52, 57 and 58). This extends previous analysis done by McGonigle et al., (2009), and aims (among other objectives) to derive constraints on the source processes determining the large range (2-55 kg) of SO_2 explosive mass observed.

Figure 52f shows this gas-geophysical comparison for the explosive event imaged by the sequence of frames in Figure 52a-e. Two sets of information emerge clearly from the figure.

First, Figure 52 shows that the explosion onset - as given by the onset of the thermal signal captured by the radiometer - corresponds well to the first UV image in which the explosion is clearly visible (frame b in Figure 52). This suggests no substantial delay between emission of gas (SO_2 signal) and hot pyroclasts (which source the majority of the irradiated thermal signal; Ripepe et al. 2002) during the strombolian explosions; or, that the delay is shorter than the temporal resolution offered by the UV camera (1.2s).

Secondly, we observe that the gas signal typically lags behind (typically by ~10 seconds) the onset of the very long period seismic displacement (VLP seismic signal), which is systematically associated with explosions at Stromboli (Ripepe et al., 2001; Chouet et al., 2003). According to prevailing theory, the regularly observed VLP waveforms at Stromboli reflect a repetitive, non-destructive process at the source, which is typically attributed to a characteristic sequence of inflation–deflation–inflation of the source volume (Chouet et al., 2003). The initial inflation (first positive displacement in the black line of Fig. 52f) is thought to represent pressurization of the conduit upon formation and release of a gas slug, followed by a stronger conduit deflation (negative displacement in the black line of Fig. 52f) possibly due to lowering of the magmastatic head associated with the rise and ejection of the slug (Chouet et al., 2003). The final inflation stage would mark a re-pressurization of the conduit as the top of the magma column reforms after the slug has burst at the surface during an explosion. While our gas observations are not specifically designed to characterise VLP source processes, we note that - in virtually all the explosions we observed - the SO_2 signal onset was centred on the negative gradient, central section of the VLP signal (see Fig. 52f). This would imply that conduit deflation is a syn-eruptive feature, and may thus be thought to reflect top-of-the-conduit volume loss upon release of the gas-pyroclast mixture (frame c in Figure 52), rather than a within-conduit downward flow of magma around the rising gas slug (Chouet et al., 2003). Subsequent ground oscillations, lasting ~ 20 s and representing the system returning to equilibrium, are associated with a post-explosive exponential SO_2 flux decrease to pre-explosive values.

The proposal that gas ascent/bursting within/at the top of the conduit is the driving force for volumetric change leading to VLP seismicity is supported further by Figure 57, where a positive correlation between our syn-explosive SO_2 mass and the corresponding VLP displacement is observed (the VLP signal is here calculated as the total displacement observed between the inflation maximum and the deflation minimum), thus corroborating the previous result of McGonigle et al., (2009). A similar correlation has more recently been proven to exist at Asama volcano, where

the volume of individual gas bursts has been shown to scale with the corresponding VLP moment release (Kazahaya et al., 2011).

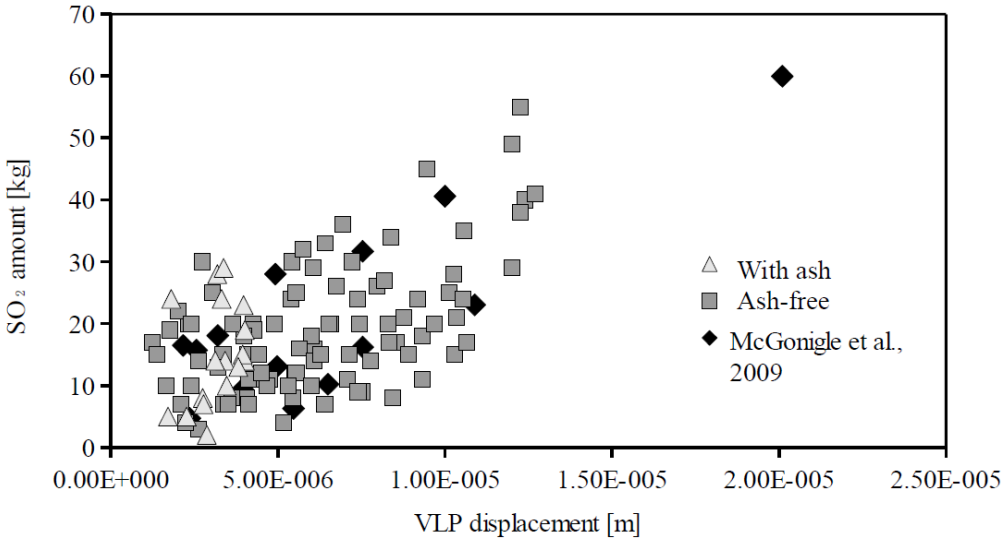

Figure 57: Scatter diagram of VLP displacement for individual Strombolian explosions, plotted versus the corresponding sin-explosive SO_2 mass.

In addition to this, we also notice that the syn-explosive SO_2 mass correlates fairly well with the amplitude of the radiometer thermal signal (Fig. 58). The latter represents the total irradiance from materials released during the explosion, including gas, ash, bombs, and lapilli, with the contribution of each component to the irradiance being dependent on its specific emissivity and emitting surface area. As volcanic ash has high emissivity (relative to gas), and spreads over a wider surface area of the radiometer's field of view (at least relative to rapidly deposited bombs and lapilli), it is not surprising that two distinct data trends emerge for ash-free and ash-rich explosions, respectively (Fig. 58). Ash-free and ash-rich explosions also appear to have different gas VLP behaviours (Fig. 57), the former being typically characterised by less variable, and generally lower, SO_2 masses (<30 kg) and VLP amplitudes ($<4 \cdot 10^{-6}$ m). The precise mechanisms for this are not entirely clear at this stage and should be a target of future study.

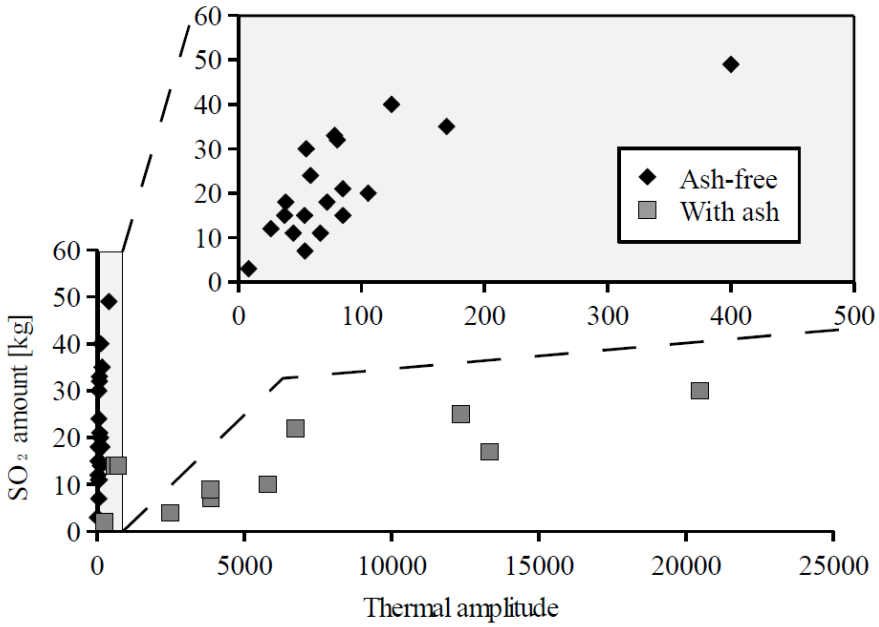

Figure 58: Scatter diagram of thermal amplitude for individual Strombolian explosions, plotted versus the corresponding sin-explosive SO_2 mass. The exploded gray-filled graph is a zoom on ash-free explosions.

To conclude, the data shown in Figure 52, 57 and 58 convey the straightforward (but hitherto only hypothetical) message that the larger the volume of gas coalescing and ascending within the conduit, the larger the resultant volumetric change in the conduit with be (e.g., higher VLP signal), the bigger the volume of gas bursting during the explosions (higher SO_2), as well as the amount of fragmented magma being entrained into the eruptive column (higher thermal) (Ripepe et al, 2008).

5.3.4.2 Insights into gas puffing

Gas puffing activity at Stromboli has been characterised over the last two decades by combined analysis of infrasonic transients and thermal imagery (Harris and Ripepe, 2007). Based on results of model calculations predicated upon results of the above geophysical studies, it was concluded that puffing activity may account for a substantial fraction (~50%) of Stromboli's total gas flux (Ripepe et al., 2008). However, no direct gas flux data have ever been reported in favour of or against this hypothesis, since the high frequency of puffing degassing (with a period ranging

between 0.8 and 1.2s) has precluded the use of data from the previously available (scanning) gas techniques.

Here, we have presented the first direct SO_2 mass measurements of individual gas puffs, showing that these spread over a quite large range, from as low as 0.03 kg to as high as 0.45 kg (section 5.3.3.3 and Figure 54). Using the numbers above as lower and upper limits, and assuming that SO_2 makes up 4.8 wt % of a puff (as quoted by Burton et al., 2007a for the quiescent Stromboli's plume), we compute that the total gas mass emitted in each gas puff would fall in the 0.6-9 kg range (average, ~5 kg). Our direct measurements thus disagree with previous estimates (10-30 kg; Harris and Ripepe, 2007; Ripepe et al., 2008), based on indirect (thermal imagery) analysis, in suggest that puffing's contribution to the total volcano's gas budget may in fact be far more marginal (3-8%) than previously thought.

Ripepe and Gordeev (1999) proposed that puffing at Stromboli is associated with surface bursting of decimetre-sized gas bubbles (~0.5 m radius), produced by coalescence (in the shallow conduit) of clouds of smaller layered bubbles (Manga, 1996). The coalescence of gas bubbles at Stromboli is indeed supported by textural studies on scoria samples (Polacci et al., 2009), providing strong evidence that bubbles with radius > 0.4 mm coalescence, for pressures <50 MPa, to form networks of continuously connected vesicles, through which gas may eventually percolate to sustain quiescent (passive) gas emissions (Burton et al., 2007b). Periodic collapse of percolation pathways, and/or additional coalesce events at the top of the magmatic column, may ultimately allow for development of over-pressured gas pockets, which burst, leading to repeated puffing activity. Assuming a gas overpressure inside the bubble before bursting of $2.2 \cdot 10^4$ Pa (Ripepe and Gordeev, 1999), and a gas temperature of 1373°K, we infer, from our derived mass (5 kg) for individual gas puffs, a corresponding gas bubble volume of 0.14 m^3, which, for spherical bubble geometry, would lead to a bubble radius of ~ 0.32 m, very close to the previous estimate (0.5 m) of Ripepe and Gordeev (1999). This match provides mutual confidence in both the geophysically based (Ripepe and Gordeev, 1999) and gas-based (this study) evaluations of this parameter.

5.3.5 Conclusions

Stromboli has been for decades an ideal laboratory for studying the different modes and rates of gas release from active volcanoes. Yet, a clear quantitative understanding of the relative contributions of passive and active degassing to the total gas budget has been long unavailable.

Here, we have detailed results of a first field attempt to simultaneously assess SO_2 release from the three main forms of degassing at Stromboli (Fig. 55). By exploiting the high spatial and temporal resolution of UV cameras, we have acquired image sequences for 147 strombolian explosions, and estimated an SO_2 mass output of individual eruptions of 2-55 kg. This corroborates previous indications that explosive degassing contributes to 7±1.5 % of the total SO_2 flux (Fig. 55). We have also performed an integration with geophysical data to derive information on the mechanisms behind the explosions. It is a well accepted idea that the VLP seismic events at Stromboli are driven by generation and ascent of a gas slug within the upper conduit, with the majority of the VLP signal originating at 220-300 m depth (Chouet et al., 1999, 2003). We have here demonstrated a positive correlation between VLP amplitude of each individual explosion and its corresponding syn-explosive SO_2 mass release, and shown a systematic simultaneous occurrence of the onset of gas release and the deflation phase of the VLP pulse. This suggests that the VLP signal is inextricably connected, not only with the in-conduit eruption trigger, but also (perhaps even primarily) with the dynamics of syn-explosive gas release at the top of the magmatic column. Comparison with thermal imagery data demonstrates, instead, a nearly synchronous (± 1.2 s) emission of gas and hot pyroclasts during the explosions, and highlights a difference between ash-free and ash-dominated explosions, related to the higher emissivity of the ash relative to coarse pyroclastic materials.

In addition, we have reported on the first direct measurements of the SO_2 mass contributed by individual gas puffs (ranging 0.03-0.45 kg), thus showing that puffing contributes to only < 10 % of the total SO_2 flux, and is therefore far less than

previously suggested by indirect geophysical evaluations (~ 50%). From the estimated total gas mass (~5 kg) per puff, we argue that each individual gas puff is generated by top-of-the conduit bursting of a gas bubble of ~ 0.32 m radius, likely produced by gas coalescence in the top few meters of the magmatic column.

We conclude that, despite the coexistence of different modes of gas release, passive degassing remains the primary mechanism of gas loss at Stromboli volcano, and probably also at many other basaltic volcanoes.

5.4 Periodic degassing from the north-east crater (Etna, Italy)

5.4.1 Introduction

The large variety of volcanic manifestations in nature primarily reflects the range of physical-chemical properties of magmas, which in turn determine the conditions of magmatic ascent and eruption (Symonds et al., 1994; Giggenbach, 1996; Allard, 1997; Sparks, 2003; Parfitt, 2004). Among the key casual factors in volcanic processes, the mantle-inherited original volatile content of magmas (Wallace, 2005), and the mechanisms governing volatile degassing from silicate melts (Carroll and Holloway, 1994) play a major role on magma rheology and differentiation, and ultimately determine whether an effusive or an explosive eruption is to occur. At open-vent basaltic volcanoes, in particular, gas bubbles are thought to be buoyant enough to separately ascend within the low viscosity melt, to sustain open-vent passive gas emissions (Burton et al. 2007) or eventually coalesce into the larger gas pockets driving Hawaiian- to Strombolian-style explosions (Macdonald 1972, Chouet et al., 1974; Blackburn et al.,1976; Jaupart and Vergniolle, 1988; Ripepe et al., 1993; Vergniolle and Brandeis 1994, 1996). Gas segregation also drives magma convection (Harris and Stevenson, 1997; Stevenson and Blake, 1998) and the consequent excess degassing behaviour observed at most basaltic volcanoes (Allard et al., 1994), and is involved in magma dehydration (and thus crystallization, Métrich et al., 2010) and in the generation of LP to VLP volcano seismicity (Chouet, 1992, 1996, 2003).

Measuring the rates of surface gas release from active volcanoes may in principle provide key insights onto the mechanisms and rates of gas flow in conduits, thus potentially contributing to understand the transition between different activity styles (Jaupart and Vergniolle, 1988; Parfitt and Wilson, 1995). Real-time, high-frequency, gas observations have traditionally been challenging (McGonigle and Oppenheimer, 2003), however, and most of the available volcanic gas flux time series (e.g., Caltabiano et al., 2004) lack the temporal resolution required to investigate volcanic processes which take place over timescales of seconds to minutes (e.g., Strombolian explosions).

The very recent advent of new UV imaging techniques (Mori and Burton, 2006; Bluth et al., 2007, Kantzas et al., 2010) has represented a real breakthrough in the field of volcanic gas observations, first allowing acquisition of SO_2 flux time series with unprecedented high resolution (~1 Hz), and thus opening the way for the characterization of volcanic processes inaccessible to previous research. Whilst prior research has primarily targeted inter-comparison with simultaneously acquired geophysical signals (Dalton et al., 2010; Kazahaya et al., 2011), and SO_2 budget estimates for Strombolian explosions (Mori and Burton, 2009; Kazahaya et al., 2011; this study), no systematic attempt has been made so far to explore the short-term (seconds to minutes) fluctuations in bulk (total) SO_2 flux, and to discuss the implications of these for the currently available models of conduit gas flow, and concerning the switch from passive to explosive volcanic behaviour.

In a previous *section* (cfr. 5.3.3), I have made use of systematic UV camera measurements taken at Stromboli volcano to show that a periodic SO_2degassing regime characterizes volcanoes at which rhythmic Strombolian explosions are regularly interspersed within the quiescent (passive) degassing activity. Explosions have been seen to cause a periodic degassing behavior not only at open-vent basaltic volcanoes such as Stromboli, but also on more felsic volcanic systems where more vigorous (Vulcanian) explosive activity styles are observed (Nadeau et al., 2011).

In this *section*, I report on recent UV camera observations I made on Etna volcano in the attempt to test the hypothesis of whether or not a periodic degassing regime is observed also in cases where explosive activity is virtually absent. Etna's North-East summit crater, in particular, was an ideal site for such a study since, at least during the time interval covered by our measurements, it was characterized by vigorous degassing activity but no explosions. Our results, described below, emphasize that, even at passively degassing volcanoes, volcanic gas surface release occurs in a somewhat periodic regime. This leads to new constraints useful in better understanding the modes and mechanisms of gas flow in conduits, and the timescales of gas separation from silicate melts.

5.4.2 Mount Etna and its SO_2 degassing budget

Mount Etna is one of the most active basaltic volcanoes in the world, and one of the largest volcanic SO_2 point sources to the atmosphere (Allard et al., 1991; Allard, 1997; Caltabiano et al., 1994, 2004). Persistent passive SO_2 plume emissions occur via the four main summit craters (North-East Crater, Voragine, Bocca Nuova and South-East Crater), which contribute to almost the totality of the emitted SO_2. Additional emissions, which are sometime very vigorous, may temporary take place during flank eruptions (Caltabiano et al., 2004). In the last 30 years, first COSPEC, and more recently DOAS, have been used to obtain information on the total daily volcanic SO_2 flux at Mt. Etna. These results have been obtained by either traversing underneath the plume (Caltabiano et al., 1991, 2004), or scanning from a fixed position (Salerno et al., 2006). The SO_2 flux was found to vary from $\leq$1000 $t \cdot d^{-1}$ during low passive fuming activity, to 10000-25000 $t \cdot d^{-1}$ during high Strombolian activity and lava-fountaining paroxysms (Allard, 1997, Caltabiano et al., 1994). Based on these data, the volcano has been suggested to account for 8-10 % of global volcanic SO_2 gas emissions (Stoiber et al., 1987). According to Caltabiano et al. (2004), Etna's SO_2 time series allows for identification of two main cyclic components, with periods of ~1 and ~4 years, respectively. The former periodic behaviour (Fig. 59a) has been explained as due to a seasonal influence of solar zenith angle, meteorological parameters and tidal forces on the measurements; whilst the latter (Fig. 59b) may be related to periodicity in magma supply and replenishment, which may in turn control the timing of more intense volcanic activity (Caltabiano et al., 2004).

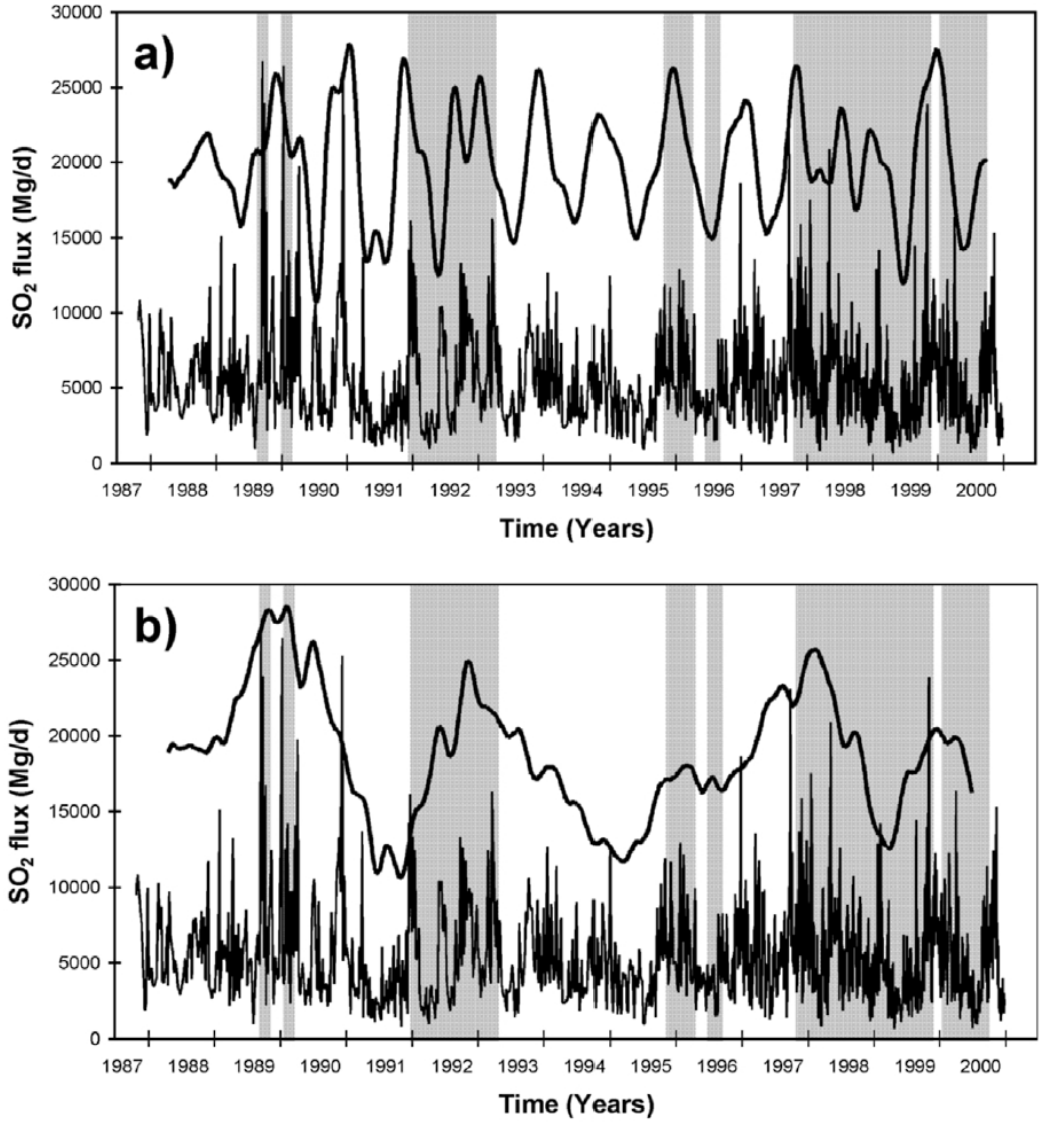

Figure 59: Band pass filtering on SO_2 signal. (a) The tick curve in the upper part of the graph highlights the 1-year component. (b) the tick curve in the upper part of the graph highlights the 4-year component. The filtered signals are shown in arbitrary units. The gray bars indicate Mt. Etna's eruptive activities (Caltabiano et al., 2004).

The low sampling frequency of traditional scanning techniques has restricted exploration of periodicity in degassing behaviour to timescales greater than days, therefore precluding observation and analysis of short-term fluctuations and periodicity in emissivity over timescales of seconds to hours. Exploration of these rapid SO_2 degassing features at Etna is the main target of this *section*.

5.4.3 Observations and technique

Degassing on Mt Etna is primarily sourced by continuous emission of gas from four summit open vents (Allard, 1997). Visual observations (Fig. 60) indicate that the North-East Crater differs - as is the case for its degassing regime - from other vents, in that it is systematically associated with intermittent emissions of gas as clouds or puffs, typically spaced about tens of seconds from each other. This "puffing" behaviour is most evident when viewed from the rim of the crater: gas emission virtually stops between one puff and the next.

Figure 60: Mt. Etna North East (right) and centrals craters (left) seen from Pizzi Dineri.

As mentioned above, no effort has ever been spent in the past to identify the high-frequency patterns of SO_2 flux variation from the North-East crater, to relate them to the puffing behaviour observed at that vent, and to explore the source (conduit) mechanisms controlling this degassing behaviour. To fill this gap , we performed (from the 1st to the 4th of July 2011) a dedicated field campaign capturing germane SO_2 flux data. Observations were taken (using the instrumental configuration detailed in *chapter* 4) from Pizzi Deneri, a site located on the upper north-eastern flank of Etna, at 2800 m a.s.l., and ~4 km distant from the crater terrace. This location ensured an ideal view of the North-East crater's plume, particularly in low wind speed conditions, when the gas typically lofted vertically ~20-30 meters above the crater's rim, before being transported quasi-horizontally above the summit crater's terrace (Fig. 60). After travelling a distance of ~450 m , the gas plume issuing from the

North-East crater mingled with the surrounding gas emitted by nearby Voragine and Bocca Nuova craters, before being collectively dispersed within the "bulk" summit's plume, entraining the south-east crater plume and being advected over the Valle del Bove (Fig. 61).

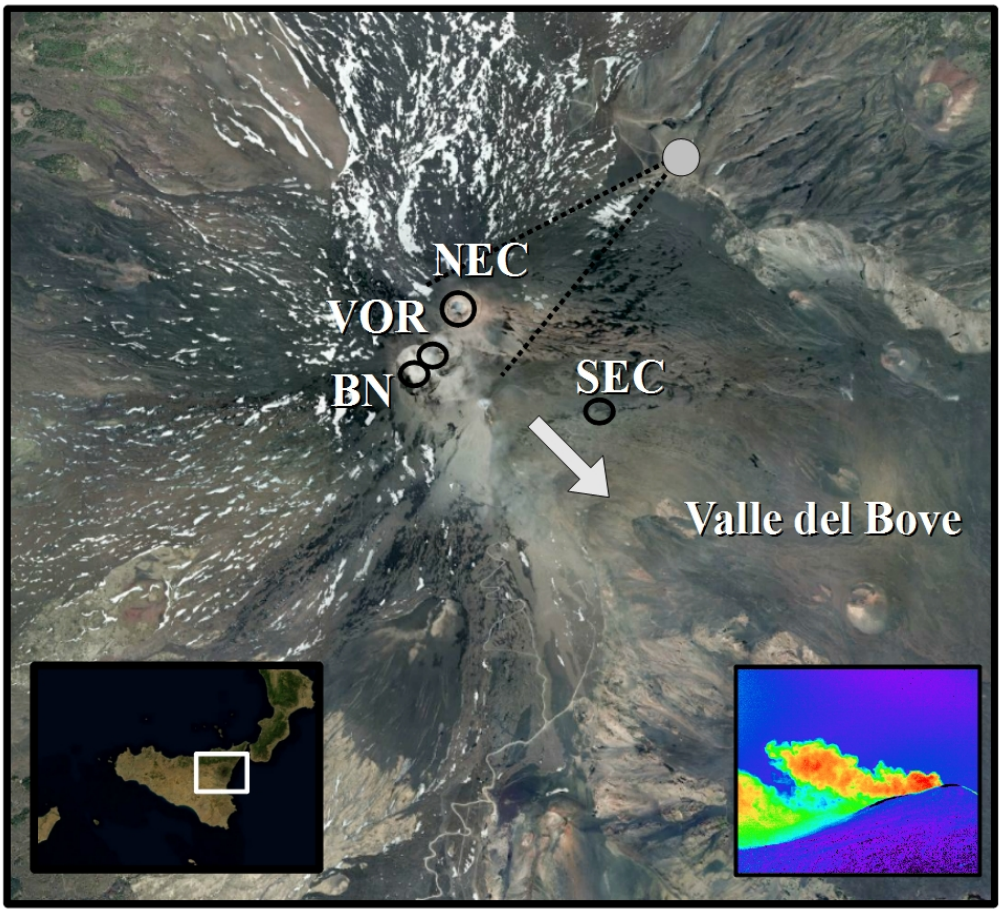

Figure 61: Map of the summit area of Mt. Etna (modified from Neri et al., 2008), showing the location of the UV camera measurement site (gray circle) and its field of view.

During our observations, the wind field on the volcano's summit was dominated by north-westerly winds, which led to a roughly perpendicular view of the moving plume from our measurement site (see Fig. 61). A number of mild gas-driven ash explosions took place at the central crater (Bocca Nuova, Fig. 62) during the measurement interval, typically lasting a few tens of seconds at most. From reports made available by INGV-Sezione di Catania, we conclude that the explosions were only marginally magmatic in nature, and that the emitted ash mostly consisted of lithic fragments (from the rock cap obstructing the Bocca Nuova vent at that time), with a

marginal juvenile component. These explosions did not affect the SO_2 flux record from the central craters.

Figure 62: Ash explosion from Bocca Nuova crater.

The SO_2 flux was measured with a sampling frequency of ~ 0.5 Hz, taking two distinct vertical cross sections of the horizontally dispersing plume. Pixel-to-pixel SO_2 variations along both the two profiles were integrated to obtain SO_2 ICA (integrated column amount), and finally (after multiplying by the plume transport speed), SO_2 fluxes. The integration sections were chosen as follows. A first plume cross section was taken ~40 meters downwind the North-East crater, to obtain a fine record of the SO_2 flux contribution from that individual vent. The second section was taken further downwind, above the southern upper rim of Valle del Bove, and was used to derive time series for the total (North-East + Central craters) SO_2 flux (Fig. 63). The SO_2 contribution from the South-East crater was irrelevant during our measurements, and is neglected here.

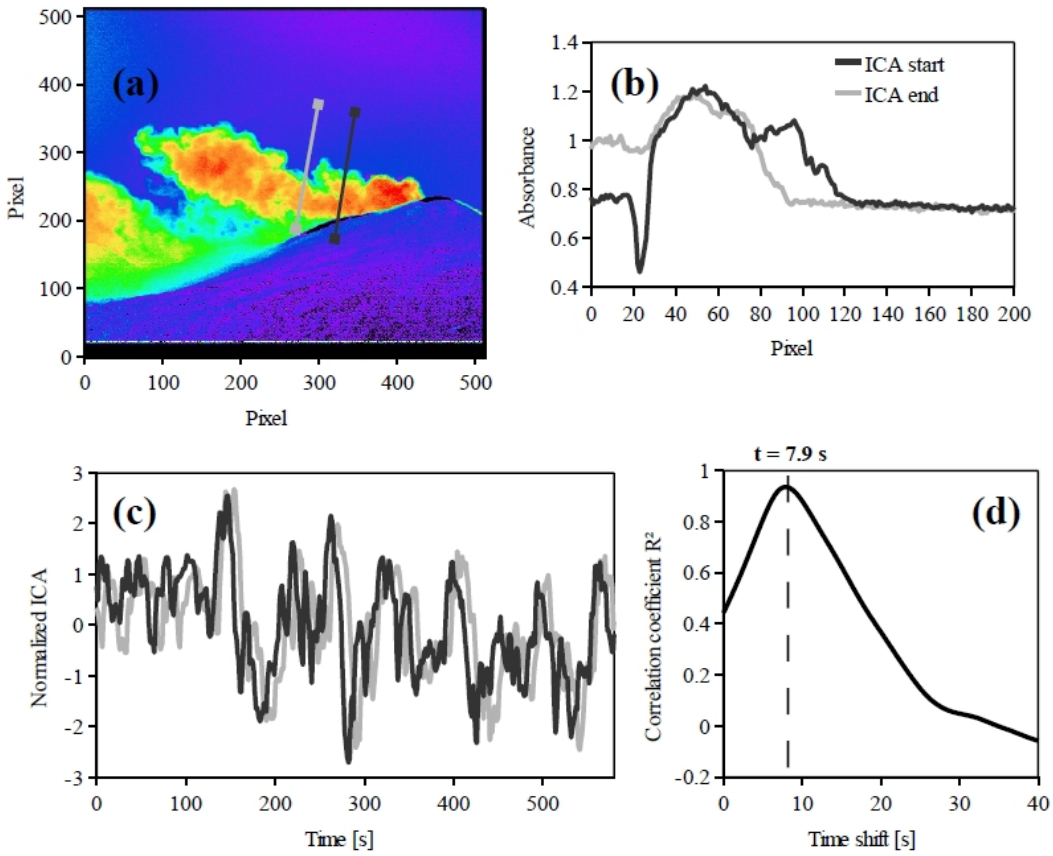

Figure 63: (a) SO_2 column amount image of the NE crater plume and the position of the two parallel cross section (gray and black lines) from which absorption profiles were calculated (b) and integrated to obtain two ICA time-series (c). The cross-correlation function (d) shows the optimal time-shift for the best overlapping of the two ICA time series.

The plume transport speed was obtained using the procedure detailed in section 4.1.5, and involved calculation of the cross-correlation coefficients between two column amount time-series obtained from two parallel and closely spaced (~100 m) plume's cross-sections (Fig. 63a). The so-derived plume transport speed ranged from 11.4 to 17.2 $m \cdot s^{-1}$, and deviated substantially from directly measured wind speed data (simultaneously measured on top of Pizzi Dineri with a portable anemometer, and ranging from 4.9-17.4 $m \cdot s^{-1}$) over a large part of the acquisition window (Fig. 64). This discrepancy may be explained in that convection (rather then dispersal by wind) determines the plume ascent hundreds of meters from the vent, and/or that orographic effects create a very complex and often unpredictable wind field over the volcano's summit.

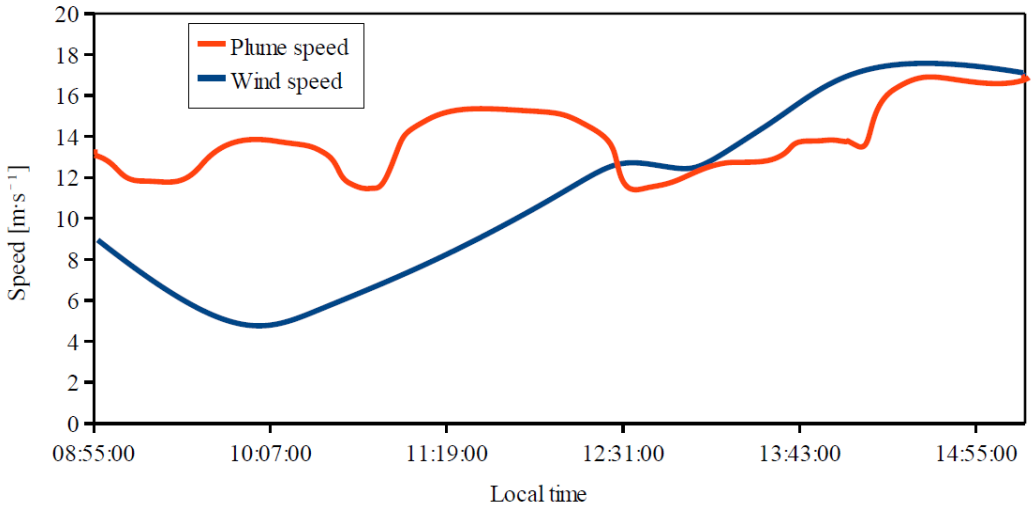

Figure 64: Calculated plume speed through cross-correlation and averaged wind speed measured on the top of Pizzi Dineri.

5.4.4 Results

Taken as a whole, the several consecutive hours of UV imaging observations indicate a total SO_2 flux from Etna ranging 2-50 kg·s^{-1} (for the 1st, 2nd and 4th of July period). Our daily SO_2 flux averages (21.9 kg·s^{-1}, 16 kg·s^{-1} and 9 kg·s^{-1} respectively) for the 3 days are close, or somewhat lower, than the typical SO_2 flux regime associated with the last decade of Etna's degassing activity (~20 kg·s^{-1} over the post 2001 period; INGV-Catania, internal reports). The SO_2 flux contribution from the North-East crater ranged from 1-29 kg·s^{-1} (average at 12.8 kg·s^{-1}, 10.5 kg·s^{-1} and 5.7 kg·s^{-1} respectively; Table 2), and therefore accounted for almost 40% of the total SO_2 flux, in agreement with previous evaluations based on walking traverses with mini-DOAS (Aiuppa et al., 2008; La Spina et al., 2010).

Date	Average	St. Dev.	Min	Max
1 July 2011	12.8 kg·s^{-1}	3.5 kg·s^{-1}	2.5 kg·s^{-1}	25 kg·s^{-1}
2 July 2011	10.5 kg·s^{-1}	4.3 kg·s^{-1}	1 kg·s^{-1}	28.7 kg·s^{-1}
4 July 2011	5.7 kg·s^{-1}	1.7 kg·s^{-1}	1.6 kg·s^{-1}	15.4 kg·s^{-1}

Table 2: Daily average of the SO_2 flux from the NE crater during our observation period.

As regards the high-frequency structure of the acquired SO_2 time series, our dataset clearly supports the existence of a non-stationary (periodic) degassing SO_2 regime from the North-East crater. Data obtained on July the 1st are shown in Fig. 65c as an example of the typical time-series obtained. These data show that the puffing degassing behaviour, which is clearly visible from visual observations at the vent's rim, is captured in our time-series in the form of nearly continuous oscillations of the SO_2 flux which, while varying in amplitude and period over the six hours of acquisition, are present throughout the entire dataset (Fig. 65b).

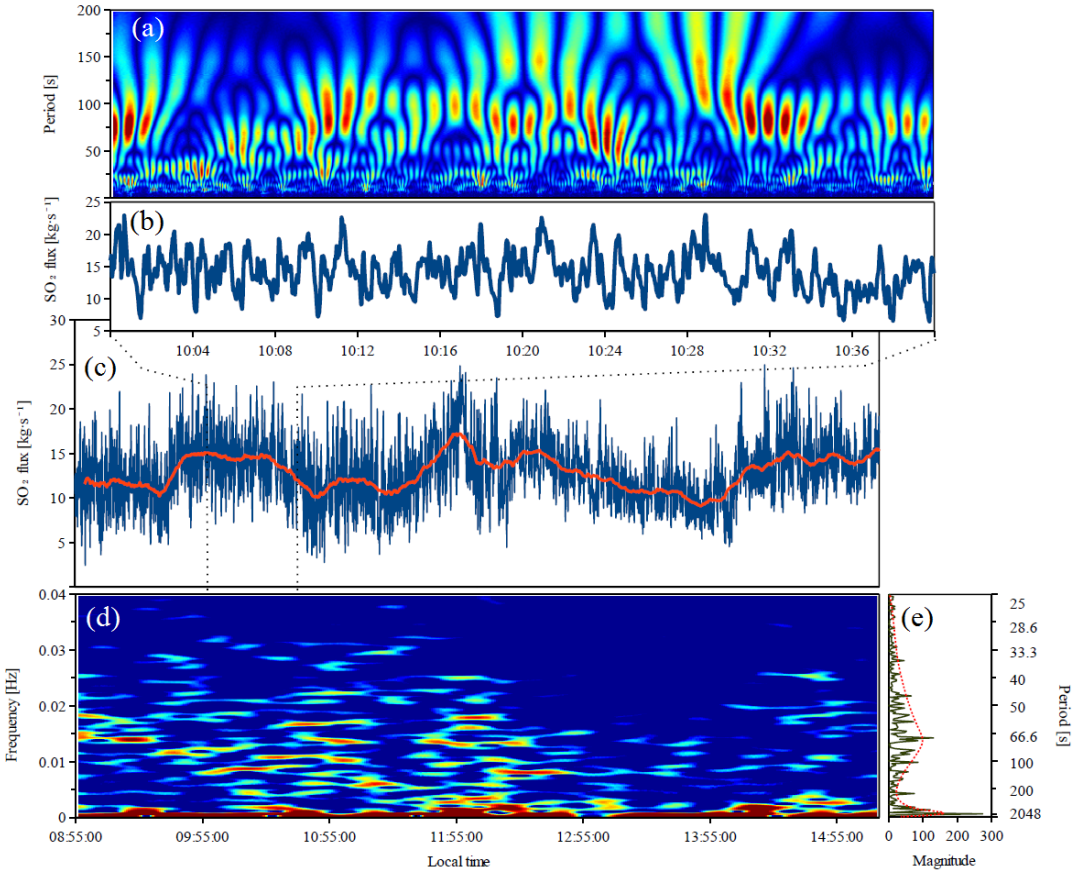

Figure 65: (a) A complex Morlet wavelet highlights the short-term variations of the periodicity in a subinterval (b) of the entire SO_2 flux time-series (c) of the 1th of July 2011 dataset. Cycles of increase and decrease of the periods in the range 40-200 s are observed. (d) A mobile average (red line) highlights the high period (> 1 h) components of the signal. (d) The spectrogram is obtained from a moving window of 2048 s, an overlapping of 2000 s, and a frequency resolution of 10^{-4} Hz. It shows the non-stationarity of the spectral components between 40-250 s and the attenuation of puffing magnitude after 12:55:00. (e) A Fast-Fourier-Transform of the SO_2 flux time series.

We broadly distinguish two SO_2 variation patterns:

1. low period SO_2 flux fluctuations, lasting tens of seconds, and having a mean amplitude of ~ 6 $kg \cdot s^{-1}$ (therefore accounting for ~50% of the average flux). On a typical sequence of consecutively collected UV images, this degassing pattern is clearly detectable as a succession of sizeable clouds of highly concentrated SO_2 being rhythmically released by the vent's rim (Fig. 65b);
2. longer period flux fluctuations, lasting thousands of seconds, and only barely identifiable in a time series of 6 hours. In Fig. 65c, these longer period cyclic fluctuations in SO_2 release are highlighted by the moving average.

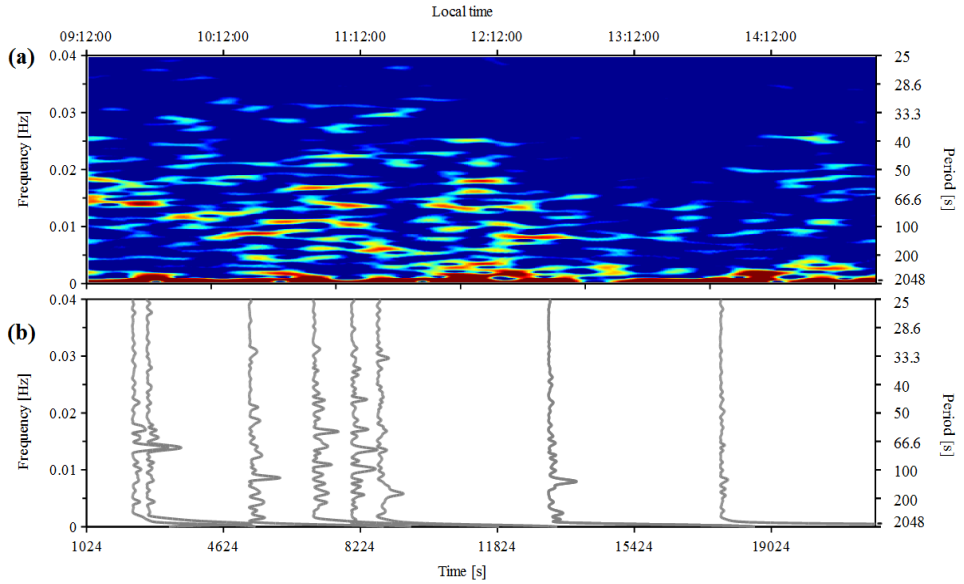

Figure 66: A detail of the above spectrogram: the sections show that puffing frequency is stable over timescale shorter than hundreds of seconds.

The spectrogram and the Fast-Fourier-Transform (FFT) curve, shown in Fig. 65d-e, identify the two main spectral components clearly. The spectrogram, shown in Fig. 65d, was obtained from the data on 1st July using a moving window of 2048 s, an overlapping of 2000 s, and a frequency resolution of 10^{-4} Hz. The diagram confirms that while the long period component (>2000 s) is fairly stable in time, the periodicity of gas puff release is not constant, and there is not even a well-defined dominant

frequency, but instead a band of frequencies represented, in the 0.005-0.025 Hz range. This feature is supported further by profiles in Fig. 66b, which demonstrate that puffing frequency, while often being relatively stable over timescales shorter than hundreds of seconds, is instead barely characterized by a constant/dominant frequency for timescale longer than a thousand of seconds. Sometimes, more than one low frequency peak is well represented at any give time (Fig. 66b). These observations suggest, therefore, that the pulsate gas discharge mechanism, which ultimately controls the North-East crater's puffing behaviour, is not occurring at a strictly constant rate, but that its typical period is modulated over timescale of minutes to hours.

In light of the complexity of the spectral distribution, we have also attempted the use of a continuous transform with a complex Morlet wavelet, a detail of which is given in the upper panel of Fig. 65A and 67. Such a highly detailed wavelet spectrogram confirms the existence of smooth variation of the spectral components, which implies that the frequency at which gas puffs are released varies over timescale of a few minutes. Three main patterns can be identified in the wavelet spectrogram:

i. Short term patterns (hundreds of seconds), in which the puffing rate is barely constant (e.g., from 8:55-10:25 local time);
ii. Long term patterns (thousands of seconds), in which the puffing rate changes continuously, and the puffing period varies progressively (or, sometimes, even abruptly) from ~300 s to <100 s (e.g., from 10:25-12:40 local time);
iii. Patterns of weak puffing activity (e.g., from 12:40-15:10 local time), when the periodicity in gas emission is less marked, or even disappears.

We stress that similar patterns have been observed in plume cross-sections taken at only a few meters above the crater's rim, therefore immediately upon emission. We therefore rule out the interpretation that the observed pulsate degassing regime (puffing) is formed upon plume dispersion in the atmosphere, and/or that atmospheric transport process can modify the puffs structure to a significant extent over the plume ages associated with our measurements.

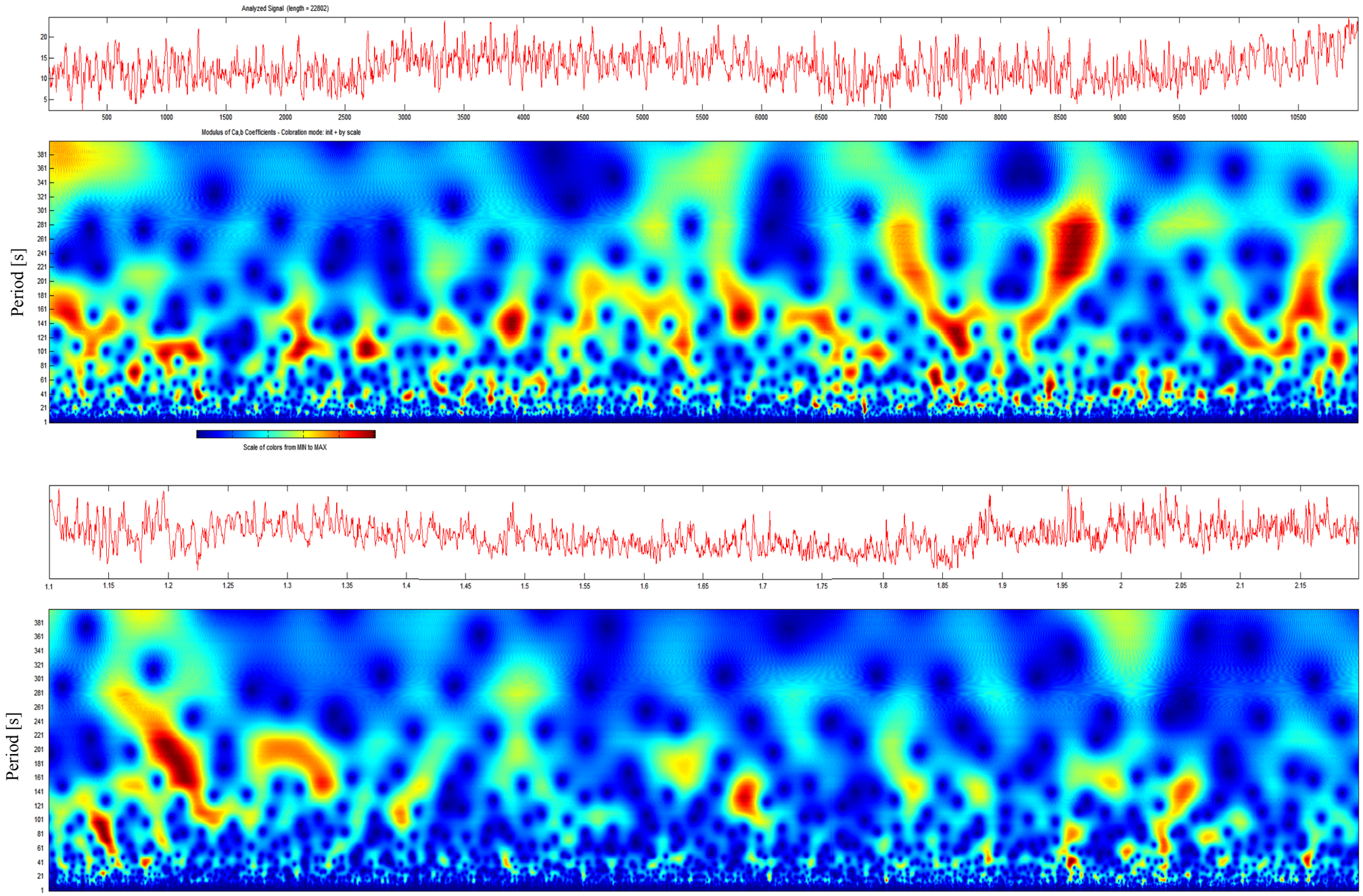

Figure 67: A complex Morlet wavelet of the 1th July 2011 SO_2 flux time-series in the range 1-400 s and a resolution of 1 seconds.

In the attempt to explore the periodicity of gas release at Etna even more deeply, and specifically to compare datasets available for the different days of observations, we have applied basic spectral analysis to the flux time-series; using, in particular, appropriate representations (spectrograms) which characterise the extent to which the SO_2 flux signal's spectral density varies over time. With this aim, we have calculated a Welch power spectral density function (PSD) for our data-set (also including results of a single-day campaign performed on 14 May 2011), and have consequently explored the day-to-day variability of the spectral components. The PSDs, high-pass filtered (>0.003 Hz) and normalized for a better comparison (Fig. 68a), indicate that a long period (50-500s) cyclical degassing behaviour is manifest in all available acquisitions. The same frequencies are roughly recurrent in each acquisition, though with different relative amplitudes for each day (and, for one of the days, the amplitudes change over timescales of thousands of seconds or less). To identify the most characteristic (stable) periods of gas flux modulation, we have performed a dot-to-dot product of the 4 normalized PSDs, which shows (Fig. 68b) that the periods common to all signals are essentially ~ 250s, ~125s and ~60s.

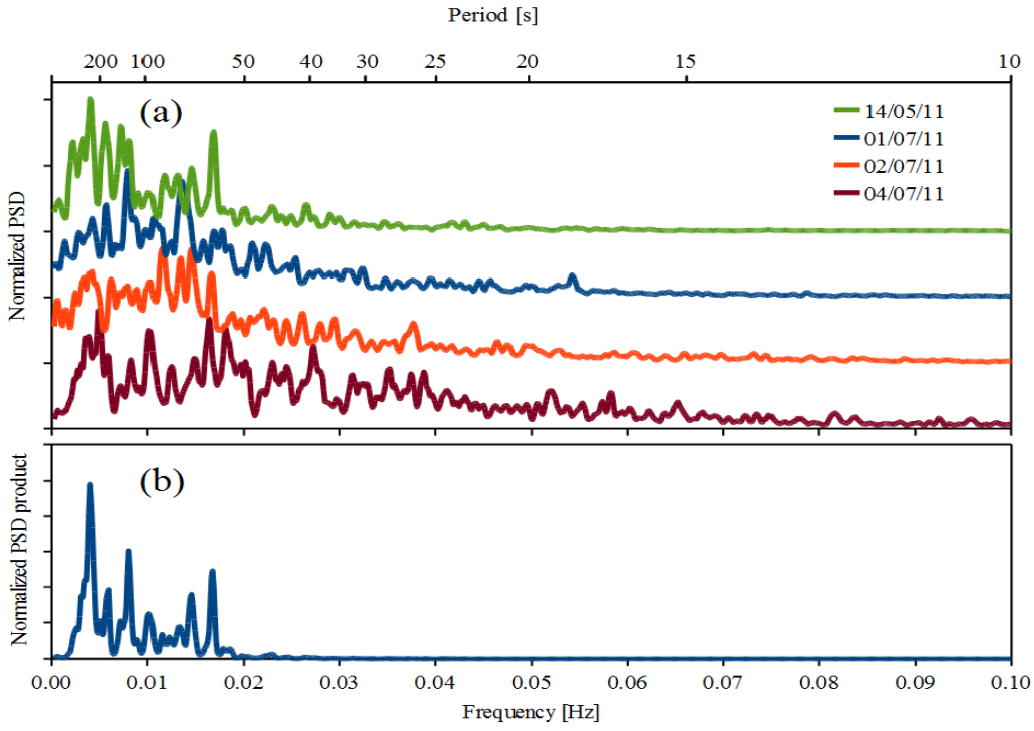

Figure 68: Normalized high-pass filtered Welch power spectral density of 4 NE crater SO_2 flux time series (top) and their product (blue line on the bottom graph).

5.4.5 Implications for degassing

The observations detailed above strongly support the conclusion that gas release from passively degassing volcanoes, when explored at high (0.5 Hz) rate, contains a periodic signature. In this, our measurements reinforce recent conclusions made based on high-frequency SO_2 flux observations at Erebus volcano (Boichu et al., 2010). The idea of periodic passive degassing behavior, for which we provide here convincing experimental evidence, is consistent with visual observations indicating that passive gas release at open-vent volcanoes is not a stationary (continuous) process, but occurs instead as a sequence of intermittently released individual gas pockets (*gas puffs*). Hitherto, this *puffing* degassing behavior has normally been thought to be associated with the bursting of over-pressured gas pockets at the magma-air interface (Harris and Ripepe, 2007), each of these bursting episodes releasing a small pressure wave (infrasound) in the surrounding atmosphere.

At Etna, however, attempts to correlate our SO_2 flux time series with infrasonic data (an example of which is shown in Fig. 69; taken from the INGV Catania monitoring network; courtesy of Andrea Cannata) led to insignificant results.

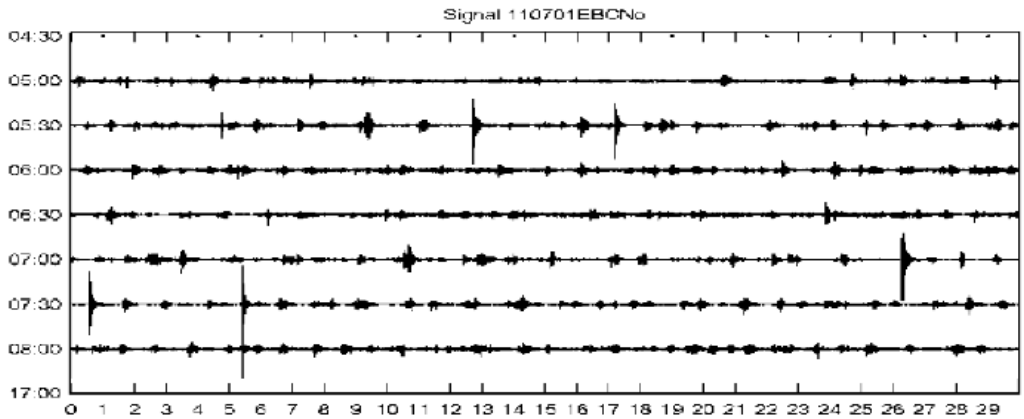

Figure 69: An example of infrasound signal acquired with a monitoring station of INGV Catania. Each sharp pressure transient represents on explosive events from the NE crater.

From an infrasonic dataset coeval with our SO_2 flux time series, we first calculated an infrasonic RMS (root mean square, a statistical measure of the magnitude of a periodic signal) in the 0.1-0.6 Hz spectral window (green line in Fig.

70), which is the frequency range containing most of the energy irradiated by the bursting events from North-east crater (see the sharp pressure transients in Fig. 69). However, the RMS turned out to be too noisy; we therefore tried to isolate the bursting events by calculating the spectral amplitude of the signal in the 0.3-0.5 Hz range (Fig. 71)

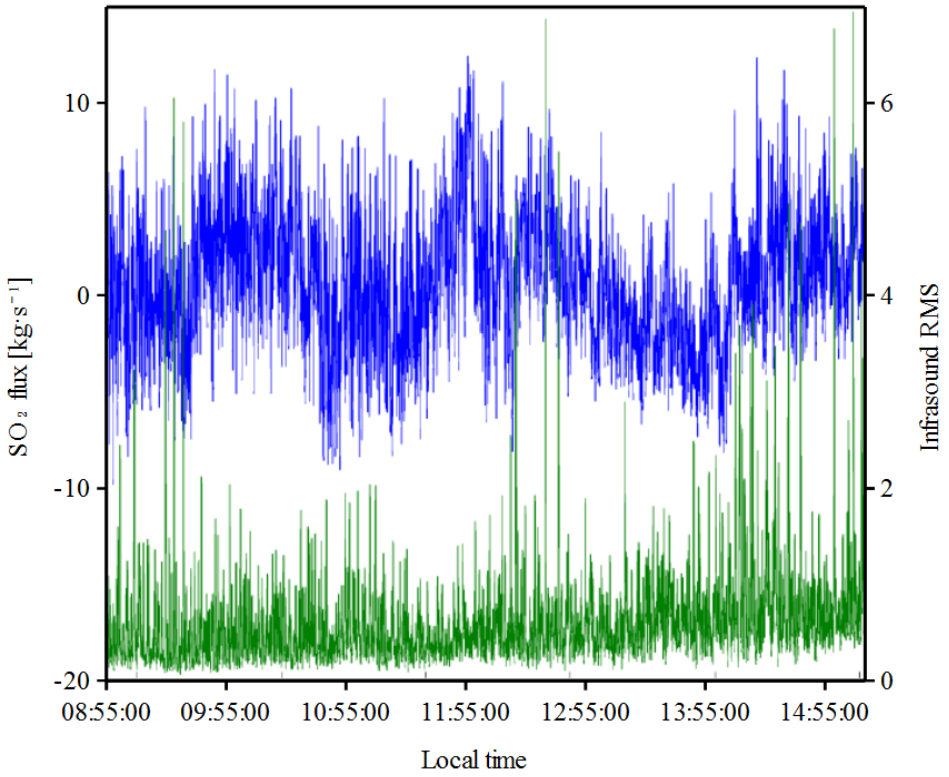

Figure 70: SO_2 flux signal (blue) and infrasound RMS (green) of the 1th July 2011.

However, even in such a second eventuality, no obvious correlation between SO_2 gas emissions and infrasonic activity was seen to emerge. We conclude, therefore, that the cyclic trends in gas flux emissions, visible in Fig 65, must be associated with a different physical process than that sourcing the infrasonic activity observed at the North-East crater (bursting of over-pressured gas bubbles upon emission; Cannata et al., 2009). We propose, instead, that the rhythmic ascent of gas bubbles through the magmatic column filling the upper vent's conduits, followed by quiescent discharge of gas (in mechanical equilibrium with surrounding magma-air) at the vent, sustain the observed periodic degassing pattern. In order to reconcile this mechanisms with the temporal periods (40-250 s) over which gas flux emissions fluctuate (Fig. 68), it

would have to be admitted that rates of gas ascent/release in volcanic conduits can vary over time scales of minutes.

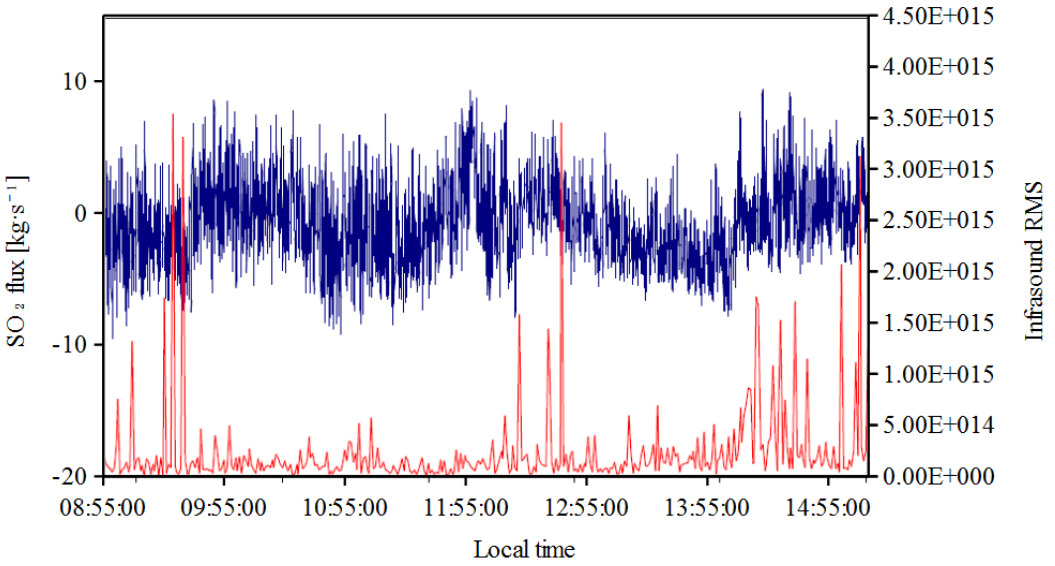

Figure 71: SO_2 flux signal (blue) and spectral amplitude of the signal (red) in the 0.3-0.5 Hz range of the infrasonic signal of the 1th July 2011.

Persistent degassing at basaltic open-vent volcanoes is best explained by a convection mechanisms in which a bi-directional flow of magma occurs in the conduit, with a less dense gas-rich magma ascending through a sinking degassed (and thus denser) magma (e.g., Shinohara, 2008). In this context, the oscillatory behaviour of SO_2 degassing at the North-east crater may simply reflect aperiodic rate of magma convection. However, passively degassing inherently requires separate ascent of gas bubbles within the silicate liquid matrix; making therefore the hypothesis more plausible that the SO_2 periodic behaviour is simply due to inhomogeneous distribution of gas bubbles rising through the gas-bearing magmatic column. More specifically, we test here the hypothesis that *passive gas puffing* reflects ascent in the conduit of layers (trains) of gas bubbles (Manga, 1996), which ultimately discharge at the magma-air interface individually, and rhythmically. We assume that bubbles are present in the conduit, and that magma velocity is small compared with bubble rise speeds, so that convective motions in the liquid do not disrupt layers and disperse the bubbles. Following Manga (1996), the gas bubble layers would be separated by a distance λ, for which we can calculate the smallest unstable wavelength:

$$(16)\quad \lambda > 2\pi\sqrt{\frac{5\cdot a^5\cdot \Delta\rho\cdot g}{3\cdot\mu\cdot\kappa}}$$

In the above relation (taken from Manga, 1996), a is the bubble radius, $\Delta\rho$ is the density difference between the liquid and the bubble, μ is the magma viscosity and κ is the diffusivity of the volatiles through the magma. The rise speed $U(\Phi)$ of each bubble layer depends on the local bubble concentration Φ, according to:

$$(17)\quad U(\phi) = U_0\left(\frac{1}{1+\phi}\right)^n$$

where U_0 is the rise speed of a single bubble, determined by Stokes' law:

$$(18)\quad U_0 = \frac{a^2\cdot\Delta\rho\cdot g}{3\cdot\mu}$$

The time lag τ between the surface discharge of a given layer of bubbles and the following is given by:

$$(19)\quad \tau = \frac{\lambda}{U(\phi)}$$

Equations 16, 17, 18 and 19 can be rearranged to calculate the dependence of the time lag τ on concentration of bubbles in the melt (Φ). With the aim of deriving such a $\tau(\Phi)$ function, we assume a magma at 1100°C, with a density of 2600 kg·m^{-3} and a viscosity of ~300 Pa·s; we also consider water as the dominant gas species inside the bubbles (H_2O exceed 80 % in the Etna's upper conduit gas phase; Aiuppa et al., 2007; Shinohara et al., 2008), and we therefore use its diffusivity coefficient: κ at 1100°C (see Fig. 72, Zhang & Stolper, 1991) throughout the calculations.

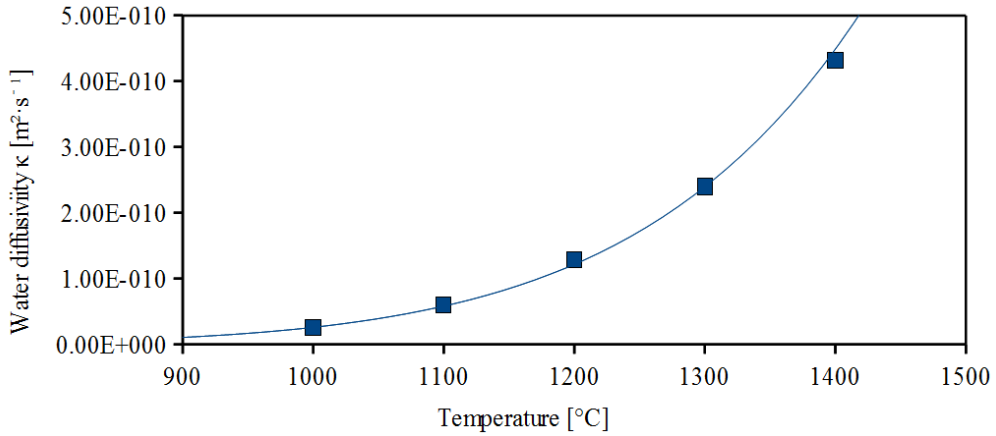

Figure 72: Diffusivity of water in a basaltic magma at different temperatures (Zhang and Stolper, 1991).

We have calibrated our model by using textural data (vesicularity, bubble dimension) of the pyroclasts erupted during the August-December 2007 Etna's explosive activity (Polacci et al., 2009). These explosive products exhibit a high degree of vesicularity (70-81 % vol.) and a population of large (from hundreds of micron to >1 cm) coalesced single vesicles. In Fig. 73, we show the solution of our $\tau(\Phi)$ function for four different values of bubble radius *a,* falling within the Polacci et al., (2009) range of values. We also obtained two different solutions (shown separately in Figures 73 a and b), depending on which value of n is adopted in Eq. 17 between 3 and 5 (see related discussion in Manga, 1996).

We make the hypothesis here that our measured low period component in gas flux emissions (range, 40-250 s; Fig 68) is a proxy for the time lag τ. Using this range of τ (dashed horizontal lines in Fig. 73) in tandem with the 70-81% vesicularity range (yellow coloured area), we find that solution 1 (obtained with n=3; Fig. 73a) works well over the entire range of *a* values used (best fit for bubble radii of ~0.5-1 mm); while solution 2 (Fig. 73b) creates a range of model $\tau(\Phi)$ functions which would require improbably large (radius >10 cm) bubbles to be consistent with experimental (vesicularity and gas periodicity ranges) data.

We admit that the above model calculations are an over-simplification of a far more complex physical scenario: separate gas flow in non-Newtonian viscous fluids is likely a far more intricate process than predictable with the above equations. The

experimental results of Divoux et al. (2009) suggest, for instance that - in non-Newtonian fluids - intermittent switching between different gas regimes, such as bubbling (rising of individual bubbles) and winding-flue (development of networks of interconnected bubbles, permeable to gas flow), can naturally occur: this process, if found to be relevant to magmatic fluids as well, may act as an additional source mechanism determining pulsate degassing at volcanoes. With these notes of caution in mind, we still conclude that a process of gas packaging into trains of discrete bubble-rich layers, when coupled with time variations in ascent rate of individual layers (due to inhomogeneities in gas vesicularity and bubble dimension over the conduit length), may well account for the time-dependent periodicity of volcanic SO_2 flux emissions, observed here.

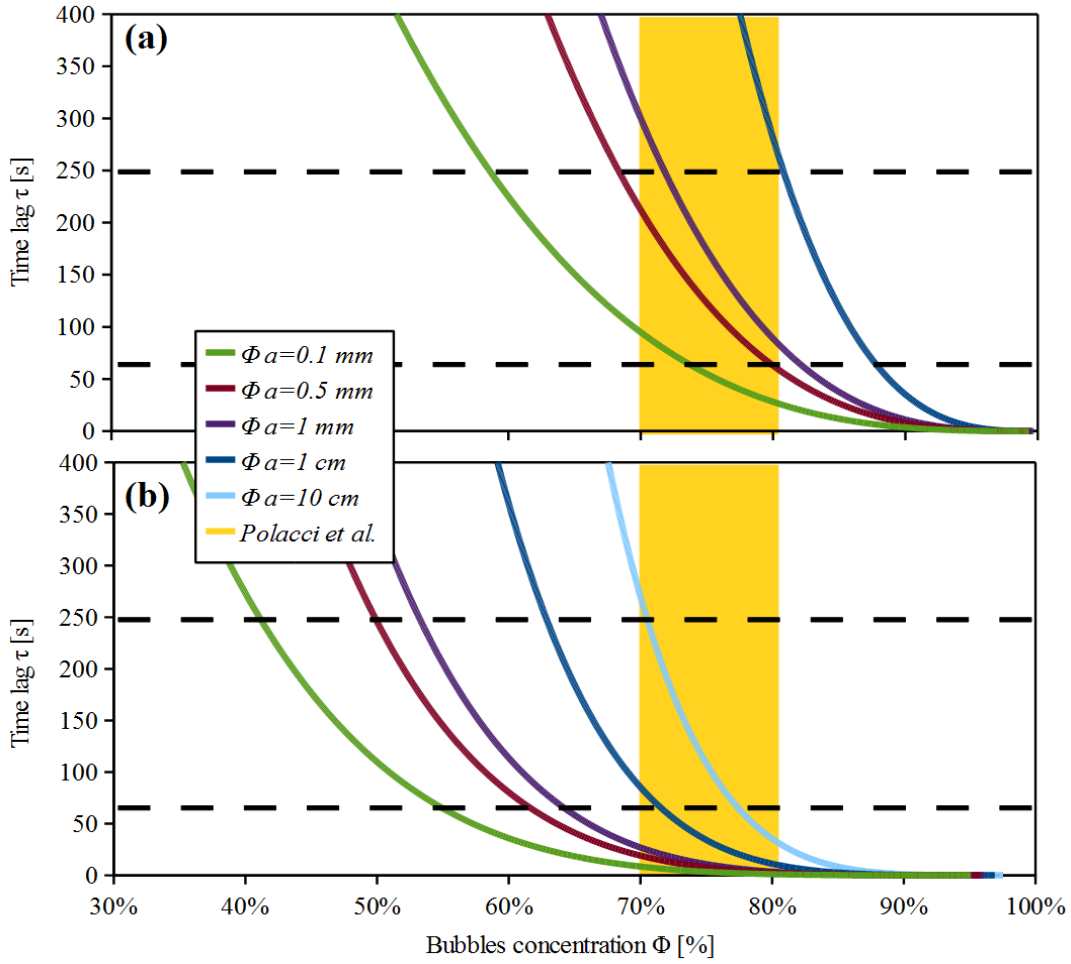

Figure 73: Graphs (a) and (b) show calculated τ(Φ) functions calculated from equations 16-19 for different bubble radius and for n values of 3 (a) and 5 (b) respectively.

Periodic SO_2 puffing behaviour at Etna (and, possibly, other volcanoes) may thus reflect (and depend on) the presence of a sequence of individual bubble layers (having time-changing rising speeds) in a volcanic conduit. Surface bursting of each such gas bubble layers would lead to emission of single gas puff, while periodicity in gas emissions would be the ultimate result of rhythmic release of (more or less regularly spaced) layers. In this case, three possible considerations (discussed below) may be relevant to the development of gas flux patterns (i) to (iii), mentioned above (see Fig. 65 and related discussion):

- A constant puffing rate, as reflected by pattern (i) in Fig. 65a, would be produced by ascent in the conduit of waves of constantly spaces bubble layers (wavelength λ is constant; Manga, 1996; Ripepe et al., 2002);
- The spacing of bubble layers, and consequently the time lag in between their arrival , can fluctuate over time, to produce structures as shown in Fig. 65 and 67, and ultimately gas pattern (ii);
- The conduit's structuring into trains of bubble layers can eventually become disrupted (e.g., when liquid convection becomes more vigorous or rapidly slows down, or because bubble concentration in the interlayers increases, leading to a generally bubbling regime; Divoux et al., 2009; Fig. 65c), ultimately giving rise to periods when puffing activity (e.g., periodic SO_2 release) disappears (gas pattern (iii) above).

5.4.6 Conclusions

Mount Etna is one of the most extensively studied volcanoes in the world. Investigating the volcano's long-term SO_2 flux behaviour has led to important conclusions to be drawn on the structure of the magma feeding system, magma production (and degassing) rates, and causes for the excess degassing behaviour (Allard et al., 2006). Nonetheless, our knowledge of the short-term (timescales of seconds to a few hours) behaviour of magmatic volatiles (e.g., bubble coalescence, separate ascent and surface bursting of gas-rich bubbles) in the upper feeding conduits of volcanoes primarily steams from indirect evidences, such as petrologic-textural

data (e.g., Rust et al., 2004), observation of geophysical signals (Chouet, 2003), physical modelling (Gonnermann and Manga, 2003; Sparks, 2003) and laboratory experiments (Divoux et al., 2009). In the past direct gas flux measurements have involved insufficient temporal resolution for fast conduit processes to be investigated.

UV cameras now allow imaging of gas flux emissions, and exploration of underlying volcanic degassing processes, with an improved temporal resolution. In this *section*, we have shown that the UV camera can valuably assist in capturing the rapid (timescale of seconds) SO_2 flux variations occurring during the quiescent activity of a basaltic volcano. We have, in particular, investigated the non-stationary nature of degassing activity at Etna's North-east crater, which is shown here to exhibit a somewhat periodic degassing behaviour (characteristic periods ranging 40-250 s). A similar degassing behaviour has recently been observed at other volcanoes (Stromboli, see *section* 5.3; Erebus, Boichu et al., 2010; San Cristóbal, Galle et al., 2010), and probably represents a common feature of all basaltic volcanoes. We have finally presented a preliminary model indicating that this periodic degassing pattern may reflect inhomogeneous distribution of gas bubbles in a magmatic conduit, and their clustering to form trains of variably spaced gas bubble layers.

Chapter 6
Conclusions

Degassing is among the most evident expressions of active volcanism, and acts to couple the Earth's interior and surface environments. Passive degassing, the continuous quiescent emission of gases and particles from a volcano summit, frequently coexists with non-passive degassing forms, e.g. discharge of over-pressurized gas as bursts or puffs. While both degassing modes have intensively been investigated in the past, the low temporal resolution of traditional gas measurement techniques has hampered the characterization of the short-term (seconds to minutes) structure of gas flux time series, and exploration of transient volcanic phenomena (e.g., Strombolian explosions).

In this study, I have reported on an updated UV camera configuration, which can be used to image volcanic SO_2 release to the atmosphere with high temporal resolution. This dual-UV camera configuration combines relatively high frequency

measurements (1.2- 0.5 Hz) with improved accuracy, at least relative to measurements taken with only one filter at a time. I have also proposed a number of calibration procedures, showing that in tandem DOAS-UV camera observations may likely result in more efficient calibration and higher flexibility in automation. I also developed novel software, which can manage all the different aspects of data acquisition and post-processing.

In order to test the validity and versatility of the instrument in volcanological applications, the developed UV camera set-up was deployed in the field during numerous measurements campaigns on three Italian volcanoes, which exhibit different forms of degassing: La Fossa crater (Vulcano), Stromboli and Etna.

La Fossa crater is characterized by a 0.045 km^2 fumarolic field, which covers the northern rim and part of the inner crater. The fumarole chemical composition varies considerably in time and space, ranging from magmatic to hydrothermal compositional end-members. While the total SO_2 flux from La Fossa has been characterised many time before, the relative contribution of the different fumaroles to the total gas budget has been largely unconstrained. Here, I have reported the first SO_2 gas flux measurement from La Fossa's individual fumaroles, and probably one of the first in depth characterisations of multiple-source emissions from a fumarolic field. The UV camera-derived individual fumarole SO_2 fluxes have been used in tandem with MultiGAS-derived gas/SO_2 molar ratios for a number of fumaroles, which allowed me to accurately assess CO_2, H_2O, and H_2S fluxes, and thus to refine previous gas inventories for the volcano. I report on two data-sets, taken during (November 2009) and after (February 2010) a degassing/heating unrest event on La Fossa crater. Our results clearly show that there was a factor ~2 increase in CO_2 and H_2O degassing during the la Fossa crater degassing/heating unrest. In contrast, the total H_2S flux, a hydrothermally derived gas component, was apparently not affected by the heating event. Overall, our observations here support further the idea that recurrent heating unrests on La Fossa fumarolic field reflect an enhanced rate of hot (deep rising) gas transport to the surface. I also confirm that the central conduit system feeding the fumaroles is the main gas transfer pathway (relative to soil degassing). This in-tandem

UV camera/MultiGAS observation is an innovative observational strategy, which may contribute to improved understanding of degassing processes, and eventually to volcanic hazard assessment.

On Stromboli, I have reported here on the first field attempt to simultaneously estimate the SO_2 flux release from the three main forms of degassing (passive degassing, strombolian explosions, and puffing). Using the UV camera system, I evaluated the SO_2 mass output for 147 strombolian explosions, and concluded that explosive degassing contributes to 7±1.5 % of the total SO_2 flux. The obtained high frequency SO_2 flux time-series also demonstrate that Stromboli is characterized by a cyclic SO_2 degassing pattern over timescales of minutes, modulated by the periodic Strombolian explosions. This may lead to re-evaluation of the relation between passive and active degassing at other volcanoes as well. I have also reported on the first direct measurements of the SO_2 mass contributed by individual gas puffs (ranging 0.03-0.45 kg), and shown that puffing contributes to < 10 % of the total SO_2 flux (far less than previously suggested by indirect geophysical evaluations, ~ 50%). From their estimated total gas mass (~5 kg), I argue that each individual gas puff is generated by top-of-the conduit bursting of a gas bubble of ~ 0.32 m radius, likely produced by gas coalescence in the top few meters of the magmatic column.

Integration of SO_2 time series with geophysical data has allowed derivation of information on the mechanisms governing Strombolian explosions. A positive correlation between the VLP seismic signal amplitude of each individual explosion (associated with generation and ascent of a gas slug within the upper conduit) and its corresponding syn-explosive SO_2 mass was observed. During an explosion, the SO_2 flux is shown to systematically peak during the deflation phase of the conduit, as indicated by a characteristic waveform of the VLP pulse. This suggests that the VLP signal is inextricably connected not only with the in-conduit eruption trigger, but also (perhaps even primarily) with the dynamics of syn-explosive gas release at the top of the magmatic column. Comparison with thermal imagery data demonstrates, instead, a nearly synchronous (± 1.2 s) emission of gas and hot pyroclasts during the explosions,

and highlights a difference between ash-free and ash-dominated explosions, related to the higher emissivity of the ash relative to coarse pyroclastic materials.

The pulsate emission of highly concentrated SO_2 clouds from the North-east crater of Mount Etna has been observed by scientists since the first in-situ sampling of the fumaroles , and represents an evident case of non-stationary passive degassing from a quiescent volcano. While Mount Etna is among the best well studied volcanoes on the planet, the source mechanisms governing this periodic degassing have remained unexplored, however. During two campaigns on Pizzi Dineri (northern rim of Valle del Bove, Etna), we took UV camera gas flux measurements targeting the North-east crater degassing dynamics. The acquired SO_2 time series demonstrate that Etna's North-east crater exhibits a periodic degassing behaviour with characteristic periods ranging 60-250 s. This may reflect an inhomogeneous distribution of gas bubbles in the magmatic conduit, and their clustering to form trains of variably spaced bubbly layers. To acquire similar data elsewhere, and verify whether periodic degassing is a general feature of open-vent volcanoes is now possible with UV camera, and more timely than ever before.

This study shows the importance of high time-resolution SO_2 flux measurements for better understanding of volcanic degassing. The dual-UV camera system, coupled with DOAS, stands as a powerful instrument for gas emission monitoring, is relatively cheap and simple to use (deployment in <2 minutes). Development of new user-friendly software will facilitate dissemination of the technique to an even larger number of volcanologists in the future. The software developed here, *Vulcamera,* has been tested over the last two years for the acquisition and data real-time/post processing, demonstrating easy and fast usage. During our campaigns, we have collected more than 24 hours of flux data on Vulcano, Stromboli and Etna, under a variety of ambient and plume conditions; and obtained a inter-comparison with geophysical data which, if pursued further in the future, promises to reveal novel and highly significant aspects of volcanic processes. A significant conclusion obtained here is that, despite the coexistence of different modes of gas

release at any given volcano, passive degassing still remains the primary mechanism of gas exhaustion. Yet, such a passive gas release is here clearly shown to be characterized by periodic fluctuations of variable magnitude and time-scales (from seconds to hours), which are potentially common to most open-vent volcanoes, and are now probably telling us a far more interesting and insightful story than we have learnt of so far.

References

A

Aggarwal, M., Hua, H., Ahuja, N., (2001). *On cosine-fourth and vignetting effects in real lenses.* 8th International Conference on Computer Vision, 2001, vol.1, 472-479

Allard, P., Carbonelle, J., Métrich, N., Loyer, H., Zettwoog, P., (1994). *Sulphur output and magma degassing budget of Stromboli volcano.* Nature, 368, 326-330.

Allard, P., (1997). *Endogenous magma degassing and storage at Mount Etna.* Geophys. Res. Lett., 24, 2219-2222, 1997.

Allard, P., Burton, M., Murè, F., (2004). *Spectroscopic evidence for a lava fountain driven by previously accumulated magmatic gas.* Nature 433, 407-410 doi:10.1038/nature03246

Allard, P., Aiuppa, A., Burton, M., Caltabiano, T., Federico, C., Salerno, G., La Spina, A., (2008). Crater gas emissions and the magma feeding system of Stromboli volcano. In: Calvari, S., Inguaggiato, S., Puglisi, G., Ripepe, M., Rosi, M. (Eds.), Learning from Stromboli: AGU Geophysics Monograph Series, 182, pp. 65–80. Washington DC

Aiuppa, A., Federico, C., Giudice, G., Gurrieri, S., (2005a). *Chemical mapping of a fumarolic field: La Fossa Crater, Vulcano Island (Aeolian Islands, Italy)*. Geophysical Research Letters. 32: L13309.

Aiuppa, A., Inguaggiato, S., McGonigle, A., O'Dwyer, M., Oppenheimer, C., Padgett, M., Rouwet, D. & Valenza, M., (2005b). *H_2S fluxes from Mt. Etna, Stromboli, and Vulcano (Italy) and implications for the sulfur budget at volcanoes*. Geochimica et Cosmochimica Acta. Elsevier Science. 69:1861-1871

Aiuppa, A., Federico, C., Giudice, G., Gurrieri, S., Valenza, M., (2006a). *Hydrothermal buffering of the SO2/H2S ratio in volcanic gases: Evidence from La Fossa Crater fumarolic field, Vulcano Island*. Geophysical Research Letters. DOI: 10.1029/2006GL027730.

Aiuppa, A., Federico, C., Giudice, G., Gurrieri, S., Liuzzo, M., Shinohara, H., Favara, R. , Valenza, M., (2006b). *Rates of carbon dioxide plume degassing from Mount Etna volcano*. Journal of Geophysical Research. DOI:10.1029/2006JB004307.

Aiuppa, A., Moretti, R., Federico, C., Giudice, G., Gurrieri, S., Liuzzo, M., Papale, P., Shinohara, H., Valenza, M., (2007). *Forecasting Etna eruption by real time evaluation of volcanic gas composition*. Geology 35 (12), 1115–1118 doi:10.1130/G24149A.

Aiuppa, A., Burton, M., Allard, P., Caltabiano, T., Giudice, G., Gurrieri, S., Liuzzo, M., Salerno, G., (2011). *First experimental evidence for the CO_2-driven origin of Stromboli's major explosions*. Solid Earh Discuss, 3, 411-430, doi:10.5194/sed-3-411-2011

Andres, R.J., Kasgnoc, A.D., (1998). *A time-averaged inventory of subaerial volcanic sulfur emissions*. J. Geophys. Res. 103, 25251–25261.

B

Blackburn, E.A., Wilson, L., Sparks, R.S.J., (1976). *Mechanisms and dynamics of strombolian activity*. J. Geol. Soc. London, 132:429-440.

Bluth, G.S.J., Shannon, J.M., Watson, I.M., Prata, A.J., Realmuto, V.J. (2007). *Development of an ultra-violet digital camera for volcanic SO_2 imaging*. J. Volcanol. Geotherm. Res., 161, 47-56.

Bobrowski, N., Hönninger, G., Lohberger, F., and U. Platt (2006). *IDOAS: A new monitoring technique to study the 2D distribution of volcanic gas emissions*. J. Volcanology and Geothermal Res., 150, 329-338.

Boichu, M., Oppenheimer, C., Tsanev, V., Kyle, P.R., (2010). *High temporal resolution SO2 flux measurements at Erebus volcano, Antarctica*. J. Volcanol. Geotherm. Res., 190, 325-336.

Burton, M., Allard, P., Murè, F., La Spina, A., (2007a). *Magmatic gas composition reveals the source depth of slug-driven Strombolian explosive activity*. Science, 317, 227-230.

Burton, M., Mader, H.M., Polacci, M. (2007b). *The role of gas percolation in quiescent degassing of persistently active basaltic volcanoes*. Earth Planet. Sci. Lett., 264, 46-60.

Burton, M., Caltabiano, T., Murè, F., Salerno, G., Randazzo, D. (2009). *SO_2 flux from Stromboli during the 2007 eruption: results from the FLAME network and traverse measurements*. J. Volcanol. Geotherm. Res., 182, 214-220.

C

Caltabiano, T., Romano, R., Budetta, G., (1994). *SO_2 flux measurements at Mount Etna (Sicily)*. J. Geophys. Res. 99 (12), 809–12,819

Caltabiano, T., Burton, M., Giammanco, S., Allard, P., Bruno, N., Murè, F., Romano, R., (2004). *Volcanic gas emissions from the summit craters and flanks of Mt. Etna, 1987-2000*. Mt. Etna: Volcano laboratory.

Cannata, A., Montalto, P., Privitera, E., Russo, G. and Gresta, S. (2009a). *Tracking eruptive phenomena by infrasound: May 13, 2008 eruption at Mt. Etna*. Geophys. Res. Lett., 36, L05304, doi: 10.1029/2008GL036738.

Carroll, M.R., Holloway, J.R. (Eds.), (1994). *Volatiles in magmas*. Reviews of Mineralogy, p. 30.

Carroll, M.R., Webster, J.D., (1994). *Solubilities of sulfur, noble gases, nitrogen, chlorine, and fluorine in magmas*. In: Carroll, M.R., Holloway, J.R. (Eds.), Rev. in Mineral. 30, American Mineralogical Society,. pp. 231-279.

Casadevall, T.J., Stokes, J.B., Greenland, L.P., Malinconico, L.L., Casadevall, J.R., Furukawa, B.T. (1987). *SO_2 and CO_2 emission rates at Kilauea Volcano, 1979–1984*. In: Decker RW, Wright TL, Stauffer PH (eds) Volcanism in Hawaii. US Geol Surv Prof Paper, pp 771–780

Chouet, B., Hamisevicz, B., McGetchin, T.R. (1974). *Photoballistics of volcanic jet activity at Stromboli*. Italy. J. Geophys. Res., 79, 4961–4976.

Chouet, B., (1992). *A seismic model for the source of long-period events and harmonic tremor.* in Volcanic Seismology, edited by P. Gasparini, R. Scarpa, and K. Aki, 133-156, Springer, New York.

Chouet, B., Saccorotti, G., Dawson, P., Martini, M., Scarpa, R., De Luca, G., Milana, G., Cattaneo, M., (1999). *Broadband measurements of the sources of explosions at Stromboli volcano*. Italy. Geophys. Res. Lett., 28, 1937-1940.

Chouet, B., Dawson, P., Ohminato, T., Martini, M., Saccorotti, G., Giudicepietro, F., De Luca, G., Milana, G., Scarpa, R. (2003). *Source mechanism of explosions at Stromboli Volcano, Italy, determined from moment-tensor inversions of very-long-period data*. J. Geophys. Res., 108 (B1), 2019. doi:10.1029/2002JB001919.

Chiodini,G., Frondini, F., Raco, B., 1996. *Diffuse emission of CO2 from the Fossa crater, Vulcano Island (Italy)*. Bulletin of Volcanology. 58:41-50.

Chiodini, G., Granieri, D., Avino, R., Caliro, S., Costa, A., Werner, C., (2005). *Carbon dioxide diffuse degassing and estimation of heat release from volcanic and hydrothermal systems*. Journal of geophysical research. B, Solid planets. DOI:10.1029/2004JB003542.

D

Daag, A.S., Tubianosa, B.S., Newhall, C.G., Tungol, N.M., Javier, D., Dolan, M.T., Delos Reyes, P.J., Arboleda, R.A., Martinez, M.L., Regalado, T.M. (1996).

Monitoring sulfur dioxide emission at Mount Pinatubo. In: *Fire and mud: eruptions and lahars of Mount Pinatubo Philippines*. Newhall CG, Punongbayan RS (eds), Philippine Institute of Volcanology and Seismology, Quezon City, and University of Washington Press, Seattle. P *409-434*

Delmelle, P., Delfosse, T., Delvaux, B. (2003). *Sulfate, chloride and fluoride retention in Andosols exposed to volcanic acid emissions*. Environ Pollut 126:445-457.

Dalton, M., Watson, I., Nadeau, P., Werner, C., Morrow, W., Shannon, J., (2009). *Assessment of the UV camera sulfur dioxide retrieval for point source plumes.* J. Volcanol. Geotherm. Res., 188, 358–366.

Dalton, M., Waite, G.P., Watson, I. M., Nadeau, P., (2010). *Multiparameter quantification of gas release during weak Strombolian eruptions at Pacaya Volcano, Guatemala*. Geophys. Res. Lett., VOL. 37, L09303, doi:10.1029/2010GL042617, 2010

Doukas, M.P. (2002). *A new method for GPS-based wind speed determinations during airborne volcanic plume measurements*. US Geol Surv Open-File Rep 02–395, pp 13

E

Edmonds, M., R. A. Herd, B. Galle, and C. M. Oppenheimer (2003). *Automated, high time resolution measurements of SO_2 flux at Soufriére Hills Volcano, Montserrat*. Bull. Volcanol., 65, 578–586, doi:10.1007/s00445-003-0286-x.

Elias, A.J., Sutton, J.B., Stokes and T.J. Casadevall (1988). *Sulphur dioxide emission rates of Kilauea volcano, Hawaií, 1979–1997*. Open File Report 98-462. U.S. Geol. Surv (1988) http://hvo.wr.usgs.gov/products/OF98462.

G

Galle, B., Oppenheimer, C., Geyer, A., McGonigle, A.J.S., Edmonds, M., Horrocks, L.A., (2003). *A miniaturised UV spectrometer for remote sensing of SO_2 fluxes: a new tool for volcano surveillance*. J. Volcanol. Geotherm. Res. 119, 241–254.

Galle, B., Platt, U., Oppenheimer, C., Millan, M., Alonso, L., Chen, D. (2006). *Final scientific report on EU-Project DORSIVA*. Rep. 26051, Chalmers Univ. of Technol., Gothenburg, Sweden.

Galle, B., Johansson, M., Rivera, C., Zhang, Y., Kihlman, M., Kern, C., Lehmann, T.,Platt, U., Arellano, S., Hidalgo, S., (2010). *Network for Observation of Volcanic and Atmospheric Change (NOVAC)—A global network for volcanic gas monitoring: Network layout and instrument description*. J. Geophys. Res., 115, D05304, doi:10.1029/2009JD011823.

Giggenbach W. F., (1987). *Redox processes governing the chemistry of fumarolic gas discharges from White Island, New Zealand*. Applied Geochemistry, 2, 143 161.

Giggenbach, W. F., (1996). *Chemical Composition of Volcanic Gases*. Monitoring and Mitigation of Volcanic Hazards. 221–256.

Giggenbach, W.F. (1997). *The origin and evolution of fluids in magmatic-hydrothermal systems*. In: Geochemistry of Hydrothermal Ore Deposits. 3rd Edition. Barnes HL (ed) Wiley, New York, NY, USA. P 737-796

Graf, H.F., Feichter, J., Langmann, B. (1997). *Volcanic sulfur emissions: Estimates of source strength and its contribution to the global sulfate distribution*. J Geophys Res 102:10,727-10,738

H

Harris, A.J.L., Stevenson, D.S., (1997). *Magma budgets and steady-state activity of Vulcano and Stromboli volcanoes*. Geophys. Res. Lett. 24, 1043–1046

Harris, A. and Ripepe, M. (2007), *Temperature an dynamics of degassing at Stromboli*, J. Geophys. Res., 112, doi:10.1029/2006JB004393.

Hirabayashi, J., Ohba, T., Nogami, K., Yoshida, M., (1995). *Discharge rate of SO_2 from Unzen Volcano, Kyushu, Japan*. Geophys. Res. Lett. 22, 1709–1712.

Hoff, R.M. (1992). *Differential SO_2 column measurements of the Mt. Pinatubo volcanic plume*. Geophys Res Lett 19:175-178

Holland, P.A.S., Watson, M.I., Phillips, J.C., Caricchi, L., Dalton, M.P., (2011). *Degassing processes during lava dome growth: Insights from Santiaguito lava dome, Guatemala*. J. Volcanol. Geotherm. Res., 202, 153-166.

Horton, K.A., Williams-Jones, G., Garbeil, H., Elias, T., Sutton, A.J., Mouginis-Mark, P., Porter, J.N., Clegg, S., (2006). *Real-time measurement of volcanic SO_2 emissions: validation of a new UV correlation spectrometer (FLYSPEC)*. Bull.Volcanol. 68, 323–327.

I

Italiano, F., Pecoraino, G., Nuccio, P. M., (1998). *Steam output from fumaroles of an active volcano: Tectonic and magmatic-hydrothermal controls on the degassing system at Vulcano (Aeolian arc)*. Journal of Geophysical Research Letters. 103:29829-29842.

J

Jaupart, C., Vergniolle, S., (1988). *Laboratory models of Hawaiian and Strombolian eruptions*. Nature 331:58-60.

Johansson, M. (2008). *Geometrical errors in flux measurements using the NOVAC scanning DOAS instrument*. Paper presented at Fourth International DOAS Workshop, Accent Project, Hefei, China.

K

Kantzas, E.P., McGonigle, A.J.S., Bryant, R.G., (2009). *Comparison of low cost miniature spectrometers for volcanic SO_2 emission measurements*. Sensors 9, 3256–3268. doi:10.3390/s90503256.

Kantzas, E.P., McGonigle, A.J.S., Tamburello, G., Aiuppa, A., Bryant, R. G. (2010). *Protocols for UV camera volcanic SO_2 mesurements*. J. Volcanol. Geotherm. Res., 194, 55-60, doi:10.1016/j.jvolgeores.2010.05.003.

Kantzas, E.P., McGonigle, A.J.S., Tamburello, G., Bryant, R. G. (2011). *UVolc: A software platform for measuring volcanic SO_2 fluxes*. Computer & Geosciences, doi:10.1016/j.cageo.2011.07.011.

Kazahaya, R., Mori, T., Takeo, M., Ohminato, T., Urabe, T., Maeda, Y., (2011). *Relation between single very-long-period pulses and volcanic gas emissions at Mt. Asama, Japan*. 38, L11307, doi:10.1029/2011GL047555

Kern, C., Deutschmann, T., Vogel, L., Wöhrbach, M., Wagner, T., Platt, U. (2009). *Radiative transfer corrections for accurate spectroscopic mesurements of volcanic gas emissions*. Bull. Volcanol., doi:10.1007/s00445-009-0313-7.

Koepenick, K. W., Brantley, S. L., Thompson, J. M., Rowe, G. L., Nyblade, A. A., Moshy, C., (1996). *Volatile emissions from the crater and flank of Oldoinyo Lengai volcano, Tanzania*. Journal of Geophysical Research Letters, 13:819-830.

Kyle, P.R., Sybeldon, L.M., McIntosh, W.C., Meeker, K., Symonds, R. (1994). *Sulfur dioxide emission rates from Mount Erebus, Antarctica*. In: Kyle PR (ed) Volcanological and environmental studies of Mount Erebus, Antarctica. American Geophysical Union, Washington, D.C., pp 69–82

M

Macdonald, G.A. (1972). *Volcanoes*. Prentice-Hall. Englewood Cliffs, NJ.

Manga, M. (1996). *Waves of bubbles in basaltic magmas and lavas.* J. Geophys. Res., 101, 17457-17465.

McGonigle, A.J.S.,Oppenheimer, C., Galle, B., Mather, T.A., Pyle, D.M., (2002). *Walking traverse and scanning DOAS measurements of volcanic gas emission rates*. Geophys. Res. Lett. 29, 1985.

McGonigle, A. J. S., and Oppenheimer, C. (2003). *Optical sensing of volcanic gas and aerosol emissions*. in Volcanic Degassing, edited by C. Oppenheimer, D. M. Pyle, and J. Barclay, Geol. Soc. Spec. Publ., 213, 149 – 168.

McGonigle, A.J.S. (2005a). *Volcano remote sensing with ground-based spectroscopy.* Phil. Trans. R. Soc. A, 363, 2915–2929 doi:10.1098/rsta.2005.1668

McGonigle, A.J.S., Inguaggiato, S., Aiuppa, A., Hayes, A.R., Oppenheimer, C., (2005b). *Accurate measurement of volcanic SO_2 flux: determination of plume transport speed and integrated SO_2 concentration with a single device*. Geophys., Geochem., Geosyst. 6, Q02003.

McGonigle, A. J. S. (2007). *Measurement of volcanic SO_2 fluxes with differential optical absorption spectroscopy*. J. Volcanol. Geotherm. Res., 162, 111– 122, doi:10.1016/j.jvolgeores.2007.02.001.

McGonigle, A. J. S., Aiuppa, A., Giudice, G., Tamburello, G., Hodson, A. J., Gurrieri, S., (2008). *Unmanned aerial vehicle measurements of volcanic carbon dioxide fluxes*. Geophysical Research Letters. DOI:10.1029/2007GL032508.

McGonigle, A.J.S., Aiuppa, A., Ripepe, M., Kantzas, E.P., Tamburello, G. (2009). *Spectroscopic capture of 1 Hz volcanic SO_2 fluxes and integration with volcano geophysical data*. Geophys. Res. Lett., 36, L21309, doi:10.1029/2009GL040494.

Métrich, N., Rutherford, M.J., (1998). *Low pressure crystallization paths of H_2O-saturated basaltic-hawaiitic melts from Mt. Etna: implications for open-system degassing of basaltic volcanoes*. Geochim. Cosmochim. Acta 62, 1195–1205.

Métrich, N., Bertagnini, A., Landi, P., Rosi, M., (2001). *Crystallization driven by decompression and water loss at Stromboli volcano (Aeolian Islands, Italy)*. J. Petrol. 42, 1471–1490.

Métrich N, Mandeville C.W. (2010). *Sulfur in magmas*. Elements 6:81-86

Métrich, N., Bertagnini, A., Di Muro, A., (2010). *Conditions of Magma Storage, Degassing and Ascent at Stromboli: New Insights into the Volcano Plumbing System with Inference on the Eruptive Dynamics*. J. Petrol. 51/3, 603-626.

Millan, M.M., (1980). *Remote sensing of air pollutants: a study of some atmospheric scattering effects*. Atmos. Environ. 14,1241-1253.

Moffat, A.J., Millan, M.M., (1971). *The application of optical correlation techniques to the remote sensing of SO_2 plumes using skylight*. Atmos. Environ. 5, 677^690.

Mori, T. and Burton, M. (2006). *The SO_2 camera: a simple, fast and cheap method for ground-based imaging of SO_2 in volcanic plumes*. Geophys. Res. Lett., 33, L24804, doi:10.1029/2006GL027916.

Mori, T. and Burton, M. (2009). *Quantification of the gas mass emitted during single explosions on Stromboli with the SO_2 imaging camera*. J. Volcanol. Geotherm. Res., 188, 395-400, doi:10.1016/j.jvolgeores.2009.10.005.

N

Nadeau, P.A., José, L.P., Waite, G.P., (2011). *Linking volcanic tremor, degassing, and eruption dynamics via SO_2 imaging*. Geophys. Res. Lett., 38, L01304, doi:10.1029/2010GL045820

Neri, M., Mazzarini, F., Tarquini, S., Bisson, M., Isola, I., Behncke, B., Pareschi, M.T., (2008). *The changing face of Mount Etna's summit area documented with lidar technology.* Geophys. Res. Lett., 35, L09305,doi:10.1029/2008GL033740.

Nuccio, P. M., Paonita, A., (2001). *Magmatic degassing of multicomponent vapors and assessment of magma depth: application to Vulcano Island (Italy)*. Earth and Planetary Science Letters. 193:467-481

O

Olmos, R., et al. (2007). *Anomalous emissions of SO_2 during the recent eruption of Santa Ana volcano, El Salvador, Central America*. Pure Appl. Geophys., 164(12), 2489– 2506.

Oppenheimer, C. (2003). *Volcanic degassing*. In: Holland, H., Turekian, K. (Eds.), The crust, Treatise on Geochemistry, vol. 3. Elsevier-Pergamon, Oxford, pp. 123–166. Ch. 3.04.

Oppenheimer, C., Scaillet, B., Martin, R.S., (2011). *Sulfur Degassing From Volcanoes: Source Conditions, Surveillance, Plume Chemistry and Earth System Impacts*. Reviews in Mineralogy & Geochemistry, Vol. 73 pp. 363-421, 2011, Copyright c Mineralogical Society of America

Oppenheimer, C., (2010). *Ultraviolet sensing of volcanic sulfur emissions*. Elements, 6, 87–92.

P

Parfitt, E.A., Wilson, L., (1995). *Explosive volcanic eruptions-IX. The transition between the Hawaiian-style lava fountaining and Strombolian explosive activity.* Geophys. J. Int., 121, 226-232, doi:10.1111/j.1365-246X.1995.tb03523.x.

Parfitt, E.A., (2004). *A discussion of the mechanisms of explosive basaltic eruptions*. J. Volcanol. Geotherm. Res. 134, 77-107.

Patrick, M., Harris, A.J.L., Dehn, J., Ripepe, M., Rothery, D. A., Calvari, S. (2007). *Strombolian explosive styles and source conditions: Insights from thermal video (FLIR) imagery*. Bull. Volcanol., 69, 769-784, doi:10.1007/s00445-006-0107-0.

Polacci, M., Baker, D.R., Mancini, L., Favretto, S., Jill, R.J., (2009). *Vesiculation in magmas from Stromboli and implications for normal Strombolian activity and paroxysmal explosions in basaltic systems*. J. Geophys. Res., 114, B01206, doi:10.1029/2008JB005672.

R

Ripepe, M., Ross, M., Saccorotti, G., (1993). *Image processing of explosive activity at Stromboli*. J. Volcanol. Geotherm. Res., 54, 335-351.

Ripepe, M. and Gordeev, E. (1999). *Gas bubble dynamics model for shallow volcanic tremor at Stromboli*. J. Geophys. Res., 104 (B5), 10639-10654.

Ripepe, M., Ciliberto, S., Della Schiava, (2001). *Time constraints for modelling source dynamics of volcanic explosions at Stromboli*. J. Geophys. Res., 106 (B5), 8713-8727.

Ripepe, M., Harris, A.J.L., Carniel, R. (2002). *Thermal, seismic and infrasonic evidences of variable degassing rates at Stromboli volcano.* J. Volcanol. Geotherm. Res., 118, 285-297.

Ripepe, M. and Marchetti, E. (2002). *Array tracking of infrasonic sources at Stromboli volcano.* Geophys. Res. Lett., 29 (22), 2076, doi:10.1029/2002GL015452.

Ripepe, M., Delle Donne, D., Harris, A., Marchetti, E., Ulivieri, G., (2008). *Dynamics of Stromboli activity.* In: Calvari, S., Inguaggiato, S., Puglisi, G., Ripepe, M.,

Rosi, M. (Eds.), Learning from Stromboli: AGU Geophysics Monograph Series, 182, pp. 39-48. Washington DC.

Ripepe, M., Delle Donne, D., Lacanna, G., Marchetti, E., Ulivieri G. (2009). *The onset of the 2007 Stromboli effusive eruptions recorded by an integrated geophysical network*. J. Volcanol. Geotherm. Res., 182, 131-136, doi:10.1016/j.jvolgeores.2009.02.01

Robock, A., (2002). *Pinatubo eruption: The climatic aftermath*. Science, 295, 1242-1244.

Robock, A., and Oppenheimer, C. (editors), (2003). *Volcanism and the Earth's atmosphere*. American Geophysical Union, Geophysical Monograph, 139, 360pp.

S

Salerno, G., M. Burton, T. Caltabiano, B. N. Bruno, D. Condarelli, L. V. Longo, and M. F. Murè (2006). *High-term resolution SO_2 flux measurements using an automated UV scanner array: First 16-month results on Mt. Etna (Italy).* Geophys. Res. Abstr., 8, Abstract EGU06-A-03098.

Salerno, G., M. Burton, C. Oppenheimer, T. Caltabiano, D. Randazzo, N. Bruno, and V. Longo (2009). *Three-years of SO_2 flux measurements of Mt. Etna using an automated UV scanner array: Comparison with conventional traverses and uncertainties in flux retrieval.* J. Volcanol. Geotherm. Res., 183, 76–83.

Shinohara, H., (2005). A *new technique to estimate volcanic gas composition: plume measurements with a portable multi-sensor system*. Journal of Volcanology and Geothermal Research. 143:319-333.

Shinohara, H. (2008). *Excess degassing from volcanoes and its role on eruptive and intrusive activity.* Rev. Geophys., 46 doi:10.1029/2007RG000244 RG4005.

Sparks, R.S.J. (2003). *Dynamics of magma degassing*. Geological Society, London, Special Publications, 213, 5-22.

Spilliaert, N., Métrich, N., Allard, P., (2006). *S– Cl–F degassing pattern of water-rich alkali basalt: Modelling and relationship with eruption styles on Mount Etna volcano*. Earth Planet. Sci. Lett. 248, 772–786.

Stevenson, D.S., Blake, S., (1998). *Modelling the dynamics and thermodynamics of volcanic degassing*. Bull. Volcanol. 60, 307–317.

Stoiber, R. E., Malinconico, L. L. & Williams, S. N. (1983). *Use of the correlation spectrometer at volcanoes*. In Forecasting volcanic events (ed. H. Tazieff & J. C. Sabroux), pp. 425–444. Amsterdam: Elsevier.

Symonds, R. B., Rose, W. I., Bluth, G. J. S. & Gerlach, T. M. (1994). *Volcanic gas studies—methods, results, and applications*. Rev. Mineral. 30, 1–66.

T

Tamburello, G. Kantzas, E.P., McGonigle A.J.S., Aiuppa, A., Giudice, G., (2010). *UV camera measurements of fumarole field degassing (La Fossa crater, Vulcano,*

Island). J. Volcanol. Geotherm. Res., 199, 47-52, doi:10.1016/j.jvolgeores.2010.10.004

Tamburello, G., Kantzas, E.P., McGonigle, A.J.S., Aiuppa, A., (2011a). *Recent advances in ground-based ultraviolet remote sensing of volcanic SO_2 fluxes*,. Annals of Geophysics, 54, 2, 199-208; doi: 10.4401/ag-5179

Tamburello, G., Kantzas, E.P., McGonigle, A.J.S., Aiuppa, A., (2011b). *Vulcamera: a program for measuring volcanic SO_2 using UV cameras*. Annals of Geophysics, 54, 2, 219-221; doi: 10.4401/ag-518

V

Vandaele, A., Simon, P., Guilmot, G., Carleer, M., Colin, R., (1994) *SO_2 absorption cross section measurement in the UV using a Fourier transform spectrometer.* J. Geophys. Res., 99, 25,599-25,605

Vergniolle, S., Brandeis, G., (1996). *Strombolian explosion: A large bubble breaking at the surface of a lava column as a source of sound*. J. Geophys. Res., 101 (B09), 20,433–20,448.

Vidal, V., Géminard, J.C., Divoux, T., Melo, F., (2006). *Acoustic signal associated with the bursting of a soap film which initially closes an overpressurized cavity.* Eur. Phys. J. B., 54, 321-339, doi:10.1140/epjb/e2006-00450-0

Vidal V., Ripepe, M., Divoux, T., Legrand, D., Géminard, J.C., Melo, F. (2010). Dynamics of soap film bursting and its implications to volcano acoustics. Geophys. Res. Lett. 37, L07302

W

Wallace, P.J. (2005). *Volatiles in subduction zone magmas: concentrations and fluxes based on melt inclusion and volcanic gas data.* J. Volcanol. Geotherm. Res., 140, 217-240

Watson, I.M., Oppenheimer, C., Voight, B., Francis, P.W., Clarke, A., Stix, J., Miller, A., Pyle, D.M., Burton, M.R., Young, S.R., Norton, G., Loughlin, S., Darroux, B., Staff, M.V.O., (2000). *The relationship between degassing and deformation at Soufriere Hills volcano. Montserrat*. J. Volcanol. Geotherm. Res. 98, 117–126.

Williams-Jones, G., Horton, K.A., Elias, T., Garbeil, H., Mouginis-Mark, P.J., Sutton, A.J., Harris, A.J.L. (2006). *Accurately measuring volcanic plume velocity with multiple UV spectrometers*. Bull Volcanol 68:328–332

Y

Yamamoto, H., Watson, I.M., Phillips, J.C., Bluth, G.J. (2008). *Rise dynamics and relative ash distribution in vulcanian eruption plumes at Santiaguito Volcano, Guatemala, revealed using an ultraviolet imaging camera.* Geophys. Res. Lett., 35, L08314, doi:10.1029/2007GL032008

List of Figures